MASTER'S THESIS

COMPUTATIONAL ABERRATION CORRECTION IN OPTICAL COHERENCE TOMOGRAPHY WITH PHASE-UNSTABLE SYSTEMS

Sebastián Ruiz Lopera
sruizlo2@eafit.edu.co

Universidad EAFIT
School of Sciences
Master in Applied Physics
Applied Optics Group
Medellín
2020

COMPUTATIONAL ABERRATION CORRECTION IN OPTICAL COHERENCE TOMOGRAPHY WITH PHASE-UNSTABLE SYSTEMS

SEBASTIÁN RUIZ LOPERA

Thesis submitted in partial fulfillment of the requirement for the degree of
Master in Applied Physics

Advisors

Ph.D. RENÉ RESTREPO GÓMEZ
Área de Instrumentación óptica espacial
Intituto Nacional de Técnica Aeroespacial

Ph.D. NÉSTOR URIBE PATARROYO
Wellman center for photomedicine
Harvard Medical School and Massachusetts General Hospital

UNIVERSIDAD EAFIT
SCHOOL OF SCIENCES
MASTER IN APPLIED PHYSICS
APPLIED OPTICS GROUP
MEDELLÍN
2020

"A grad student in procrastination tends to stay
in procrastination unless an external force is applied to it."

Newton's first law of Graduation

Acknowledgment

This dissertation is dedicated to my family, for all the company and support given throughout my life, helping me to grow firmly, a step at a time.

I would like to thank

Advisors René and Néstor, for the immeasurable amount of work and time, full of virtual meetings, discussions, ideas, technical and professional advice, all within a pleasing environment that makes hard work gratifying and productive.

Sofía, for the constant support and motivation to keep going in the hard process of research and writing, that thankfully has been brightened by her charming company.

Carolina, for constantly soften the days with her happiness and inspiration.

Professors of the Applied Optics Group Daniel, Carlos and Elena for adopting and saving me of the "bureaucratic limbo" that is having no internal advisor.

Former and current members of the Applied optics Group, in special Manuela for making every day in the lab enjoyable and delightful with snacks and coffee, and Camilo and Carlos for their academic guidance.

José Hérnan, for his technical contribution to this work through his academic project, Taylor M. Cannon, for her experimental contribution to this work in the preparation of samples and acquisition of data, and the members of Brett's lab at Wellman Center for Photomedicine who aided me during my short visit.

SPIE, for support through the 2019 Optics and Photonics Education Scholarship.

Finally, Universidad EAFIT and Vicerrectoría de Descubrimiento y Creación for the internal grant that gave me the possibility to pursuit a graduate degree.

ABSTRACT

Optical coherence tomography (OCT) has become an important imaging modality for biomedical research and medical applications. OCT produces three-dimensional and high-resolution images of tissue by radiating light into the sample and measuring the backscattered light using interferometry. OCT signal is directly related to the complex-amplitude field of backscattered light. Post-processing techniques have been valuable to exploit the vast information in the signal, enabling to improve visualization and analysis of images in terms of practical features like resolution, sensitivity, and contrast, and also to provide additional types of optical contrast that give extra and complementary information of the sample. Since it is an optical modality, OCT is prone to optical aberrations that degrade image quality and resolution, therefore correction of aberrations has been of great interest in OCT.

In the first part of this work, the "OCT experiment" is analyzed from an interference perspective to understand the basic operation of OCT that relies on optical interferometry. Then, an image formation model is described to explain the origin of aberrations in OCT imaging and how to correct them with state-of-the-art computational techniques. These approaches, however, are restricted to operate in specific system setups that provide sufficient experimental conditions for their correct operation. The core of this work is to present a strategy that relaxes experimental conditions required to perform computational aberration correction in OCT tomograms. Additional post-processing tools are also proposed, in particular, to reduce complex noise in the OCT signal, using non-local means to reduce noise efficiently by exploiting the tomographic information.

Computational aberration correction is demonstrated in experimental applications using different samples imaged with phase-unstable swept-source OCT systems that have been deemed unsuitable for this purpose in the past, given its experimental constraints to obtain reliable measurements of the complex signal. Results show correction of defocus in all experimental validations, showing resolution improvement at planes beyond several times the Rayleigh range of the systems, up to 5 times in a proof-of-concept experiment. Significant improvement of image quality is presented in ocular, skin, and endoscopic imaging, combining computational aberration with post-processing techniques developed in the past for speckle noise suppression and the additional tool developed here for noise reduction. Finally, computational refocusing of polarimetric properties of tissue measured with OCT is presented.

CONTENTS

LIST OF FIGURES

LIST OF ACRONYMS

1D, One dimensional.

2D, Two dimensional.

3D, Three dimensional.

ADC, Analog-to-digital conversions.

AO, Adaptive optics.

BFL, Back focal length.

CAC, Computational aberration correction.

CAO, Computational adaptive optics.

CTNode, Coherent tomographic non-local means denoising.

DOP, Degree of polarization.

DoF, Depth of field.

FBG, Fiber Bragg grating.

FDOCT, Fourier-domain optical coherence tomography.

FF, Full-field.

FFL, Front focal length.

FM, Forward model.

FT, Fourier transform.

FoV, Field of view.

ISAM, Interferometric synthetic aperture microscopy.

LF, Line-field.

MEMS, Micro-electro-mechanical mirror system.

MPS, Mean power spectrum.

MS, Multiple scattering.

NA, Numerical aperture.

OCM, Optical coherence microscopy.

OCT, Optical coherence tomography.

OCT-A, Optical coherence tomography angiography.

OF, Optimum filter.

OFDI, Optical frequency domain imaging.

OPL, Optical path length.

OoF, Out of focus.

PS-OCT, Polarization-sensitive optical coherence tomography.

PS-TNode, Polarization-sensitive tomographic non-local means despeckling.

PSF, Point spread function.

RB, Rollback.

ROI, Region of interest.

SAR, Synthetic aperture radar.

SDOCT, Spectral-domain optical coherence tomography.

SE, Shannon's Entropy.

SHARP, Short Aline-Range Phase-stability adaptive optics.

SLO, Scanning laser ophthalmoscope.

SNR, Signal-to-noise ratio.

SOA, Semiconductor optical amplifier.

SSOCT, Swept-source optical coherence tomography.

STD, Standard deviation.

TDOCT, Time-domain optical coherence tomography.

TNode, Tomographic non-local means despeckling.

VCSEL, Vertical cavity surface emitting lasers.

CHAPTER 1

INTRODUCTION

Light-matter interaction has become a relevant tool in medical sciences and biology, enabling the creation and development of a specialized field known as *biomedical optics* or *biophotonics* oriented to fundamental research, imaging, diagnosis, therapy and monitory of diseases and surgery assistance [1]. Many imaging techniques have emerged to cover the general necessity to visualize internal structures of tissues. In particular, *Optical Coherence Tomography* (OCT) has become an important imaging modality for biomedical optics and medicine [1, 2]. The following sections present a general introduction to the operation and applications of OCT in medicine.

1.1. Optical coherence tomography in medicine

OCT *is an imaging technique that produces three-dimensional, micrometric-resolution images of scattering samples such as biological tissues by measuring the light that is backscattered by the sample using low-coherence interferometry* [2, 3].

The research community in biophotonics has shown great interest in OCT given its unique features such as high sensitivity that allows obtaining useful information from biological samples with different optical properties, and its resolution of 1-15 μm and axial range of $\sim$2 mm that fills a gap between other medical imaging modalities such as ultrasound and confocal microscopy [4]. Furthermore, non-invasive operation of OCT, both *ex vivo* and *in vivo*, with no contrast agents nor ionizing radiation are important features that have positioned OCT in the medical community for imaging of tissue pathologies *in situ* and in real-time, particularly in ophthalmology [5, 6], but also in endoscopic imaging [7], intravascular imaging [8, 9] and dermatology [10, 11] among others [12–14].

OCT produces cross-sectional and volumetric images by measuring the magnitude and "echo time delay" of light backscattered by the sample [3], similarly to the operation of other tomography techniques, such as ultrasound [15] that uses sound instead of light. Backscattered light contains information of the optical properties of the sample, and this information is distinguished at different depths by determining

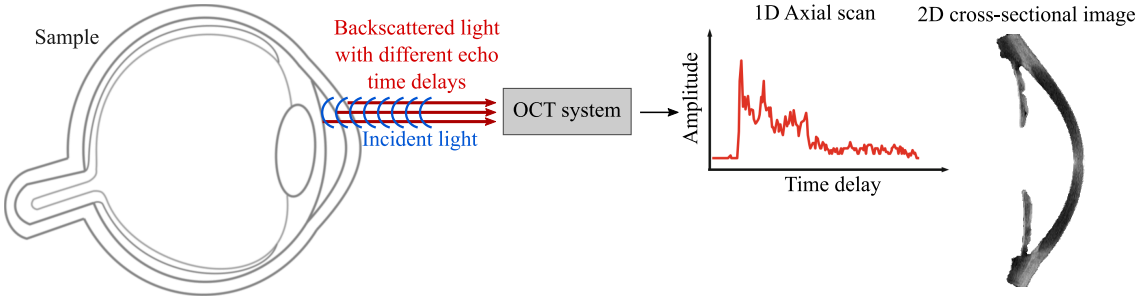

Figure 1.1: Example of axial scan and cross-section images generated by OCT measuring the magnitude and echo time delay of backscattered light.

the time it takes for light to travel different axial distances, thus performing an axial scan, that can be expanded to a cross-sectional image (as depicted in Figure 1.1) and also to volumetric information. Given the large magnitude of the speed of light of $\sim 3 \text{x} 10^8$m/s, there are technical limitations to make electronic devices with the required sensitivity and time resolution to measure the echo time delay of light with micrometric resolution [4]. Hence, OCT employs low-coherence interferometry to measure the backscattered light in terms of optical path length differences rather than measuring the temporal delays directly [3], being both related through the speed of light.

Providing cross-sectional images *in situ* and in real-time without the need to remove and process specimens is a valuable feature of OCT for the visualization of tissue microstructure and pathology. This possibility to perform "optical biopsies" [16] enables operation of OCT in applications where histology of excised tissue, the gold standard for assessing pathology, is insufficient for various reasons [4]: (1) biopsy is hazardous or impossible, for example in the eye, arteries or nervous tissues, (2) biopsy is susceptible to sampling errors, given the impossibility to detect the location of the pathology precisely, for example in cancer diagnosis, leading to a false negative, (3) real-time visualization is required, for instance, in guidance of invasive procedures, and (4) structural information is not sufficient and additional functional imaging or measurements like blood flowmetry is necessary.

Several phenomena occur in the interaction of the sample and the incident light. OCT measures only the backscattered light; the light that is scattered in the opposite direction of the incident beam. In that sense, the major limitation of OCT is that light is highly scattered in multiple directions by most tissues reducing the portion of backscattered light. This attenuation by scattering imposes a limit to imaging depth in OCT to $\sim$2 mm in tissue [4]. Light sources in the near-infrared range with a wavelength between 840–1300 nm are used widely for OCT, given the low water absorption and high scattering of tissue [17]. Many OCT systems use $\sim$1300 nm wavelength, because it provides larger imaging penetration compared to shorter

wavelengths, although the standards for ophthalmology are ∼850 nm and ∼1 μm wavelengths [4].

OCT has become a crucial standard for clinical assessment in ophthalmology given that the optical transparency of the eye allows "easy" optical access to the retina and the posterior segment of the eye. First experimental demonstration of OCT imaging in 1991 by Huang *et al.* was performed in the human retina and coronary artery *ex vivo* [3]. Following works by Fercher *et al.* [18] and Swanson *et al.* [19] demonstrated retinal images *in vivo*, and since then, ophthalmology has been the specialty with more clinical studies and technical developments in OCT, because it assists in the diagnosis of diseases in early and late stages [20–22], even before visual symptoms or irreversible consequences occur [23], and it also allows tracking the progression of diseases and monitor response to therapy [24–26].

The most direct application of OCT after ophthalmology is in dermatology, given the easy access to skin tissue [27]. OCT allows the identification of skin features like sweat ducts, dermal/epidermal junction, and collagen-rich structures [10], but imaging depth is very limited because of the highly scattering properties of skin tissue [28]. Although it is an active application for OCT, for instance, in skin cancer diagnosis [29], the medical impact of OCT in dermatology is not as relevant as in ophthalmology given that practical and scientific benefits over standard medical procedures in this field are not clear.

Medical applicability of OCT was extended after integrating OCT imaging systems with catheters, endoscopes, and needles probes that enable operation of OCT in luminal tissue such as gastrointestinal tract [30], vasculature [8] and airway [31], and in solid organs [32]. The possibility to image internal body organs *in situ* is crucial when excision of tissue is not possible or hazardous, for instance, in intravascular imaging, which is currently a relevant medical OCT application [9].

Moving to an experimental description of OCT, the general setup consists of a light source, an optical interferometer such as Michelson or Mach-Zehnder interferometers, and a light detector [3], as depicted in Figure 1.2. In the interferometer, light from the light source is divided into two beams, one is reflected by a mirror, the other by the sample, and both are recombined producing interference that is captured by the detector. The axis in which light propagates is referred as *axial* axis and the orthogonal axes are known as *lateral* or *transverse* axes. Most OCT systems focus the light into a small spot in the sample and measure the axial scan known as *A-line*, relating the amplitude of the signal versus depth. Then, the position of the focused spot in the transverse plane is swept using two galvanometer mirrors, and in each position, an A-line is acquired, which is known as raster scan. Acquisition of A-lines at different positions of the sample along one lateral axis known as *fast scan axis* produces 2D cross-sectional views known as *B-scans*. Acquisition of B-scans at

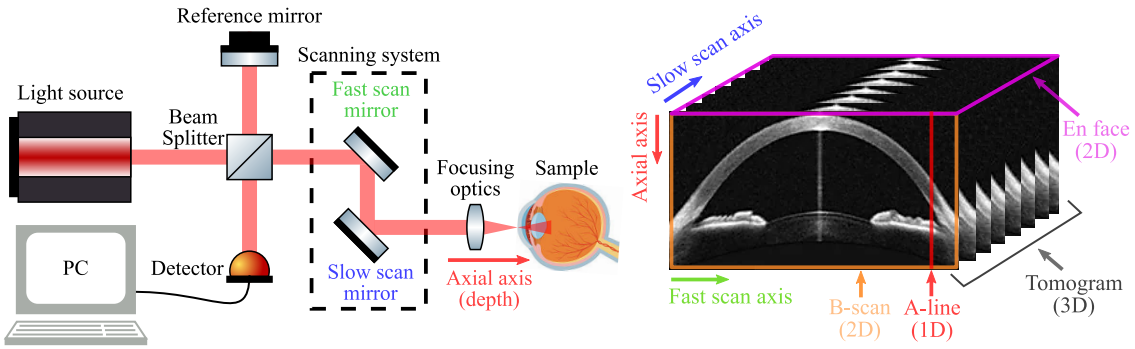

Figure 1.2: Schematic of a generic OCT setup based on a Michelson interferometer and illustration of common notation used for axial axis, transverse axes (fast/slow scan axes), axial scan (A-line) and cross-sectional images (B-scan, *en face*).

different positions of the sample along the lateral axis orthogonal to the fast scan axis, known as *slow scan axis*, provides volumetric images or *tomograms*. Furthermore, the cross-section relating the two lateral axes at a fixed depth is known as *en face* [4]. See Fig. 1.2 for an illustration of the notation described above. An additional scan type used in very particular applications consists of acquiring multiple A-lines in time but at the same location, which is known as *C-scan*.

From this general scheme, OCT technology and theory have evolved. To date, there is a wide variety of system configurations with particular advantages in terms of imaging speed, sensitivity, imaging depth, among others [4]. The use of an optical system to focus the light into the sample and to collect the backscattered light is common to any OCT system, and its properties greatly influence the quality of images. Most notably, it determines the lateral resolution, i.e. the resolution in the lateral axes, and it may induce optical aberrations that degrade image quality, similarly to any other optical imaging technique [33–35].

1.2. Aberrations in OCT

Most OCT systems focus light on the sample, hence the lateral resolution is defined by the diffraction-limited spot size of the focused light beam [4]. Optical aberrations, whether from the optical systems or the sample itself, degrade image quality affecting the visualization of fine structures and limiting the axial range where images appear sharp [33, 36]. Specialized optical systems are used to avoid or reduce the impact of aberrations, for instance, telecentric and achromatic systems correct for spherical and chromatic aberrations [37].

One of the main limitations of optical systems is that they produce in-focus images only for those planes of the sample that are within the *depth of field* (DoF) —defined by the numerical aperture (NA) of the system— because beam divergence causes a

resolution loss for planes outside the DoF, producing defocused images [33, 34]. In the case of OCT, this means that certain planes of the tomogram will be in-focus and appear sharp, but others are out-of-focus and appear blurred. This effect is overcome by using systems with large DoF of ∼0.5 – 2 mm, and in such case, imaging axial range is limited by signal attenuation in tissue rather than by the effect of defocus. However, a large DoF implies a low lateral resolution given its inverse relationship, well-known as lateral-resolution–DoF trade-off. For this reason, the resolution in the transverse plane is often lower than the resolution in the axial axis, which depends on the central wavelength and spectral bandwidth of the light source [4].

In addition to system-induced aberrations, the sample can introduce aberrations with a significant impact to reduce image quality, particularly in ophthalmology given that light beam passes through the eye of the subject and imperfections in the cornea and the lens may induce aberrations [38, 39].

Because aberrations affect the raw OCT signal, any subsequent post-processing will be influenced by them as well [40, 41], such is the case of functional imaging techniques like polarization-sensitive OCT (PS-OCT), which is an extension of OCT for measuring the polarimetric properties of the sample [42], and OCT angiography (OCT-A) used for vasculature label-free imaging [43].

High-resolution imaging is a very active research field in OCT since it gives access to additional and more detailed information of the sample, which is important in many applications, for example, in cellular imaging as eye photoreceptors [44]. To obtain high-resolution images, aberration can be corrected with hardware-based adaptive optics (AO) [36] or computational aberration correction (CAC) [35]. In AO, additional hardware is used to correct for wavefront distortions *in situ*. It demands complex optics and system design that limit clinical applicability, yet, it is incapable of compensating the lateral-resolution–DoF trade-off because each depth demands an individual correction, but OA applies a global correction [45].

CAC operates the complex OCT signal using mathematical models based on the propagation of light to compensate aberrations using an appropriate phase filter [33–35]. CAC addresses lateral-resolution–DoF trade-off. Its major limitation is the reduction of signal strength given that the acquired signal is weaker in the presence of aberrations, which is an experimental limitation that, in principle, cannot be corrected in post-processing [46]. Currently, the operation of CAC is not possible in all OCT systems due to technical limitations that prevent the acquisition of reliable complex-value tomograms [47].

In this work, we present a method for CAC suitable for most common OCT systems to expand its applicability throughout research and clinical applications, making it possible to correct for optical aberration to improve image quality by

post-processing in systems where it was not possible due to technical limitations.

1.3. Noise in OCT

Noise is any contribution to the measured signal apart from the backscattered light, which is the interest of OCT [48]. In that sense, *speckle* arising in tissue imaging as a consequence of coherent interference of backscattered light with random phases [49], is not noise in rigorous terms. Actually, speckle is important for several functional imaging applications [43, 50, 51], but it causes random fluctuations that often hinder visual interpretation [52]. Consequently, speckle reduction while preserving the visibility of fine structures is an active area of research in OCT [53] and in most coherent imaging techniques, such as synthetic aperture radar (SAR) [54]. For this reason, noise reduction in OCT is generally associated with speckle reduction, but there are multiple sources of strictly speaking noise in the OCT signal induced by the system, that have a relevant impact on imaging features such as the *signal-to-noise ration* (SNR), defined as the ratio of the signal power and the noise process variance; the sensitivity, defined as the SNR of a perfect reflector placed in the sample arm; and the dynamic range, defined as the range of SNR observable within a signal acquisition or image [48, 55]. SNR is typically given in decibels (dB) through the logarithmic transformation $\mathrm{SNR}_{\mathrm{dB}} = 10 \log_{10} \mathrm{SNR}$. Developments in OCT technology had a significant improvement in sensitivity and current imaging systems achieve sensitivities as high as ∼100 dB, meaning that the minimum detectable reflectivity in the sample is $\sim 1 \times 10^{-10}$ times the reflectivity of an ideal reference mirror [48]. In experimental terms, OCT images span dynamic ranges of 40–60 dB although it depends on the tissue and the system.

The most notable sources of noise in the OCT signal are shot, excess and thermal noise [55]. *Shot* noise originates from the uncertainty of "counting" particles of discrete nature such photons and electrons, and it arises in the detection of the OCT signal that involves photon-electron conversion and digitization. *Excess* noise arises from time fluctuations of the incident intensity, mostly due to fluctuation of the emission of the light source. *Thermal* noise stems from the random motion of electrons in conductors. In OCT, noise has been addressed mostly experimentally, and at this point, it is possible to achieve shot noise-limited detection [55]. For instance, excess noise suppression is achieved using two detectors in a *balanced* detection scheme where non-interfering light —that contributes the most to excess noise— is suppressed. Computational approaches for noise reduction have concentrated on speckle suppression, and most shot noise reduction approaches rely on a straightforward average of multiple frame repetitions [56].

In the presence of aberrations, there is a reduction of SNR and dynamic range

because the collected light is intrinsically less in the presence of aberrations than in the aberration-free case, and this issue is not addressed in CAC techniques. An experimental approach to reduce signal strength loss is to use CAC techniques in systems with an astigmatic beam that provides high light collection throughout a longer depth than a Gaussian beam, and then aberrations are corrected in post-processing including astigmatism induced on purpose [35].

1.4. Problem statement

Post-processing is important in OCT to obtain images with high resolution and contrast as well as additional useful information of the sample, improving and facilitating study, diagnosis, and monitory of diseases. Developing techniques to improve image quality in OCT has been the scope of collaborative projects between the Applied Optics Group at Universidad EAFIT and the Wellman Center for Photomedicine at Massachusetts General Hospital and Harvard Medical School. Results include the development of a useful technique for speckle suppression [53], as well as the derivation of models for robust estimation of the autocorrelation function of intensity OCT signal [57] that is the basis of functional imaging modalities such as angiography [43] and flowmetry [51]. In parallel, experimental setups have been made, including a lab-made accessible full-field OCT system [58] and a linear-in-wavenumber spectrometer for spectral-domain OCT [59]. In addition, a numerical phase correction algorithm was proposed but, given its iterative structure, processing times are unpractical and results are limited [60], however, this initial approach for phase stabilization contributed to ideas and notions that led to the current proposal.

Computational aberration correction is a very active field in OCT to improve image quality in applications where aberrations have a significant impact and to provide high-resolution images [35, 61, 62]. The development of CAC techniques has been constrained to system configurations that allow a more reliable and robust measurement of the complex-valued tomogram. CAC techniques rely on a common mathematical model, hence requirements for its application are the same, being phase stability the most relevant requirement [47]. *Phase stability* is achieved when there is a constant phase relation between measurements at different lateral locations [47], in other words, when there exists a correlation between measurements.

The acquisition of phase-stable tomograms is not straightforward in practical terms given that phase is highly sensitive to phase noise that affects phase stability [47, 63], arising from the imaging system and from the sample itself due to axial motion [64, 65]. Sample motion artifacts include two effects: the first is a phase jump due to the Doppler effect [66, 67], and the second is the effective shift of the complex information due to the sample's displacement. Doppler phase noise is the issue most addressed

for CAC given that its impact is, in general, more notable than the impact of complex-amplitude shift [64, 65], although the impact of each effect is relative to features of the imaging system and the magnitude of motion [47].

Achieving sufficient phase stability for CAC has restricted its usage to custom system configurations with volumetric phase stability, that in some cases is achieved at the cost of increasing system complexity [61, 68–70]. In phase-stable systems, operation of CAO is straightforward and for *in vivo* imaging, it is sufficient to correct for phase noise due to the sample's axial motion using numerical corrections based on reference phase signal, generated by adding a highly reflective surface such as a coverslip, or based on the measured signal [67, 71]. A drawback of methods based on a reference phase signal is that it demands hardware modifications to add a highly reflective surface in addition to the reference mirror.

Numerical phase stabilization methods based on the sample signal assume that there is phase stability at least along one lateral axis, thus correction is only required along the orthogonal lateral axis [65]. This assumption is valid for phase-stable systems in which phase instabilities in the tomogram arise from sample motion that only affects one lateral axis, commonly the slow scan axis [65]. However, there are standard OCT configurations that present phase noise induced in the system, for which current numerical phase corrections are hopeless because there is not any axis with phase stability [63]. Operation of CAO in such phase-unstable configurations rely on hardware modifications to avoid system-induced phase noise, restricting its applicability in research and medical applications.

Given the current limitation of standard OCT systems to acquire phase-stable tomograms, the proposal of this work is *to develop and experimentally test a post-processing method for optical aberration correction in phase-unstable tomograms, with no need for hardware modifications or specialized configurations, hence enabling operation of CAC for image quality improvement in system unsuitable for it so far, more specifically, in raster scan wavelength-swept source OCT systems.*

Additional issues in CAC are considered as well, regarding the SNR reduction in aberrated tomograms due to signal strength loss, as well as the motion artifacts affecting the complex amplitude, not only the phase.

1.5. Objectives

1.5.1. General objective

To correct optical aberrations in optical coherence tomography with phase-unstable systems using post-processing.

1.5.2. Specific objectives

- To establish the state-of-art of computational aberration correction in optical coherence tomography.
- To identify sources of phase noise and phase correction methods for optical coherence tomography.
- To develop a computational method for phase stabilization and aberration correction of tomograms with no intrinsic phase stability.
- To test the performance of the method with *ex vivo* and *in vivo* tomograms acquired with typical phase-unstable OCT systems.
- To identify and analyze the possible limitations of the method.

1.6. Outline of the work

The principal outcome of this work is the development of the technique Short Aline-Range Phase-stability adaptive-optics (SHARP) for computational aberration correction in phase-unstable systems [72]. SHARP is demonstrated in successful experimental results using systems with no need for specific hardware that ensures phase stability, in a variety of OCT application ranging from ocular imaging to endoscopic imaging and including *ex vivo* and *in vivo* modalities. SHARP integrates a computational aberration correction technique with numerical phase noise correction to compensate aberrations in phase-unstable OCT tomograms, showing particular potential for extending the depth of field to relax the lateral resolution–DoF trade-off.

Additional approaches to address other general drawbacks and limitations of CAC are proposed. Complex noise reduction approaches are presented to countervail the intrinsic reduction of SNR in computational aberration-corrected images when compared to experimental aberration-free images. Second, SHARP is extended to admit tomograms affected by complex amplitude shifts due to sample motion for *in vivo* imaging, in addition to the Doppler phase term, thus addressing both

effects of motion artifacts. Furthermore, an optional step for correcting spatial-varying aberrations encountered in certain practical scenarios is described. Finally, a strategy to perform computational aberration correction in polarization-sensitive OCT is presented, taking into consideration the particularities of the processing used in this functional imaging technique to properly correct aberrations. Successful computational refocusing of polarimetric properties images of tissue is presented. This is the first integration of computational refocusing in polarization-sensitive OCT to the best of our knowledge.

There is a particular interest in this work in noise reduction because of its importance not only in CAC but in OCT imaging universally to improve sensitivity and dynamic range. The first proposal introduced here for noise reduction is to use a straightforward frequency filter grounded in the context of image deconvolution, that has been used in several imaging modalities, for instance, in astronomy. This filter is used for image deconvolution but it is not particularly dedicated to noise reduction despite its potential for such purpose.

The second approach is a more sophisticated noise reduction technique termed Coherent Tomographic Non-local-means denoising (CTNode). This technique is an adaptation of the previous despeckling technique Tomographic Non-local means despeckling (TNode) with the adequate modifications to address for photon noise in the complex-amplitude tomogram, which is the aim of CTNode, instead of suppressing speckle in the intensity tomogram, that is the aim of TNode. Both approaches are based on non-local-means weighted-averaging using statistical properties of its corresponding undesired component, i.e. photon noise or speckle. Experimental results of CTNode are presented in conjunction with SHARP, although the use of both techniques is independent. CTNode promises to be a more efficient technique than standard approaches based on frames averaging, with potential applications in functional OCT techniques.

1.7. Structure of the document

In this Chapter, a general introduction of OCT was provided to present the problem and the objectives of this work.

In Chapter 2, there is a description of the principle of operation of OCT and the different possible configurations, making emphasis on the level of phase stability that is achieved in each configuration. A mathematical model for the signal of the "OCT experiment" is presented from an interferometric perspective and then from a light propagation and image formation perspective. The latter model serves as the basis for the CAC techniques that are then described, followed by a description of phase stability requirement in CAC and phase stabilization techniques, emphasizing

numerical approaches. A simulated tomogram with simple structures generated elsewhere based on the acquisition of the complex OCT signal [60] is used to illustrate concepts and explanations when required.

Foundation and description of SHARP are given in detail in Chapter 3. Results of a proof of concept experiment are presented, in which a cucumber sample presenting remarkable structures was used to acquire tomograms without and with defocus induced deliberately shifting the position of the focal plane. Furthermore, approaches to address additional important issues in CAC, besides phase stability requirement, are proposed, namely, motion artifacts and spatially-varying aberration correction. Mathematical and conceptual framework of CTNode are also presented in Chapter 3, briefly explaining the operation of non-local means algorithm and then deriving its particular operation in CTNode, taking into consideration the origin and statistical description of photon noise in the OCT signal. Results are presented using the simulated noiseless tomogram mentioned previously.

Experimental validation of the methods is presented in Chapter 4 for a variety of samples, systems, and applications, including *ex vivo* and *in vivo* imaging in ophthalmic, endoscopic, and dermatologic OCT. Aberration correction with SHARP is demonstrated in anterior segment imaging of a swine eye *ex vivo*, endoscopic OCT of a swine airway *in vivo*, and skin imaging of human hand dorsal *in vivo* affected by involuntary motion. Furthermore, it is showed that the integration of SHARP and resolution-preserving despeckling technique TNode dramatically improves image quality in comparison to the raw tomograms. Also, noise reduction with CTNode is demonstrated in conjunction with SHARP in anterior segment imaging and separately in human retina imaging *in vivo*, showing a significant noise floor reduction. Additionally, the operation of SHARP in PS-OCT based on Stokes processing is demonstrated in the anterior segment of an excised swine eye, showing successful defocus correction in polarimetric parameters of tissue. In each demonstration, a discussion and analysis of the methods and the results are given, highlighting the capabilities and drawbacks.

Finally, conclusions regarding the results and objectives of the work are discussed in Chapter 5, as well as possible further steps in the context of noise reduction and computational aberration correction in OCT.

CHAPTER 2

THEORETICAL BASIS

There have been several theoretical and technical advances in optical coherence tomography in response to the importance that it has gathered in the biomedical optics community [4]. In this chapter, the principle of operation, models for the OCT signal, and advances of OCT are explained, including the different configurations that have been developed, starting from the initial approach based on low-coherence interferometry in time domain detection [3] that later advanced into spectral domain detection [73, 74]. Also, this Chapter presents advantages and disadvantages in practical features of OCT configurations such as sensitivity [55], imaging speed [75], and most importantly here, phase stability [67] that is discussed in detail. In the first part of this Chapter, Section 2.1, the OCT experiment is analyzed from an interferometric perspective in regard to the coherence gating used for axial scan performed in OCT. In the second part, Section 2.2, propagation of light in the sample arm is taken into consideration to establish a more general model for image formation in OCT, concerning the confocal gating used for the transverse scan. From this model derive the state-of-the-art techniques for computational aberration correction in OCT explained in Section 2.3, where also phase stability requirement and approaches to achieve it are discussed and exemplified with simulations.

2.1. Optical coherence tomography

Tomography techniques produce images by sectioning the sample using a penetrating wave [76]. In medicine, tomography techniques radiate waves into the sample and measure the backscattered waves to produce images of the internal structure of tissues [76]. For instance, ultrasound employs sound waves and measures the echo time delay and amplitude of the reflected waves [77], while optical coherence tomography employs light. Measuring the echo time delay of light with micrometric resolution using direct electronic detection schemes as in ultrasound is challenging given that light is around six orders of magnitude faster than sound. Therefore, optical ranging measurements demand alternative approaches such as high-speed optical gating [78] or low-coherence interferometry that is the basis of OCT [3].

2.1.1. Measuring the echo time delay of light

Using backscattered light to see through biological tissue was proposed by Duguay [78, 79] in 1971 employing a high-speed optical Kerr shutter with a 10 pico-seconds pulsed laser to "photograph light in flight" while propagating through a cell of milk and water [78]. In subsequent approaches, resolution was improved using nonlinear optical processes to detect the time delay of backscattered light with a femto-second resolution, making it possible to measure corneal thickness in a rabbit eye *ex vivo* with 15 μm resolution [80]. These approaches are unpractical for reasons like the use of intense pulsed lasers and the low sensitivity of around -70 dB while current OCT systems achieve sensitivities of -100 dB, three orders of magnitude greater in linear scale [4].

2.1.2. Low-coherence interferometry

The potential of low-coherence interferometry to measure the echo time delay of backscattered light with high resolution and sensitivity was devised in the 80's decade, starting with optical fibers and waveguide devices [81, 82] and later with biological samples after the first demonstration by Fercher *et al.* in 1988 [83] who measured the axial eye length. Interferometry techniques measure the correlation between optical fields by interfering light that is backscattered by the sample with light that has traveled through a reference path [84]. In an interferometer, light emitted by the source is divided into two arms, one is reflected by a reference mirror and the other is reflected by the sample, and then both are recombined to produce interference in a detection plane. Interference only occurs when the optical path length (OPL) difference between the two light beams is within the *coherence length* of the light source l_c. This is the optical distance that different waves from the same light source can mismatch and yet maintain a *degree of coherence* or a *correlation* [85].

The emission spectrum determines the coherence length of a light source: l_c is inversely proportional to spectral bandwidth. The key insight in high-resolution low-coherence reflectometry is the use of sources with broad-spectrum that present short coherence length; *interference signal at a given OPL can be distinguished from interference signals at others OPL with a resolution equal to the coherence length.* This *coherence gating* establishes the principle of axial scan in OCT. For a Gaussian spectrum with central wavelength λ_c and full-width at half-maximum $\Delta\lambda$, axial resolution δz is

$$\delta z = \frac{2\ln 2}{\pi}\frac{\lambda_c^2}{\Delta\lambda}. \tag{2.1}$$

Inverse relation between δz and $\Delta\lambda$ shows that light source with broad emission spectrum or short central wavelength provides fine axial resolution.

To derive the axial OCT signal, consider the Michelson interferometer in Fig. 2.1.

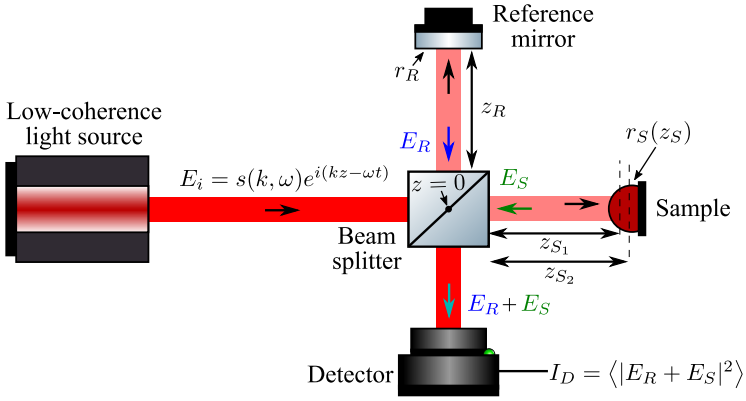

Figure 2.1: Schematic of generic Michelson interferometer used in OCT.

Interferometry measures the correlation between the electric fields of the light reflected by the sample and the reference mirror [84]. Consider that the light source emits plane waves with electric field $E_i = s(k,\omega)e^{i(kz-\omega t)}$ at time t and distance z along the propagation axis, being $s(k,\omega)$ the complex amplitude, dependent on the angular frequency ω and wavenumber $k = 2\pi/\lambda$ for wavelength λ. Assuming free space propagation and a 50/50 beam splitter, the reference beam propagates a distance z_R from the beam splitter to the reference mirror with reflectivity r_R and reflectance $R_R = |r_R|^2$, then reflected light propagates back to the beam splitter and its electric filed can be expressed as $E_R = \dfrac{E_i}{\sqrt{2}} r_R e^{i2kz_R}$.

On the other hand, light on the sample arm propagates a distance z_S from the beam splitter to the sample. In biological tissues, the refractive index changes, resulting in different reflectivities, therefore, the sample can be described as a discrete number N of reflectors with reflectivities r_{S_n} and reflectances $R_{S_n} = |r_{S_n}|^2$ located at distances z_{S_n} as

$$r_S(z_{S_n}) = \sum_{n=1}^{N} r_{S_n} \delta\left(z_S - z_{S_n}\right). \tag{2.2}$$

Coherent gating in OCT allows to reconstruct the function $\sqrt{\mathbf{R_{S_n}(z_{S_n})}}$ to produce images with optical contrast related to changes in the refractive index of the sample [48].

Light backscaterred by the sample propagates back to the beam splitter with electric field $E_S = \dfrac{E_i}{\sqrt{2}} \sum_{n=1}^{N} r_{S_n} e^{i2kz_{S_n}}$. Reference and sample electric fields E_R and E_S interfere and a photodetector with responsivity ρ captures the intensity producing a

photocurrent $I_D(k,\omega)$ that can be described as [48]

$$\begin{aligned} I_D(k,\omega) &= \rho \left\langle \left| \frac{E_R}{\sqrt{2}} + \frac{E_S}{\sqrt{2}} \right|^2 \right\rangle \\ &= \rho \left\langle \left| \frac{E_i}{2} r_R e^{i2kz_R} + \frac{E_i}{2} \sum_{n=1}^{N} r_{S_n} e^{i2kz_{S_n}} \right|^2 \right\rangle \\ &= \frac{\rho}{4} \left\langle \left| s(k,\omega) r_R e^{i2kz_R - \omega t} + s(k,\omega) \sum_{n=1}^{N} r_{S_n} e^{i2kz_{S_n} - \omega t} \right|^2 \right\rangle, \end{aligned} \tag{2.3}$$

assuming $z = 0$ at the splitting surface of the beam splitter without loss of generalization. $\langle \cdot \rangle$ is the temporal averaging performed by the photodetector during the integration time of a single measurement, which is long enough to expect that I_D is independent of the temporal component ωt given the fast temporal oscillation of light imposed by ω. This is consistent with expansion of Eq. (2.3) using $|E|^2 = E^* E$ that yields the spectral interferogram [48]

$$\begin{aligned} I_D(k) = \frac{\rho}{4} &\left[S(k) \left(R_R + \sum_{n=1}^{N} R_{S_n} \right) \right] ... \\ + \frac{\rho}{2} &\left[S(k) \sum_{n=1}^{N} \sqrt{R_R R_{S_n}} \cos\left(2k\left[z_R - z_{S_n}\right]\right) \right] ... \\ + \frac{\rho}{4} &\left[S(k) \sum_{n \neq m}^{N} \sqrt{R_{S_n} R_{S_m}} \cos\left(2k\left[z_{S_n} - z_{S_m}\right]\right) \right], \end{aligned} \tag{2.4}$$

where $S(k) = |s(k,\omega)^2|$ is the light source spectrum and $z_R - z_{S_n}$ is the OPL difference.

There are three components in $I_D(k)$ as noted in Eq. (2.4). The first one is a *background* component that is independent of propagating distances and it is the largest component given that typically reference mirror reflectivity denominates the sample reflectivity. In general, this is an undesired component that is canceled out using dual balanced detection [86].

Second is a *cross-correlation* component that depends on the spectrum of the light source $S(k)$, the wavenumber k and the OPL difference $z_R - z_{S_n}$. This is the desired component in OCT imaging since it gives access to the sample reflectivity through the term $\sqrt{R_R R_{S_n}}$.

The last term is an *auto-correlation* component that represents the interference between the different sample reflectors, independent of the reference light. This is

commonly an artifact component that can be neglected by increasing the magnitude of the other two components by increasing the reference mirror reflectivity.

Note that $I_D(k)$ in Eq. (2.4) is the interference resulting from a particular wavenumber k, but the ultimate aim in OCT is to "isolate" the $\sqrt{R_R R_{S_n}}$ term along depth, i.e. versus OPL differences. There are two approaches to retrieve the depth-dependent photoccurent $i_D(z)$, yielding two major OCT configurations: time-domain OCT (TDOCT) [3] and Fourier-domain OCT (FDOCT) [73].

2.1.3. Time-domain OCT

Most straightforward way to obtain the depth-dependent signal is to use a mono-pixel detector to capture the interference while the reference delay z_R is scanned by moving the reference mirror along the axial direction as shown in Figure 2.2. The detector captures the intensity for all k at the same time, thus $i_D(z_R)$ is the integration over all k of $I_D(k)$ [48],

$$i_D(z_R) = \frac{\rho}{4} S_0 \left(R_R + \sum_{n=1}^{N} R_{S_n} \right) ... \\ + \frac{\rho}{2} S_0 \sum_{n=1}^{N} \sqrt{R_R R_{S_n}} e^{-(z_R - z_{S_n})^2 \Delta k^2} \cos\left[2k_0 \left(z_R - z_{S_n}\right)\right], \tag{2.5}$$

where $S_0 = \int_0^\infty S(k)dk$ is the spectral total power emitted by the light source, and a normalized Gaussian spectrum $S(k) = \frac{1}{\Delta k \sqrt{\pi}} e^{-\left[\frac{(k-k_0)}{\Delta k}\right]^2}$ is assumed, being k_0 the central wavenumber and Δk the full-width at $1/e$ of the maximum.

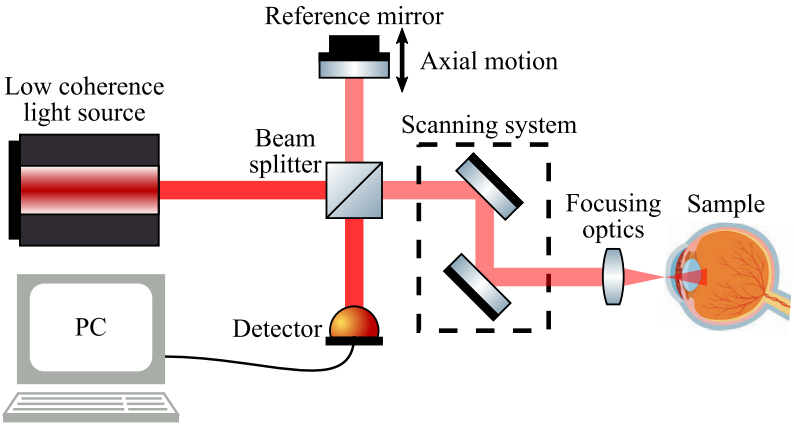

Figure 2.2: Schematic of a generic TDOCT setup based on a Michelson interferometer, where the axial scan is performed by displacing the reference mirror in the axial axis while recording the interference with a mono-pixel detector.

Time domain A-line $i_D(z_R)$ consists of a background component (DC), proportional to S_0, and an interference component that is a summation of Gaussian functions with finite width, having peak-values of $\sqrt{R_R R_{S_n}}$ located at OPL differences $z_R - z_{S_n}$ and modulated by cosines of period π/k_0, equivalent to $\lambda_0/2$. $\gamma(z_R) = e^{-(z_R - z_{S_n})\Delta k^2}$ is known as the *coherence function* and it causes a "broaning" of the interference signal of each reflector and its width is related to the coherence length of the light source that determines the axial resolution, thus $\gamma(z_R)$ is considered as the axial point spread function (PSF) [48]. Figure 2.3 illustrates a TDOCT A-line in Fig.2.3(b) for a sample characterized by three reflectors as shown in Fig.2.3(a).

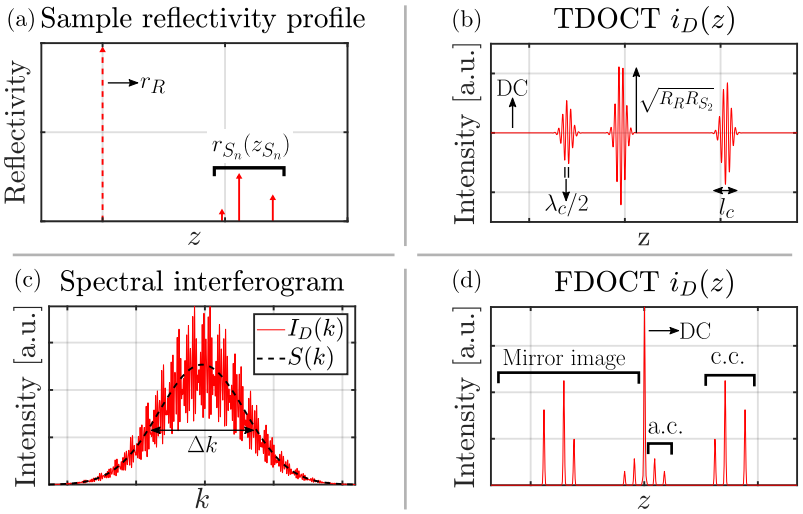

Figure 2.3: Illustration of A-lines obtained in OCT. (a) Axial reflectivity profile for a sample characterized by three reflectors: (b) TDOCT A-line, (c) spectral interferogram and (d) FDOCT A-line obtained as the Fourier transform of (c), indicating the background (DC), cross-correlation (c.c.) and auto-correlation (a.c.) components.

Early OCT imaging systems including the first experimental demonstration of OCT in 1991 [3] employed a time-domain detection. Time-domain designation arises from the fact that the reflectivity axial profile of the sample is acquired while displacing the reference mirror in time. This demands mechanical systems to displace the reference mirror, which limits imaging speed to A-line rates $<\sim$2 kHz [48], due to technical restrictions to develop precise and fast motion systems with micrometric resolution and millimetric travel range. Furthermore, given that the axial scan is acquired while the detector captures the signal at different times, stable systems are required to avoid artifacts during imaging due to changes in the imaging conditions, for instance, changes in the light source emission. For this reason, achievable sensitivity is limited and this, in addition to low imaging speed, establishes the major drawbacks of TDOCT [87].

2.1.4. Fourier-domain OCT

Although TDOCT systems served well in early medical development of OCT, their relatively slow scan rate and limited sensitivity restricted the potential of OCT and restricted its expansion to many medical applications. An improvement in sensitivity and imaging speed in OCT was possible with the introduction of FDOCT systems, where the reference mirror remains fixed [55, 87, 88]. Axial spatial domain and optical frequency domain are conjugate with the wavenumber and the OPL difference being Fourier transform duals. This concept led to development of Fourier-domain acquisition where photocurrent $I_D(k)$ in Eq. (2.4) is captured directly in the k space and a subsequent Fourier transform $\mathrm{FT}_k\{\cdot\}$ of the signal along variable k yields the depth-dependent photocurrent $i_D(z)$, with no need to displace the reference mirror [73].

Using the Fourier transform property $\mathrm{FT}_k\{\cos(kz_0)\} = \frac{1}{2}[\delta(z+z_0) + \delta(z-z_0)]$, the convolution theorem $\mathrm{FT}_k\{g(k)f(k)\} = \mathrm{FT}_k\{g(k)\} * \mathrm{FT}_k\{f(k)\}$, and the shifting property of delta functions $f(z) * \delta(z-z_0) = f(z_0)$, it is possible to obtain the FDOCT A-line $i_D(z) = \mathrm{FT}_k\{I_D(k)\}$ from Eq. 2.4 as [48]

$$\begin{aligned} i_D(z) = \frac{\rho}{8}\gamma(z)\left[R_R + \sum_{n=1}^{N} R_{S_n}\right] \ldots \\ + \frac{\rho}{4}\sum_{n=1}^{N}\sqrt{R_R R_{S_n}}\left[\gamma\left(2\left[z_R - z_{S_n}\right]\right) + \gamma\left(-2\left[z_R - z_{S_n}\right]\right)\right] \ldots \\ + \frac{\rho}{8}\sum_{n\neq m=1}^{N}\sqrt{R_{S_n} R_{S_m}}\left[\gamma\left(2\left[z_{S_n} - z_{S_m}\right]\right) + \gamma\left(-2\left[z_{S_n} - z_{S_m}\right]\right)\right], \end{aligned} \tag{2.6}$$

where again $\gamma(z) = \mathrm{FT}_k\{S(k)\}$ is the coherence function of the source, which assuming a Gaussian emission spectrum is given by

$$S(k) = \frac{1}{\Delta k\sqrt{\pi}} e^{-\left[\frac{(k-k_0)}{\Delta k}\right]^2} \xleftrightarrow{\mathrm{FT}} \gamma(z) = e^{-z^2\Delta k^2}. \tag{2.7}$$

Eq. (2.6) contains three components as Eq. (2.4); background, cross-correlation and auto-correlation components. Figure 2.3 shows an example of a Fourier domain A-line in Fig. 2.3(d) for a sample with three reflectors as shown in Fig. 2.3(a) and its corresponding interferogram in k space in Fig. 2.3(c).

The cross-correlation component provides access to the signal of interest in OCT, $\sqrt{R_R R_{S_n}}$, by each reflector appearing at positions $\pm 2(z_R - z_{S_n})$ and being "broadened" by the coherence function similarly to the case of the TDOCT A-line. The apparent position of the reflectors $\pm 2(z_R - z_{S_n})$ has a factor of 2 since the interferometer

measures the round-trip distance.

There is a "mirror image" produced by the fact that $I_D(k)$ is real, hence its Fourier transform is Hermitian symmetric, that is, the positive values are the complex conjugate of the negative values, and this is represented by the double sign of $\pm 2(z_R - z_{S_n})$. This does not have an important influence if the sample is positioned entirely on one side of the zero OPL, making it is possible to extract only one half of the Fourier spectrum to filter out the mirror image.

The background component appears as a large component centered at the zero OPL. In general, it can be easily omitted from the signal since the reflectors of the sample are positioned beyond the zero OPL such that cross-correlation terms do not overlap with the background component. However, in addition to the main lobe, side lobes may appear and cause significant artifacts overlapping with the cross-correlation terms, therefore, the background is typically removed by recording the spectrum of the source by blocking the light from the sample arm and then subtracting this background spectrum to every measurement.

Autocorrelation component appears near the zero OPL if the position of the reference mirror is such that $(z_{S_n} - z_{S_m}) << (z_R - z_{S_n})$, and this way it is possible to omit this artifact, but a more direct solution is to adjust the reference reflectivity to ensure that the amplitude of cross-correlation terms is much higher than the amplitude of auto-correlation terms.

Note that the OCT signal $i_D(z)$ is given as a function of depth for a specific transverse point with coordinates (x, y) of the sample. In raster scan systems, the beam is scanned in the sample plane using galvanometer scan mirrors that deflect the light beam changing its position in the sample, and in each location (x, y) an A-line is acquired. Given that the interest so far is the axial scan, dependence on coordinates (x, y) has been omitted for simplicity.

Sensitivity improvement in FDOCT as compared to TDOCT arises from the fact that interference for all depths is captured simultaneously, considering that the signal is acquired in k space and it is known that each value in frequency domain contributes to all values in spatial domain [55]. In FDOCT, there are two approaches to measure the spectral interferogram. The most intuitive way is to use a digital spectrometer as the detector as shown in Figure 2.4, which provides the intensity signal as a function of wavenumber $I_D(k)$ in a single measurement, and it is known as spectral-domain OCT (SDOCT) [73]. Digital spectrometers are composed of a linear camera and an optical system that separates the spectral components of input light in such a way that each pixel of the detector captures the intensity of a portion of the spectrum. Imaging speed in SDOCT is limited by the acquisition rate of the linear camera and typical A-line rates are between 2 – 50 kHz [4].

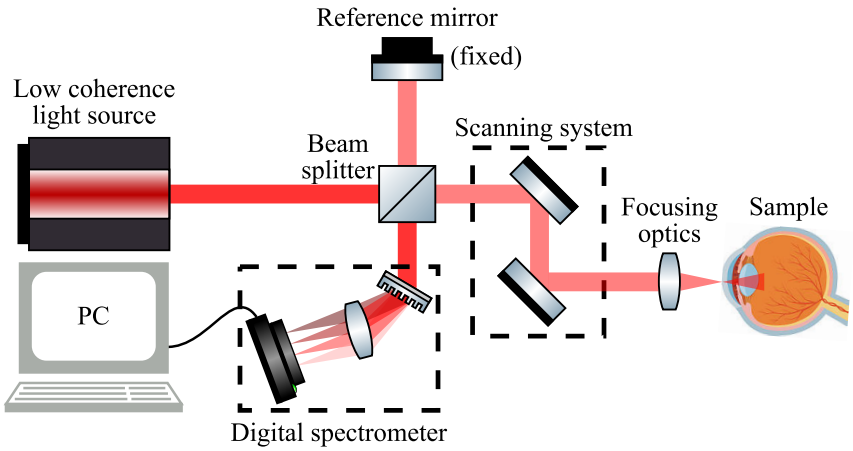

Figure 2.4: Schematic of a generic SDOCT setup based on a Michelson interferometer, where the axial scan is obtained by computing the Fourier transform of the spectral interferogram acquired with a digital spectrometer.

The second approach in FDOCT is to use a tunable light source with a narrow spectrum and to acquire the interference signal $I_D(k)$ with a single-element photodetector while the central emission wavenumber k of the light source is swept among a broad spectrum, and it is known as wavelength-swept source OCT (SSOCT) [74, 75]. It is also referred to as optical frequency domain imaging (OFDI) [89] instead of low-coherence interferometry given that, in rigorous terms, instantaneous emission of the tunable light source is considered coherent. OFDI achieves the highest imaging speed in OCT, providing A-line rates up to 200 kHz [90], or even more with specialized instrumentation [91], and it is limited by the sweeping rate of the light source. Here OFDI and SSOCT are used indistinctly although in general OFDI is used to refer to the imaging technique and SSOCT is used to refer to the OCT systems itself. A more detailed description of SSOCT systems is provided below because this is the one of interest for this work.

2.1.5. Optical frequency domain imaging

The operation of OFDI is grounded on the fact that OPL and wavenumber are conjugate variables. In low-coherence interferometry, interference is acquired by illuminating the sample with light spanning several wavenumbers while OPL is scanned. In the alternative scenario, interference corresponding to all OPLs is acquired at the same time, while illuminating the sample with light spanning a single wavenumber that is changed in time, and this is the principle of operation of OFDI [75]. Then, a Fourier transform of the spectral signal yields the depth-dependent signal.

The detection scheme in OFDI employs a single-element detector, allowing higher A-line rates than in SDOCT systems that are limited by the acquisition rate of the linear camera, which is composed of multiple pixels. The increase of imaging

speed reduces susceptibility to motion artifacts when imaging *in vivo* and allows larger scans in limited time. Tunable light sources are available in the 1–1.3 μm wavelength range, where cameras technology is not well established, hence SSOCT systems are used commonly in the 1–1.3 μm range that serves for multiple medical applications and SDOCT in the complementary 0.85–1 μm range used mainly in ophthalmology [4].

The most relevant specifications of tunable light sources in SSOCT are repetition rate, instantaneous linewidth $\delta\lambda$, tunable range $\Delta\lambda$ and tuning curve $k_i(t)$ [92]. Axial resolution is determined by central wavelength of emission λ_c and tunable range $\Delta\lambda$ equally to Eq. 2.1, $\delta_z = \frac{2\ln 2}{\pi}\frac{\lambda_c^2}{\Delta\lambda}$, thus it is independent of instantaneous linewidth. Contrarily, the depth range Δz observed within a single A-line is determined by the instantaneous linewidth as

$$\Delta z = \frac{\lambda_c^2}{4\delta\lambda} \tag{2.8}$$

and is independent of tunable range. Note that central wavelength mediate in both parameters. As a numerical example, a tunable light source with instantaneous linewidth $\delta\lambda = 0.1$ nm and tunable range $\Delta\lambda = 125$ nm centered at $\lambda_c = 1.3$ μm provides 6 μm axial resolution along 4.2 mm depth range. The same light source but with central wavelength $\lambda_c = 860$ nm provides 2.7 μm axial resolution over 2.15 mm.

Tunable curve $k_i(t)$ determines the instantaneous wavenumber as a function of time t. Ideally, this is a linear function $k_i(t) = k_0 + k_s t$ where k_0 is the initial wavenumber and k_s is the wavenumber step between consecutive instantaneous wavenumbers [93]. In practice, $k_i(t)$ is a non-linear function of time and thus linearization is required, typically performed on post-processing prior to computing the Fourier transform of the spectral interferogram, otherwise, artifacts appear degrading axial resolution [93].

The development of SSOCT systems has inherited technology from optical communications in the near-infrared spectrum that employs similar optical components such as tunable laser sources, optical fiber, and detectors [94]. In that sense, there are various types of tunable light sources relying on different principles of operations. Currently, the development of fast, stable, linear, low-cost tunable light sources is a very active area of research [95].

Lasers are optical oscillators comprising a gain medium that is pumped optically or electrically to amplify light by stimulated emission, and an optical cavity that gives coherent optical feedback for laser oscillations [96]. Semiconductor optical amplifier (SOA) is a gain medium widely used for tunable lasers because they offer a high gain in a broad bandwidth, a rapid response time, in the picosecond scale, and a

wide range of gain center wavelengths depending on the semiconductor materials [92]. One way to construct tunable lasers is to incorporate an internal or external scanning filter in the basic laser instrumentation, to select the central wavelength of the instantaneous emission. One of the first tunable lasers used in OCT applications is based on a scanning filter using a polygonal mirror and, to date, this is widespread in research and medical systems [75]. Polygon-based tunable lasers offer a high sweep rate in a wide tuning range with narrow linewidth, ideal features for OCT imaging.

In polygon-based lasers, the optical cavity includes a diffraction grating, a telescope, and a rotating polygonal mirror with tens of facets [75]. The light emitted by an SOA within a broad spectrum is reflected by the diffraction grating in such a way that there is an angular separation of spectral components. Light is relayed to the polygonal mirror through the telescope, and only the spectral component incident perpendicular to the mirror surface is reflected back to the grating and then to the SOA, providing coherent light feedback. Rotation of the polygonal mirror changes the surface angle and therefore the instantaneous spectral component with perpendicular incidence also changes [75]. The drawbacks of this scanning filter approach are that polygonal mirrors are relatively bulky and moving part.

Figure 2.5 illustrates an optic fiber-based SSOCT system using a polygon-based tunable laser. Light from the tunable laser is delivered to an optic fiber beam splitter that divides the light into the sample and reference arm. Then, reflected light from both produce interference that is detected by a photodetector and digitized. In this scheme, balanced detection is illustrated using two detectors to subtract the background signal and thus suppressing excess noise [86]. Moreover, SSOCT systems require a trigger signal to synchronize detector acquisition with the rotation of the polygonal mirror [63]. In the system of Fig. 2.5, the trigger signal is generated by a narrowband fiber Bragg grating (FBG) that reflects light of a specific wavelength. When the laser source emits this wavelength, the FBG reflects light that is detected to generates a pulse which indicates the beginning of the interferogram detection. Acquisition process is performed using N analog-to-digital conversions (ADC) dictated by a sampling clock [63].

Compact tunable lasers have been possible with vertical-cavity surface-emitting lasers (VCSEL) in conjunction with a micro-electro-mechanical mirror system (MEMS) used to vary the cavity length of the VCSEL, thereby tuning the output wavelength [97]. MEMS-VCSEL sources, however, have a limited tuning range and broad instantaneous linewidth although they are in current development to provide a powerful alternative to polygonal-based sources [98]. Current research focuses on developing akinetic tunable lasers to provide more robust and reliable light sources with the same or even better features of polygon-based sources [99].

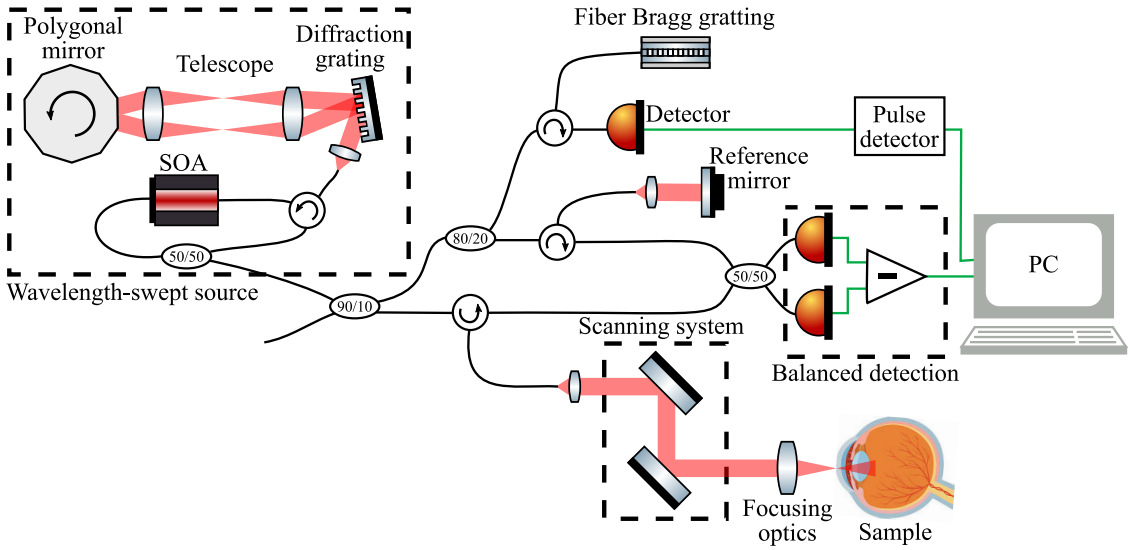

Figure 2.5: Schematic of a fiber-based SSOCT setup where the wavelength-swept source changes its instantaneous central wavelength in time due to the rotation of the polygonal mirror. The fiber Bragg grating designed to reflect a single wavelength produces a trigger signal to start the acquisition of the spectral interferogram, indicating the start of a sweep cycle of the light source.

2.1.6. Phase stability in OCT configurations

Being an interferometric technique, OCT provides the *complex amplitude* of the light backscattered by the sample, and this includes phase and amplitude information. This is an important feature of OCT because the complex amplitude provides more information than the amplitude (or intensity) alone, enabling the operation of phase-resolved functional techniques and phase-dependent post-processing [41,63,67].

In OCT, there are several undesired contributions to the phase that are considered as *phase noise*, arising from the system or the sample [47,63], making the development of phase-resolved OCT technology challenging. The ability of a system to provide repeatable phase measurements is known as *phase stability* and it exists when there is a constant phase relationship between measurements, that is when the phase difference between entirely correlated measurements is zero [47]. In phase-sensitive techniques like flowmetry, the phase difference between consecutive measurements is directly related to the flow velocity. Phase stability is crucial because phase-noise causes phase fluctuations, yielding spurious contributions to the calculation of the phase difference that ultimately results in errors in the velocity estimation [67].

Phase stability is greatly influenced by the configuration used for the axial and transverse scan, and it is possible to obtain 1D (along one axis), 2D (along two axes), or 3D (volumetric) phase stability. In SDOCT, the parallel acquisition of the entire spectral interferogram within a single measurement ensures phase stability during the acquisition of every A-line, thus the axial axis is phase-stable. In addition, the

high repeatability of spectrometers ensures phase stability along successive A-lines, despite being measured at different times while scanning the position of the beam, hence in principle, SDOCT provides volumetric phase stability. However, there are sources of phase noise that prevent from obtaining 3D phase stability in experimental scenarios: one arising from sample motion that is detailed in Section 2.3.4, and the second arising from the galvanometer scanning system that adds a phase offset depending on the instantaneous angle of the mirrors, because of the separation of the pivot position of each galvanometer mirror and the back focal plane of the scan lens [47]. Although there is a physical limitation in positioning the pivot point of both galvanometers mirrors at the back focal length of the scan lens, precise alignment of one mirror would ensure phase stability along its corresponding lateral scan axis, making it possible to obtain 2D phase stability in SDOCT [100].

In SSOCT systems, achieving phase stability has been more challenging than in SDOCT because each component of the spectral interferogram is acquired sequentially in time and not in parallel like in a spectrometer. In principle, this is not a limitation if experimental conditions of the system during A-line acquisition do not change, but there is a particular issue regarding the trigger signal that has a detrimental effect on phase stability. SSOCT systems require a trigger signal to synchronize the A-line acquisition with the wavelength sweep of the light source [63], for instance, using a Fiber Bragg grating like in Fig. 2.5. However, the fast sweeping cycle of the light source demands precise electronics to obtain perfect synchronization, but in practice, this is not the situation and there is a time delay or *jitter* in the sampling clock of the detector with respect to the trigger signal. As a consequence, acquisition starts arbitrarily within the sweep cycle of the light source [63].

A jitter in synchronization causes a shift δk in the acquired spectral interferogram, thus the measured signal is $\tilde{I}_D(k) = I_D(k - \delta k)$. Depth-dependent signal obtained as $i_D(z) = \mathrm{FT}_k\{\tilde{I}_D(k)\}$ results in [101]

$$\begin{aligned} \tilde{i}_D(z) &= \mathrm{FT}_k\{I_D(k - \delta k)\} \\ &= \mathrm{FT}_k\{I_D(k)\}e^{-i2\pi z\delta k} \\ &= i_D(z)e^{-i2\pi z\delta k}, \end{aligned} \tag{2.9}$$

with $i_D(z) = \mathrm{FT}_k\{I_D(k)\}$ being the unmodified depth-dependent A-line. Note that effect of spectral shift only impacts the phase of the A-line by the factor $e^{-i2\pi z\delta k}$ that represents a phase ramp with slope $-2\pi\delta k$, known as *phase-jitter* noise, but the amplitude $|\tilde{i}_D(z)| = |i_D(z)|$ remains unchanged, thereby traditional structural OCT image based on the intensity $|\tilde{i}_D(z)|^2 = |i_D(z)|^2$ is not affected. The random behavior of jitter in synchronization causes that the spectral shift δk varies randomly between spectral interferograms, and this dramatically impacts phase stability in raster scan

systems because A-lines are captured sequentially in time while displacing the beam in the sample plane, inducing spatially-varying phase-jitter noise.

In addition to phase-jitter, random phase offsets can be induced in some SSOCT systems that are equipped with a frequency shifter used to double the axial imaging range by eliminating the ambiguity between positive and negative optical path delays [102].

An approach to avoid phase-jitter is the use of k-clocks that produce a sample clock linear in k using a Mach-Zehnder interferometer [103]. In standard systems, signal acquisition is performed linearly in time with N ADC following an internal electronic sample clock. With a k–clock, ADC is performed linearly in k with certainty. Therefore, the use of a k–clock avoids phase-jitter because the uncertainty in trigger signal is solved, at the same time that acquired signal is linear in k eliminating the need for signal linearization in post-processing. Although there are k-clocked SSOCT systems available [62], they are not widespread because of the need for additional hardware, thus phase-jitter is a very common issue affecting standard research and medical OCT systems [89]. Additionally, even using a k-clock, SSOCT systems are susceptible to galvanometer and sample motion phase noise, affecting its phase stability [64].

In the previous descriptions, it is possible to note that phase stability is very limited in raster scan systems, whether SDOCT or SSOCT, because the transverse scan is performed by scanning the beam position in time. Parallel acquisition of A-lines for different transverse locations can be achieved with extended-field systems where light is projected onto the sample in an extended area. In line-field SDOCT (LF-SDOCT), the sample is illuminated with a line-shaped beam, produced by a cylindrical lens, and the linear detector in the digital spectrometer is replaced by a two-dimensional detector: one dimension corresponds to the k space and the orthogonal dimension corresponds to the transverse fast scan axis [104, 105]. Hence, a single acquisition of the detector provides a B-scan view, and a single galvanometer is required to scan the beam along the slow scan axis providing three-dimensional images. Parallel acquisition along the fast scan axis ensures phase stability *in vivo* in this axis as long as the acquisition rate is relatively fast compared to the velocity of the sample motion, nonetheless, the slow scan axis typically remains phase-unstable [105].

TDOCT and SSOCT systems allow full-field (FF) acquisition [61, 106] by making three general modifications: an extended collimated beam is used to illuminate the sample; the single-element detector is replaced by a two-dimensional detector; and additional optical lenses are used to image the sample plane on the detector plane. With these modifications, a single axial scan provides an entire tomogram with volumetric phase stability, even *in vivo* if the acquisition rate is relatively

fast compared to the velocity of the sample motion. Figure 2.6 illustrates simple schematics of LF-SDOCT and FF-SSOCT systems.

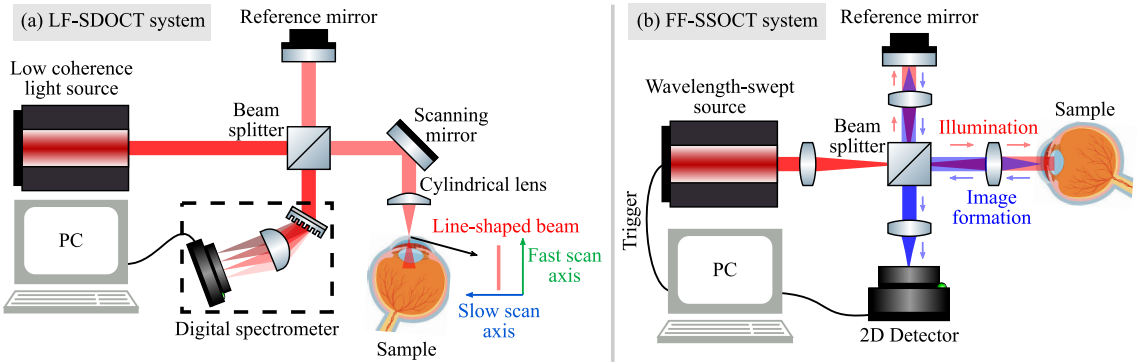

Figure 2.6: Schematic of generic (a) LF-SDOCT setup for the acquisition of a B-scan in a single detector shot and (b) FF-SSOCT setup for the acquisition of a tomogram in a single cycle of the wavelength-swept source. The red path illustrates the illumination beam and the blue path the image formation on the detector plane for a point.

Extended-field OCT systems are custom configurations used in particular scenarios, like in the CAC research area, because they offer sufficient phase stability [61,69]. However, they are not widespread given that they have a more complex optical design, including 2D detectors that are not well developed in terms of speed and sensitivity in the near-infrared range, and more importantly, they are more prone to multiple scattering [107]. Scattered light in tissue can be divided into two components: single scattering and multiple scattering (MS). The former is the backscattered signal of interest in OCT and the latter is an undesired component arising from light that is scattered multiple times following random paths that reach the detector, but it does not contribute direct information to the OCT signal due to its random properties [108]. Raster scan systems have an intrinsic rejection to MS because of confocal gating, that is, the focused beam scans a small region of the sample in a limited field of view (FoV), contrary to extended detection that is more prone to collect MS photons given that the FoV during each measurement is larger [107].

There is not a general way to evaluate phase stability. Typically, assessment is performed by visually inspecting phase images, or more specifically, histograms or images of phase differences between adjacent A-lines [109]. A quantitative approach is to image a coverslip or a reflective surface; because such a reference surface is expected to have a constant phase, the estimation of phase differences between consecutive A-lines yields an estimation of phase stability [109]. One possible configuration to image the coverslip is to acquired A-lines while sweeping the beam with the galvanometer system, thus acquiring a B-scan, or simply by acquiring multiple A-lines in the same position with a static beam what is known as a C-scan. Typical, the

standard deviation (STD) of phase differences is provided and used as a quantitative reference of phase stability. For instance, phase stability of 0.32–5.2 mrad STD has been reported for SDOCT [67, 110], whereas 32 mrad STD has been reported for SSOCT systems with a polygon mirror-based laser [111] using phase stabilization methods, showing that this configuration is indeed more prone to phase instabilities than SDOCT, but higher phase stability of 1.5 mrad STD using Akinetic swept laser has been obtained with SSOCT systems [112].

2.2. Modeling the acquisition of the complex OCT signal

In the previous section, the OCT experiment was described and analyzed from an interference perspective to derive the acquisition of the axial scan that provides the depth-dependent signal i_D through optical interferometry. Hereafter, the OCT signal is represented by S for consistency with the general bibliography used to derive the following models. The measured OCT signal S corresponds to the complex field of light backscattered by the sample, however, the ultimate aim in OCT is not to know the backscattered light S itself but to know the *scattering potential* of the sample η that produced the measured signal, because η is directly related to the sample structure [113]. More specifically, in OCT the optical beam probe is used to measure η indirectly; *the acquired signal S contains the sample scattering information modified by the effect of the optical system.* In the ideal situation, the effect of the optical system is not significant and the measured signal is directly related to η. This is the case of systems with aberration-free optical beams where imaging is diffraction-limited inside the depth of field and the theoretical lateral resolution is achievable, but in the presence of aberrations or outside the depth of field of the beam, the optical field is distorted and effective lateral resolution is reduced [113].

Scattering theory can be used to derive a model of the image formation process that relates the measured signal with the sample structure, known as *forward model* [113, 114]. Inversion of the forward model results in the *inverse scattering model* that allows recovering an approximate sample structure from the backscattering signal [33]. Solutions to the inverse scattering model brought the development of computational techniques for aberration correction of OCT tomograms [33–35]. In this section, the forward model is presented and the subsequent section surveys solutions to the inverse scattering model to correct aberrations in post-processing, but first, a conceptual description of lateral-resolution–DoF trade-off is given.

2.2.1. Confocal gating for lateral scan in OCT

In raster scan systems, the transverse scan is performed using confocal gating resulting from the distribution of the focused beam as shown in Figure 2.7. When light is

focused on the sample plane, the illuminated cross-sectional area defines the lateral resolution and it can be given in terms of the input beam diameter [34]. Typically, at the back focal length of the optical system, the probe beam with central wavelength λ_c is a Gaussian beam with a $1/e^2$–diameter D, and after the optical system, light is focused at the front focal length f in a spot with a $1/e^2$–radius w_0, that defines the diffraction-limited lateral resolution δx [4]

$$\delta x = 2w_0 = \frac{4\lambda_c}{\pi}\frac{f}{D}, \tag{2.10}$$

where $\frac{D}{2f}$ = NA is the numerical aperture of the optical system. The inverse relationship between NA and δx means that high NA systems produce small focused spots and therefore provide fine transverse resolution.

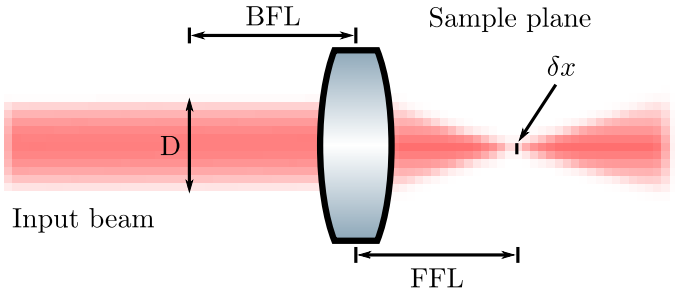

Figure 2.7: Schematic of focusing optics in OCT. Input collimated beam of diameter D at the back focal length (BFL) is focused into a focal point of diameter δx at the front focal length (FFL).

Due to convergence and divergence of the optical beam, the $1/e^2$–radius of the focusing beam denoted as $w(z)$ varies with depth z. Setting $z = 0$ at the front focal plane, $w(z)$ can be expressed as [115]

$$w(z) = w_0\sqrt{1 + \left(\frac{z\lambda_c}{\pi w_0^2 n}\right)^2}, \tag{2.11}$$

where n is the refractive index of the propagating medium.

Eq. 2.11 shows that diffraction-limited resolution is only possible at the focal plane ($z = 0$) and is degraded for other planes. However, for distances z relatively close to the focal plane, the change of spot size is relatively small. The confocal parameter b is defined as the distance within which the spot size is smaller than $\sqrt{2}\delta x$ and thus resolution can be considered as nearly constant, and it is given by [115]

$$b = 2z_R = \frac{\pi\delta x^2}{\lambda}, \tag{2.12}$$

where z_R is known as the Rayleigh range. The confocal parameter defines the region where defocus is negligible and is also referred to as depth of field (DoF). It is proportional to the beam spot size squared and this establishes the lateral-resolution–DoF trade-off; high NA systems provide high-resolution images in a limited DoF whereas low NA systems provide low-resolution images in an extended DoF. In general, OCT systems employ low NA (between 0.01 and 0.15) to obtain tomograms with nearly focal resolution throughout the whole axial scan and this has limited transverse resolution in OCT to $\sim> 10$ μm. In certain applications, high NA systems are used and known as optical coherence microscopy (OCM) [4].

To illustrate confocal gating and its relation to numerical aperture, Figure 2.8(a) shows the focused beam produced by two optical systems in different NA regimes, for a wavelength $\lambda_c = 1$ μm. Low NA system (red) produces a large spot size but its size remains nearly constant along a large DoF. In contrast, the second system (blue) has a NA four times larger producing a spot size four times smaller but its size increases abruptly reducing the DoF by 4^2 times. Fig. 2.8(b) shows the square relationship between confocal parameter and transverse resolution, indicating the corresponding values of the NA used in Fig. 2.8(a).

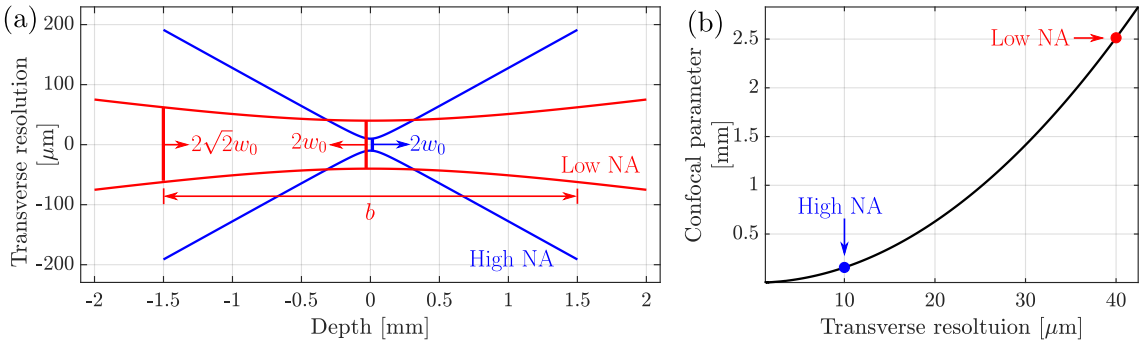

Figure 2.8: Illustration of confocal gating for light with $\lambda_c = 1\mu$m. (a) A focused beam produced by two optical systems with relatively low and high NA. (b) Relation between confocal parameter and transverse resolution.

With this qualitative description of the resolution-DoF–trade-off, it is possible now to analyze how this impacts the acquired complex signal.

2.2.2. Forward model

This section presents the forward model (FM) that relates the measured OCT signal to the sample structure considering the effect of the optical system using a model for the image formation process. In the FM, the propagation of the Gaussian probe beam is included to derive an expression for the interference signal that also considers the effect of confocal scan [113, 114]. From Fourier optics theory, the acquired signal $S(x, y; k)$ for wavenumber k at transverse coordinates (x, y) can be modeled

as $S(x,y;k) = h(x,y,z;k) \otimes \eta(x,y,z)$, that is the convolution (denoted by $\otimes$) of the system coherent point spread function (PSF) $h(x,y,z;k)$ with the scattering potential of the sample $\eta(x,y,z)$ [116],

$$S(x,y;k) = \iiint h(x-x', y-y', z';k)\eta(x',y',z')\mathrm{d}x'\mathrm{d}y'\mathrm{d}z', \tag{2.13}$$

where the integration over z' indicates that light is captured simultaneously for all depths, as occurs in Fourier-domain detection. Strictly speaking, $h(x,y,z;k)$ is the system's impulse response, but it is typically denoted simply as the PSF [117]. $h(x,y,z;k)$ can be expressed as the product of the incident and detection complex probe beams, $g_i(x,y,z;k)$ and $g_d(x,y,z;k)$ respectively, but given that OCT is based on a reflection (double-pass) geometry, the incident and collection beams are identical to $g(x,y,z;k)$, hence [113]

$$h(x,y,z;k) = k^2|A(k)|^2 g^2(-x,-y,z;k), \tag{2.14}$$

where $|A(k)|^2$ is the power spectral density and the inversion of lateral coordinates (x,y) is due to the reflection geometry.

To derive a model for the probe beam $g(x,y,z;k)$, first consider that the beam at the focal plane $z = z_0$ and transverse coordinate $\mathbf{r_0} = (x,y,z_0)$ is a normalized Gaussian probe beam

$$g_0(\mathbf{r_0};k) = \frac{1}{2\pi w_0^2(k)} e^{-\mathbf{r_0}^2/[2w_0^2(k)]}, \tag{2.15}$$

with waist radius $w_0(k) = \alpha/k$ for wavenumber k and $\alpha = \pi/\mathrm{NA}$. Using plane-wave decomposition with transverse frequency coordinate $\mathbf{q} = (q_x, q_y, 0)$, the beam at $\mathbf{r} = (x,y,z)$ in any plane z is described as [113]

$$g(\mathbf{r};k) = \frac{1}{(2\pi)^2} \iint e^{i(z-z_0)\sqrt{k^2-\mathbf{q}^2}} e^{-\mathbf{q}^2\alpha^2/2k^2} e^{i\mathbf{q}\cdot\mathbf{r}} \mathrm{d}^2\mathbf{q}. \tag{2.16}$$

Using Eqs. 2.13 and 2.14, it is possible to model the measured OCT interference signal taking into consideration the beam distribution, as explained in detail in Refs. [113, 118], by means of the expression

$$S(\mathbf{r}';k) = \frac{A(k)}{(2\pi)^2 k} \iiint f^2(\mathbf{r}-\mathbf{r}';k)\eta(\mathbf{r})\mathrm{d}^2\mathbf{r}\mathrm{d}z, \tag{2.17}$$

where the term $f^2(\mathbf{r};k)$ is given by

$$f^2(\mathbf{r};k) = \frac{1}{8\pi^2}\left(\frac{\alpha^2}{k^2}+\frac{iz}{k}\right)^{-1}\iint e^{-\mathbf{q}^2\alpha^2/4k^2}e^{iz\sqrt{4k^2-\mathbf{q}^2}}e^{-i\mathbf{q}\cdot\mathbf{r}}\mathrm{d}^2\mathbf{q}. \tag{2.18}$$

To understand Eq. 2.17, note that $\mathbf{r}' = (x', y', z_0)$ is the instantaneous transverse position of the probe beam during a raster scan. The signal $S(\mathbf{r}', k)$ measured for the instantaneous wavenumber k when the beam is located at the instantaneous position $\mathbf{r}'$, **is the contribution of all point scatterers in the sample weighted by the function** $f^2(\mathbf{r}-\mathbf{r}';k)$, and scaled by a value proportional to the light source intensity for k, $A(k)$. Finally, a Fourier transform of $S(\mathbf{r}';k)$ with respect to k yields the depth-dependent signal $S(\mathbf{r}', z)$. In regard to $f^2(\mathbf{r}-\mathbf{r}';k)$, the factor $\frac{1}{8\pi^2}\left(\frac{\alpha^2}{k^2}+\frac{iz}{k}\right)^{-1}$ can be considered as a depth-dependent signal-loss factor that describes the signal reduction far from the focal plane, $e^{-\mathbf{q}^2\alpha^2/4k^2}$ is related to the Fourier spectrum of the Gaussian beam, the factor $e^{iz\sqrt{4k^2-\mathbf{q}^2}}$ encompasses both the interference and the PSF broadening effect, responsible of the signal blurring, and last factor $e^{-i\mathbf{q}\cdot\mathbf{r}}$ is the Fourier transform kernel, since Eq. 2.18 is actually a Fourier integral.

To illustrate the forward model, Figure 2.9 shows an example of an OCT B-scan image simulated using Eq. 2.17. For this purpose, a collection of 128 point scatterers with random positions was defined within an axial and lateral field of view (FoV) of 820×450 μm as depicted in Fig. 2.9(a). The light source had $\Delta\lambda = 150$ nm and $\lambda_c = 1.310$ μm providing an axial resolution of $\delta z = 5$ μm. The numerical aperture was NA $= 0.25$, a relatively high value, resulting in lateral resolution $\delta x = 5$ μm throughout a depth of field of $b = 30$ μm, producing the Gaussian beam shown in Fig. 2.9(b), where the focal plane is clearly located at $z_0 = 0$. To generate the simulated OCT image shown in Fig. 2.9(c), the location of the Gaussian beam is changed iteratively, and in each location, the contribution of all point scatterers weighted by $f^2(\mathbf{r}-\mathbf{r}';k)$ is computed using Eq. 2.17. At the n-th iteration, the location of the Gaussian beam is $\mathbf{r}'_m = (n\mathrm{d}x - \frac{\Delta x}{2}, 0, z_0)$, where Δx is the lateral FoV and $\mathrm{d}x = 1.75$ μm is the sampling step which is smaller than Nyquist sampling, given by $\delta x/2$, in order to fulfill Nyquist theorem for correct sampling.

The lateral blurring due to the convergence and divergence of the probe beam is evident in Fig. 2.9(c). Resolution within the confocal region marked as b is diffraction-limited, so that point scatterers inside b appear in focus, like the one inside the red rectangle, contrary to point scatterers away from the focal plane which appear blurred in the lateral axis as a consequence of beam size increase, such as the one in the blue rectangle. Note that the superposition of signal from different point scatterers causes interference, like the two superimposed points in the yellow rectangle. When the number of point scatterers increases, random interference occurs

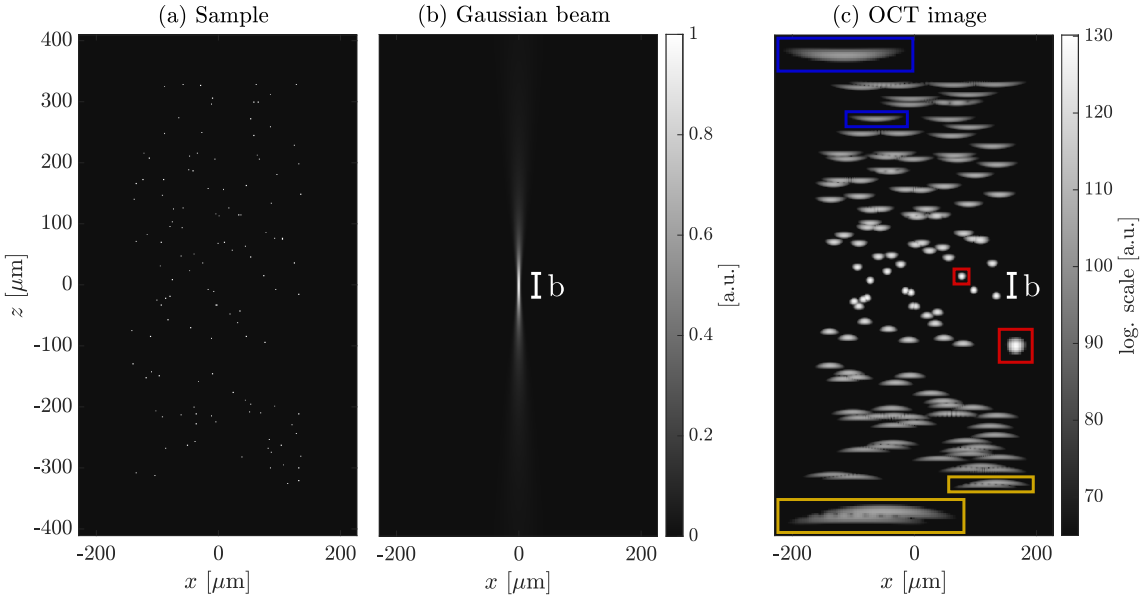

Figure 2.9: Simulation of an OCT image in the high-NA regime. (a) A sample consisting of randomly located point scatterers, (b) Gaussian beam of the system with NA= 0.25, and (c) OCT image simulated using the forward model, displayed in logarithmic scale.

and this phenomenon gives rise to speckle [49].

It is important to remark that the confocal effect is not restricted to the lateral axis. The factor $e^{iz\sqrt{4k^2-\mathbf{q}^2}}$ in Eq. (2.18) can be written as $e^{izq_z(k,\mathbf{q})}$, where $q_z = \sqrt{4k^2 - \mathbf{q}^2}$ is the axial frequency coordinate of the object [116]. Because q_z encompasses k and $\mathbf{q}$, there is a mixing of the lateral and axial information that produces a coordinate warping, from the sample's frequency coordinates (q_x, q_y, q_z) to the signal's frequency coordinates (q_x, q_y, k) [113]. As a consequence, there is an apparent object curvature away from the focal plane as observed in the blue inset of Fig. 2.9(c). The signal warping occurs because the object axial frequency component q_z is not measured directly but through the light wavenumber k [119]. In other words, the object frequency content is in the (q_x, q_y, q_z) space, but the measured signal is the $(q_x, q_y, \frac{1}{2}\sqrt{q_x^2 + q_y^2 + q_z^2})$ space. This phenomenon is significant in the high-NA regime, and for the low-NA regime, an approximation can be made to simplify the FM as will be discussed in the next section.

For a comparison between high- and low-NA regimes, Figure 2.10 illustrates the result of imaging the same sample of Fig. 2.9(a) changing the NA to 0.1, resulting in a lateral resolution of 12.5 μm throughout a depth of field of 190 μm. The Gaussian beam produced with this NA has a more constant beam size along depth, as shown in Fig. 2.10(b) in contrast to the previous NA used for Fig. 2.9(b). As a result, resolution loss away from the focal plane is less abrupt, at the expense of presenting a larger diffraction-limited spot size.

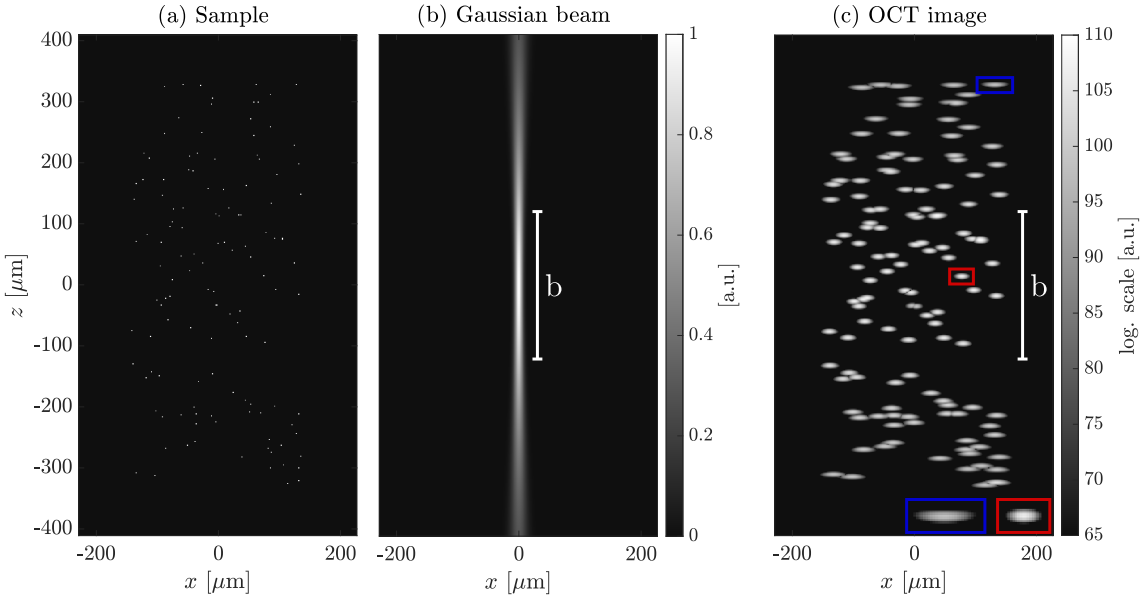

Figure 2.10: Simulation of an OCT image in the low-NA regime. (a) A sample consisting of randomly located point scatterers, (b) Gaussian beam of the system with NA= 0.1, and (c) OCT image simulated using the forward model, displayed in logarithmic scale.

2.3. Refocusing and computational aberration correction techniques in OCT

In the FM of Eq. 2.17, the OCT signal S is given by the sample potential η modified by the function f^2 [118]. From this model, it is possible to computationally obtain an approximate scattering sample potential $\tilde{\eta}$ by correcting the undesired effects present in the acquired signal S, that so far is only defocus due to the beam propagation, but other aberrations may be considered as well with further extensions presented below. There are several computational aberration correction techniques that are explained in the following sections. Some are oriented to correct for defocus to provide focal resolution throughout all depths, and others are oriented to correct for other types of aberrations that depend on the specific imaging system or even on the sample itself.

To retrieve an approximate scattering sample potential from the acquired signal it is necessary to invert the forward model, which is known as an inverse scattering problem [33]. In simple words, the FM gives the backscattering signal produced for a given scattering potential, while the inverse model gives the scattering potential that produced a given backscattering signal, and the latter process is the interest in CAC.

For the derivation of CAC techniques, it is convenient to introduce the forward model in Fourier-domain [120]. To do so, the convolution theorem can be used to

rewrite Eq.(2.13) as

$$\hat{S}(q_x, q_y; k) = \int \hat{h}(q_x, q_y, z'; k)\hat{\eta}(q_x, q_y, z')\mathrm{d}z', \tag{2.19}$$

where $\hat{S}(q_x, q_y; k) = \mathrm{FT}_{x,y}\{S(x, y; k)\}$, $\hat{h}(q_x, q_y, z; k) = \mathrm{FT}_{x,y}\{h(x, y, z; k)\}$ is the depth-dependent frequency response of the PSF, and $\hat{\eta}(q_x, q_y, z) = \mathrm{FT}_{x,y}\{\eta(x, y, z)\}$. Using an asymptotic approximation for the far-from-focus and near-focus cases [116], Eq. (2.19) can be simplified to

$$\hat{S}(q_x, q_y; k) = H(q_x, q_y; k) \int \hat{\eta}(q_x, q_y, z')e^{iz'\sqrt{4k^2-\mathbf{q}^2}}\mathrm{d}z', \tag{2.20}$$

where $H(q_x, q_y; k)$ is the space-invariant axial and lateral frequency response of the PSF, that is directly related to the optical transfer function of the system. In Eq.(2.19), the Gaussian beam is not assumed to be ideal, contrary to the derivation of the FM in Eq. (2.17), thus $H(q_x, q_y; k)$ is a general function that may describe any aberration and not only defocus. Computational aberration correction makes use of the FM in frequency domain to reconstruct an approximate sample scattering potential [120].

In the notation used hereafter, the tilde accent ˜ is used to denote that a quantity is a numerical estimation of the true quantity. For instance, $\tilde{\eta}$ is an estimation of η using any of the CAC models presented above.

2.3.1. Interferometric synthetic aperture microscopy

Interferometric synthetic aperture microscopy (ISAM) is a solution to the inverse scattering problem in OCT [33, 121], and actually it is very similar to procedures used in synthetic aperture radar (SAR) [122] and from this similarly arises its name. Eq. (2.20) can be considered as a Fourier integral with conjugate coordinates z' and $q_z = \sqrt{4k^2 - \mathbf{q}^2}$, thus it is possible to write

$$\hat{S}(q_x, q_y; k) = H(q_x, q_y; k)\hat{\tilde{\eta}}(q_x, q_y, q_z), \tag{2.21}$$

where $\hat{\tilde{\eta}} = \mathrm{FT}_{x,y,z}\{\eta(x, y, z)\}$ is the 3D Fourier transform of the sample scattering potential. Eq. 2.21 is a one-to-one mapping between $\hat{S}$ and $\hat{\tilde{\eta}}$, contrary to convolution equation that is an all-to-all mapping between S and η. The principle of operation of ISAM is to re-sample the Fourier spectrum of the acquired signal $S(x, y; k)$ in order to revert the coordinate warping, thereby the approximate scattering sample

potential $\tilde{\eta}(x, y, z)$ can be expressed as [121]

$$\tilde{\eta}(x, y, z) = \frac{1}{\rho(z)} \mathrm{FT}^{-1}_{q_x, q_y . q_z} \left\{ \left[H^{-1}(q_x, q_y; k) \hat{S}(q_x, q_y; k) \right] \Big|_{k=\frac{1}{2}\sqrt{q_x^2+q_y^2+q_z^2}} \right\}, \tag{2.22}$$

where $\rho(z) = -1/z$ countervails signal loss when far from focus. Eq. 2.22 consist in several steps: 1) computing the Fourier transform of the acquired spectral signal along transverse spatial coordinates, 2) re-mapping coordinates from k to q_z using the relation $k = \frac{1}{2}\sqrt{q_x^2 + q_y^2 + q_z^2}$, known as the Stolt mapping [123], and then 3) computing the three-dimensional inverse Fourier transform $\mathrm{FT}^{-1}\{\cdot\}$. For ISAM, an ideal Gaussian beam is generally assumed, hence H^{-1} is a weighting factor that will not introduce significant image distortion, thus it is usually set to unity. Normalization using $1/\rho(z)$ is not appropriate in practical terms to compensate for signal loss away from focal plane, thus it is commonly omitted or replaced with other depth normalization function.

ISAM, first proposed by Ralston *et al.* [33], has been used in the OCT community, especially in high-resolution imaging where DoF is greatly reduced and computational correction of defocus is a key tool for extending the DoF [124–127], being the signal loss the major constrain. Extensions have been made to different imaging geometries and functional imaging, such as rotationally-scanned ISAM for endoscopic OCT [118,128], and polarization-sensitive ISAM [129]. Furthermore, the development of ISAM have enable real-time *in vivo* visualization [130–132].

2.3.2. Digital refocusing

ISAM reconstruction brings to focus all depths simultaneously by making use of the 3D frequency content of the tomogram. In relatively low numerical aperture systems (NA < 0.15) the re-sampling curve approximates a linear path which means that frequency content in not spread along depth, hence a 2D correction in the transverse plane determined for each plane z independently is sufficient [34,133] rather than a 3D correction as in ISAM. To isolate a single plane z_d, inverse Fourier transform along k of Eq.(2.20) is computed and evaluated at $z = z_d$ as

$$\hat{S}(q_x, q_y; z_d) = \int H(q_x, q_y; k) \int \hat{\eta}(q_x, q_y, z_d) e^{iz\sqrt{4k^2 - \mathbf{q}^2}} e^{-i2z_d k} \mathrm{d}z \mathrm{d}k. \tag{2.23}$$

Replacing $k = k_c + k'$, being k' the difference between k and central wavenumber k_c, the term $(k'/k_c)^2$ is relatively small enough to be neglected, allowing to express

$q_z = \sqrt{4k^2 - \mathbf{q}^2}$ under the paraxial approximation as [133]

$$q_z = 2k_c - \frac{\mathbf{q}^2}{4k_c} + 2k'. \tag{2.24}$$

Replacing q_z in Eq.(2.23), as well as using convolution theorem to rewrite Fourier integral along k', it is possible to obtain [133]

$$\begin{aligned}
\hat{S}(q_x, q_y; z_d) &= \int H(q_x, q_y; k') \int \hat{\eta}(q_x, q_y, z_d) e^{iz(2k_c - \mathbf{q}^2/4k_c + 2k')} e^{-i2z_d(k_c + k')} \mathrm{d}z\mathrm{d}k' \\
&= \int H(q_x, q_y; k') \int \hat{\eta}(q_x, q_y, z_d) e^{i2(z - z_d)k_c} e^{-iz\mathbf{q}^2/4k_c} e^{i2(z - z_d)k'} \mathrm{d}z\mathrm{d}k' \\
&= H(q_x, q_y; z_d) \otimes \left[\int \hat{\eta}(q_x, q_y, z_d) e^{i2(z - z_d)k_c} e^{-iz\mathbf{q}^2/4k_c} \delta(2z - 2z_d) \mathrm{d}z \right] \\
&= H(q_x, q_y; z_d) \otimes \left[\hat{\eta}(q_x, q_y, z_d) e^{-iz_d\mathbf{q}^2/4k_c} \right],
\end{aligned} \tag{2.25}$$

where the convolution is performed along axial axis. The depth-dependent part of $H(q_x, q_y; z_d)$ is related to the axial PSF that can be approximated to a delta function, so that $H(q_x, q_y; z) \propto H(q_x, q_y)\delta(z - z_d)$, which can be replaced in Eq. (2.25) to obtain its inverse Fourier transform along $\mathbf{q}$ as

$$S(x, y; z_d) = \mathrm{FT}^{-1}_{q_x, q_y} \left\{ H(q_x, q_y) \hat{\eta}(q_x, q_y; z_d) e^{-iz_d\mathbf{q}^2/4k_c} \right\}. \tag{2.26}$$

Eq. (2.26) is an expression with a form widely known in digital refocusing methods based on scalar diffraction models [115, 134, 135] such as the Fresnel propagator [34], where the exponential term is a quadratic phase term responsible of depth-varying defocus. A straightforward inversion of Eq. (2.26) provides an approximate refocused sample scattering potential by [133]

$$\tilde{\eta}(x, y; z_d) = \mathrm{FT}^{-1}_{q_x, q_y} \left\{ H(q_x, q_y) \hat{S}(q_x, q_y; z_d) e^{iz_d\mathbf{q}^2/4k_c} \right\}. \tag{2.27}$$

Similarly to ISAM, an ideal Gaussian beam can be assumed and H is set to unity. Reconstruction using digital refocusing of Eq.(2.27) is not complex and implementation is rather simple compared to ISAM, but there are conceptual differences with ISAM reconstruction. In digital refocusing, each depth is brought to focus independently, applying the suitable quadratic phase term, whereas ISAM reconstruction restores the entire volume simultaneously by re-sampling the signal in the Fourier domain. More importantly, due to the paraxial approximation in Eq.(2.24), digital refocusing methods are valid only for low-NA regimes, where there is no

warping of coordinates that mixes lateral and axial information. Digital refocusing is illustrated in Figure 2.11 for the low-NA case of the simulated data in Fig.2.10, and note that digital refocused image of Fig. 2.11(c) exhibit diffraction-limited resolution throughout all depth.

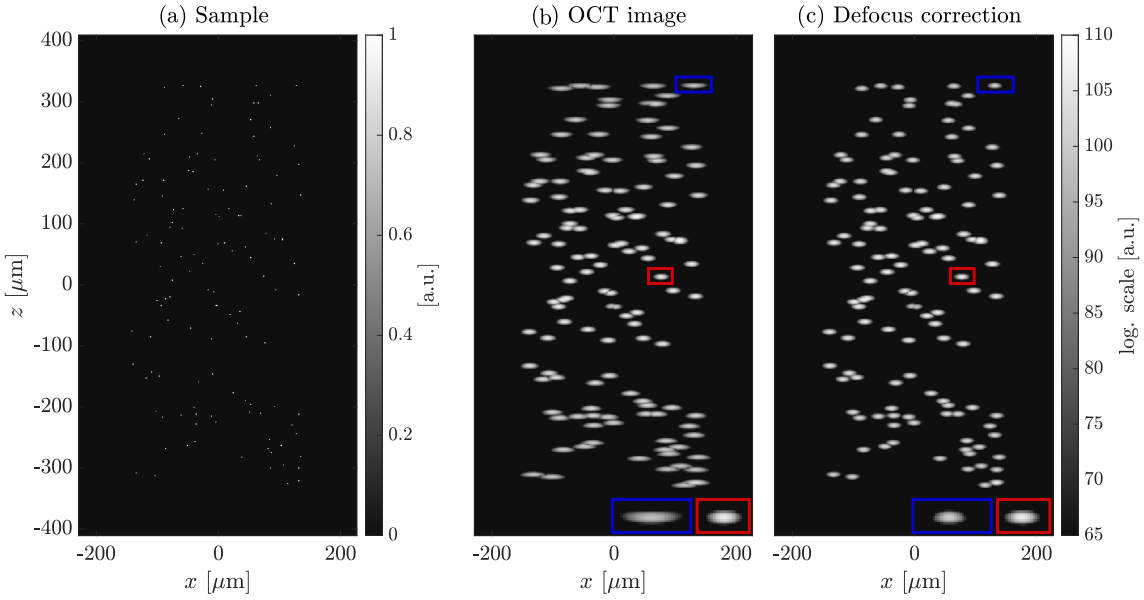

Figure 2.11: Illustration of digital refocusing. (a) A sample consisting of randomly located point scatterers, (b) OCT image simulated using the forward model, (c) digital refocused. (b) and (c) are displayed on logarithmic scale.

2.3.3. Computational adaptive optics

Aberrations are wavefront distortions with respect to a reference wavefront that affect image quality in imaging techniques such as OCT [45]. Several applications in OCT have benefited from aberration correction, whether using specific optical systems [136–139], hardware-based adaptive optics [36,44] or computational adaptive optics [46,61,62,140]. For instance, in retinal imaging, the probe beam is focused onto the retina using the optical system of the eye itself (cornea/lens) that may produce a distorted wavefront affecting image quality [39]. In particular, the wavefront in high-NA systems is more susceptible to be distorted by imperfections of the optical systems or even the sample itself.

Defocus introduced in the propagation of light is intrinsic to the Gaussian probe beam, for this reason, it is not considered as an optical aberration; in this case, aberrations are wavefront deviations from the ideal wavefront of a Gaussian beam. This can be noted in Eq.(2.20), where defocus arises from the exponential term whereas wavefront distortions can be modeled by $H(q_x, q_y; k)$ that is related to the effective generalized pupil of the optical system [120], which results from the

convolution of the illumination and detection generalized pupils, that are identical in OCT given the double-pass geometry.

Recalling the forward model in frequency domain, it is possible to invert Eq.(2.21) to obtain an aberration-corrected OCT signal as

$$\tilde{\hat{S}}(q_x, q_y; k) = H^{-1}(q_x, q_y; k)\hat{S}(q_x, q_y; k), \tag{2.28}$$

where $H^{-1}(q_x, q_y; k)$ acts as a frequency filter, which depends on spectral and spatial frequency domains, therefore it can address chromatic aberrations [120]. Given the relatively narrow spectrum of the light sources used in OCT, in practical scenarios it is convenient to assume a k-independent filter $H(q_x, q_y)$, which is the same for all depths [120]. In hardware-based adaptive optics (AO), the correction filter $H^{-1}(q_x, q_y)$ is applied directly *in situ* to compensate for the distortions of the Gaussian beam [36], but, because coordinate re-sampling is not included in this correction, $\tilde{S}(q_x, q_y; k)$ is an aberration-corrected signal rather than the sample scattering potential, it means that defocus will still be present in the acquired images. To correct for defocus using AO, a depth-dependent phase filter is necessary but it is not possible with current hardware such as deformable mirrors. In the case of computational adaptive optics (CAO), the filter is applied in post-processing [35], enabling the combination of CAO with ISAM or digital refocusing to obtain aberration-free images with focal resolution throughout all depths, namely $\tilde{\eta}(x, y, z)$ [141]. In ISAM reconstruction, $H^{-1}(q_x, q_y; k)$ is already included in Eq.(2.22) because $\tilde{\hat{S}}(q_x, q_y; k)$ is written explicit in Eq.(2.22). For low-NA regime, the depth-invariant filter $H(q_x, q_y)$ can be generalized in Eq.(2.27) to a depth-dependent filter $H(q_x, q_y; z_d)$ that includes the exponential term, resulting in [35, 120]

$$\tilde{\eta}(x, y; z) = \mathrm{FT}^{-1}_{q_x, q_y}\left\{H^{-1}(q_x, q_y; z)\hat{S}(q_x, q_y; z)\right\}. \tag{2.29}$$

In this case, defocus in treated as an aberration contained in the correction filter. The term $H(q_x, q_y; z) = \Omega(q_x, q_z; z)e^{i\varphi(q_x, q_y; z)}$ is a complex filter comprising an amplitude factor $\Omega(q_x, q_z; z)$ and a phase factor $e^{i\varphi(q_x, q_y; z)}$. Phase factor for defocus correction is explicit in Eq.(2.27) as $e^{iz_d\mathbf{q}^2/4k_c}$ but the idea of CAO is to adaptively defined the phase factor based on the data rather than using the analytical expression [35], which only accounts for defocus and requires precise knowledge of physical quantities of the system, for instance, the location of the focal plane in the tomogram. The procedure to obtain an aberration-corrected sample scattering potential using Eq.(2.29) is rather simple —note that it is a spatial deconvolution performed in Fourier domain— the key point is to determine the appropriate correction filter. In CAO, the amplitude factor $\Omega(q_x, q_z; z)$ is usually set to unity, because it does not produce a significant impact in image distortions, and a phase-only filter $H(q_x, q_y) = e^{-i\tilde{\varphi}(q_x, q_y; z)}$ is used, where the approximate phase $\tilde{\varphi}(q_x, q_y; z)$ is described

in terms of a polynomial basis, such as Zernike polynomials Z_i which are a convention for the description of optical aberrations [84, 142]. Using a weighted sum with N Zernike polynomials, $\tilde{\varphi}(q_x, q_y; z)$ is expressed as

$$\tilde{\varphi}(q_x, q_y; z) = \sum_{i}^{N} Z_i \alpha_i(z_d), \tag{2.30}$$

with weights $\alpha_i(z)$ that vary with depth. To determine $\alpha_i(z)$, there are two general approaches, optimization-based CAO [35] and sub-apertures correlation CAO [69].

Sub-apertures correlation method proposed by Kumar *et al.* consists in measuring the local slope of the wavefront in the pupil/Fourier plane to determine the correction phase, emulating a Shack-Hartmann sensor [69]. The Fourier transform of the acquired signal for each depth, namely $\hat{S}(q_x, q_y; z)$, is split into sub-apertures and the inverse Fourier transform of each sub-aperture is computed to yield images that will exhibit lower resolution and relative shifts between them. These images are cross-correlated to the image of a reference sub-aperture to measure the relative shifts, that is related to the local slope of the wavefront. Then, the local slopes are used to construct the phase correction, possibly using a decomposition like Eq.(2.30). The number of sub-apertures determines the degree of aberrations that can be corrected. For instance, splitting the pupil into two vertical and horizontal apertures enables defocus correction along the two scan axis. A large number of sub-apertures is desired to be able to correct for high-order aberrations, however, this leads to a significant resolution loss and an increased image correlation error, which ultimately results in high errors in the determination of the correction phase.

Optimization-based CAO proposed by Addie *et al.* [35] consists in finding the set of weights $\alpha_i(z_d)$ that improves image quality as measured by a metric via optimization. The iterative operation of this procedure may increase computational time compared to sub-aperture based CAO, but it allows to straightforwardly include high-order aberrations by increasing the number of polynomials and weights used in the correction phase composition. Optimization-based CAO relies on the definition of a proper image quality metric, that ideally must have a minimum (or a maximum) when image aberrations are well compensated. Most used metrics measure image sharpness since aberrations correction is supposed to improve sharpness.

For the following definition of image sharpness metrics, and in subsequent models presented in this work, discrete indexes (m, n, l) are used as discrete counterparts of continuous coordinates (x, y, z), respectively. For instance, $S(m, n, l)$ —sometimes written as $S_{m,n,l}$ for simplicity— is the discrete counterpart of the ideally continuous signal $S(x, y, z)$. In general, mathematical models will be described in continuous notation, and discrete notation will be used exclusively in intrinsically discrete

equations.

Shannon's entropy metric $\mathrm{SE}(I)$ of an image $I_{m,n}$ with discrete indexes (m,n) and size $M \times N$ is known to be minimal when aberrations are minimized, it has been used in the context of CAO in OCT [61], brought from SAR imaging [143], and is given by

$$\mathrm{SE}(I) = \sum_{i}^{M} \sum_{j}^{N} \Gamma(\bar{I}_{i,j}), \tag{2.31}$$

where $\Gamma(I) = -I \log I$, although different transformations can be used, and

$$\bar{I} = \left| \frac{I}{\sum_{i}^{M} \sum_{j}^{N} |I_{i,j}|} \right|^2 \tag{2.32}$$

is a normalized intensity image. Here, $I_{m.n} = S_{m,n,l}$ is the current l-th *en face* plane being compensated [recall that $S_{m,n,l}$ refers to the discrete version of $S(x,y,z)$].

There are several image quality metrics that have been used in the context of other imaging modalities such as digital holography [144]. For instance, Tamura's coefficient $T = \sqrt{\frac{\sigma(I)}{\langle I \rangle}}$ is a measure of contrast [145], where $\sigma(\cdot)$ is the standard deviation and $\langle \cdot \rangle$ is the average value, and gradient-based metrics such as

$$\mathrm{G(I)} = \sum_{i}^{M} \sum_{j}^{N} \sqrt{\left[I_{i,j} - I_{i-1,j}\right]^2 + \left[I_{i,j} - I_{i,j-1}\right]^2}, \tag{2.33}$$

where $I_{m,n} = |S_{m,n,l}|^2$. Image spatial frequency content metrics have been used in sensorless hardware AO and eventually in CAO [146], and are based on the fact that mid- to high-frequency content of the complex amplitude should increase as resolution improves, i.e. when aberrations are minimized. One possible estimation is the ratio of energy within a band-pass frequency range to the total energy [35], expressed as

$$\mathrm{F}(I) = \frac{\sum_{i}^{M} \sum_{j}^{N} |I_{i,j} B_{i,j}|^2}{\sum_{i}^{M} \sum_{j}^{N} |I_{i,j}|^2}, \tag{2.34}$$

where $I_{m,n} = \hat{S}_{q_m,q_n,l}$, being (q_m, q_n) discrete counterparts of (q_x, q_y), and $B_{m,n}$ is a band-pass filter with cut-off frequencies tuned to obtain a good performance.

Figure 2.12 illustrates the effect of aberrations in a simulated *en face* OCT image (xy plane) that was generated elsewhere [60] with a probe beam waist diameter of 10 μm. The tomogram consists of a large number of point scatterers distributed in the entire field of view as occurs in tissues, with a similar index of refraction, producing speckle. Also, point scatterers with a different index of refraction were

added and arranged in a cylindrical geometry along horizontal axis x, appearing as bright rectangles in the cross-sectional *en face* view of Fig.2.12(a) located at the focal plane. Eq.(2.26) was used to induce defocus as if the *en face* plane of Fig.2.12(a) were located at $z = 200$ μm from the focal plane, and defining the phase of H shown in Fig.2.12(e), using Zernike polynomials Z_5 and Z_7 to induced astigmatism and coma aberrations with random magnitudes, resulting in the aberrated *en face* of Fig.2.12(b), where blurring is evident and consequently resolution loss.

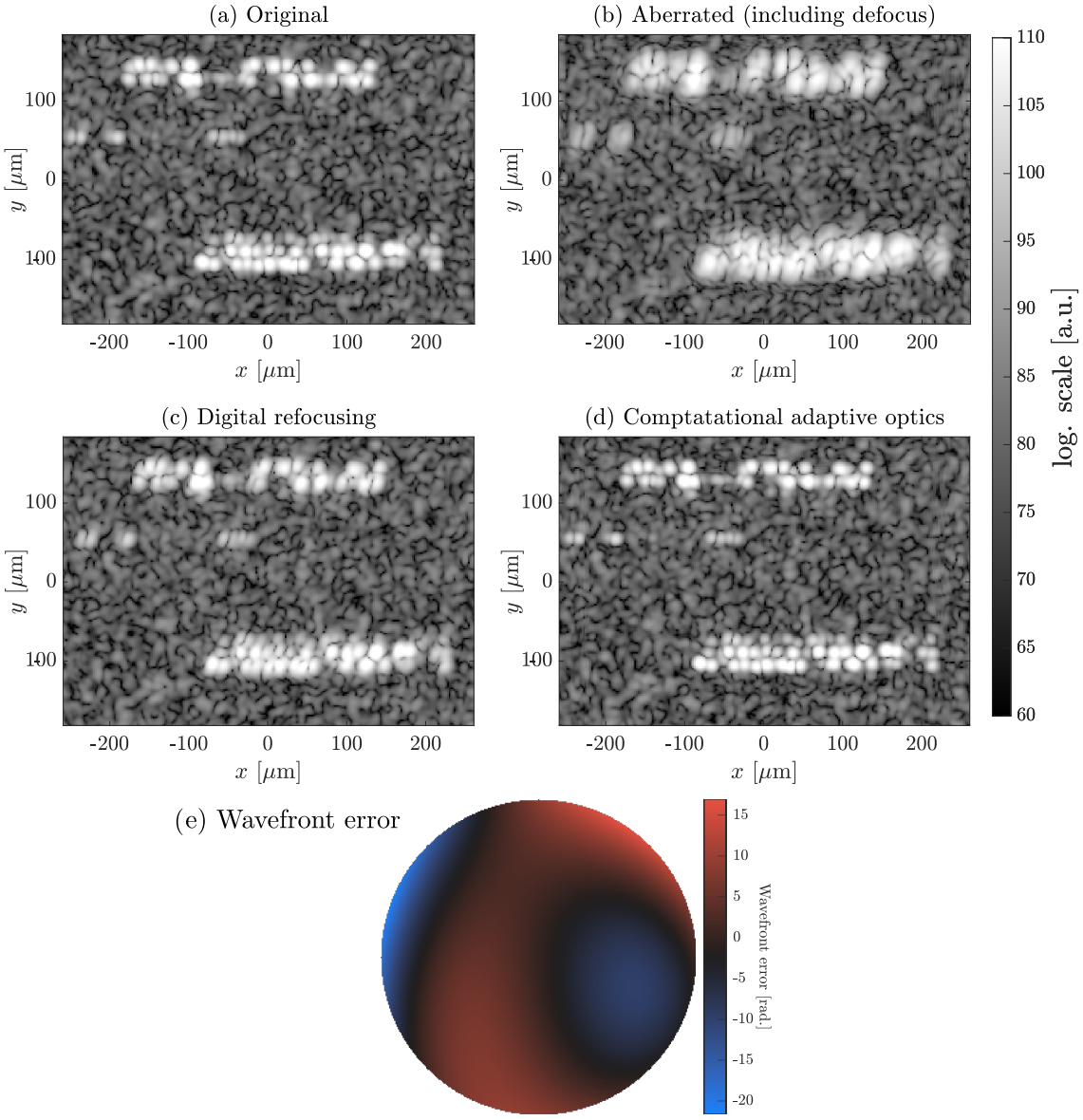

Figure 2.12: Illustration of computational adaptive optics. Simulated OCT *en face* image (a) without and (b) with aberrations and defocus, induced using the wavefront in (e). Result of (c) digital refocusing and (d) computational adaptive optics. (a)–(d) are displayed in logarithm scale.

Digital refocusing was applied to the aberrated *en face* using Eq.(2.27) setting

$H = 1$, resulting in a refocused image with partial resolution improvement only, due to the presence of the remaining two aberrations deteriorating image quality. On the other hand, optimization-based CAO was applied to the aberrated *en face* using Eq.(2.29), by describing the phase correction filter with Z_4, Z_5 and Z_7, being Z_4 Zernike polynomial for defocus. Aberration-corrected *en face* view of Fig.2.12(d) exhibits focal resolution similar to the original *en face*, demonstrating the possibility of correcting defocus and additional aberrations using CAO.

To illustrate the behavior of image quality metric that is the basis of CAO, original *en face* of Fig.2.12(a) was defocused using Z_4 weighted by $\alpha_4 = 17.8$ and then several corrected images were created with weights linearly varying between $[-40, 20]$. Figure 2.13 shows a plot of Shannon's entropy of the corrected image as a function of the correction weight $\tilde{\alpha}_4$, exhibiting a smooth behavior with a clear minimum at nearly $\tilde{\alpha}_4 = -17.8$, where the negative sign is because the correction phase term is the conjugate of the actual defocus term. Alongside Shannon's entropy, there are six examples *en faces* with different phase corrections, with the optimal *en face* enclosed in a red box, showing the best image quality among them.

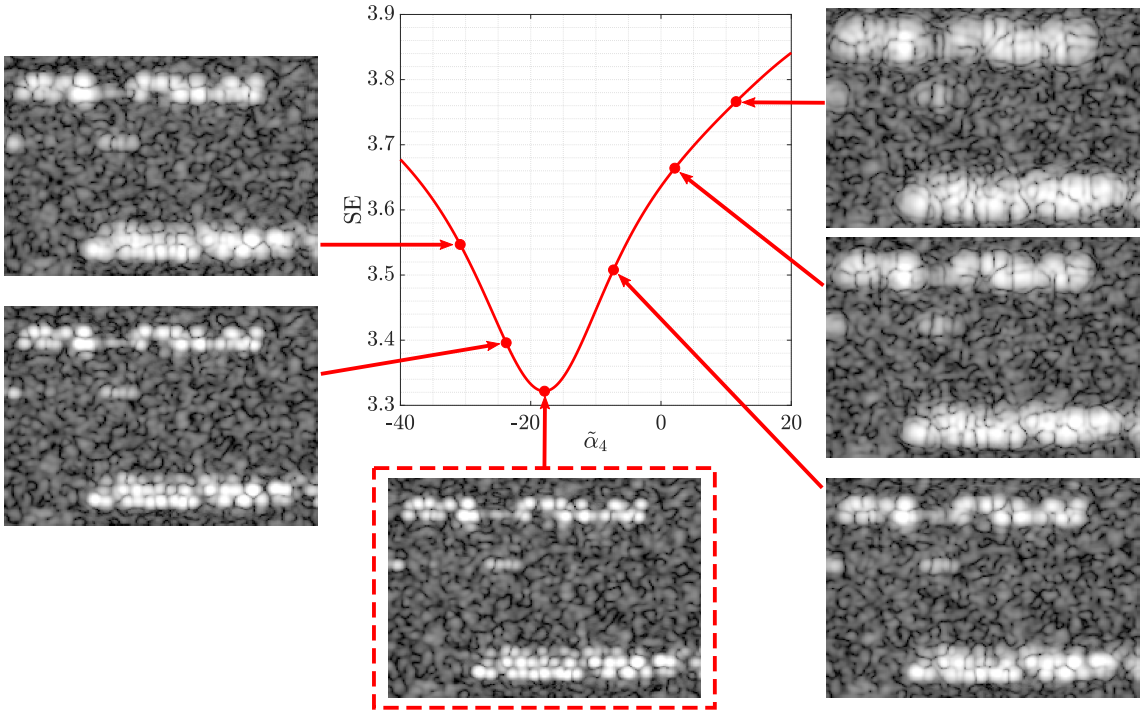

Figure 2.13: Illustration of Shannon's entropy metric to measure image sharpness of a defocused *en face* image corrected using Zernike polynomial Z_4. Plot shows the value of SE as a function of correction weight $\tilde{\alpha}_4$. Surrounding *en faces* images were corrected with different weights for a visual inspection of image quality. Optimal corrected image (on the red rectangle) corresponds to the minimum value of SE.

Computational adaptive optics promises to be a powerful alternative to hardware-based adaptive optics which requires very complex optical setups, specially in retinal

imaging where the demand of cellular imaging increases, for example in photoreceptors mosaic imaging [61, 62, 147].

There are two necessary requirements for computational aberration correction: acquired tomogram should possess phase stability which is so far the major requirement [47, 120, 133], but in addition, the lateral sampling must satisfy Nyquist sampling [120], i.e. lateral sampling must be equal or smaller than half the beam waist diameter, otherwise high-frequency content is not recovered properly and results will present distortions. In fact, Nyquist sampling is necessary in general for computational refocusing in any imaging technique, not only in OCT [148–150].

2.3.4. Phase stability requirement

Computational techniques described previously rely upon accurate measurements of the complex amplitude information to guarantee a coherent aperture synthesis, necessary for aberration correction. Complex amplitude comprises amplitude and phase information, but the phase is more susceptible to undesired fluctuations [63], hence reliable phase measurement is not a straightforward task due to experimental constrains as explained in Section 2.1.6. Early digital refocusing approaches in OCT were based on the intensity [115, 135, 151], but they provided very limited results given that incoherent deconvolution ignores the phase information. Such initial approaches were designed to work with the intensity signal possibly because of the lack of phase-stable measurements in early OCT systems.

This section aims to discuss the phase stability requirement in the context of computational aberration correction. Phase stability is affected by phase noise that may arise from the system or the sample. System-induced phase noises, such as phase-jitter [63] and galvanometer-induced phase noise [67, 117], were explained in Section 2.1.6. On the other hand, sample-induced phase noise arises from sample motion [64], therefore it affects mainly *in vivo* imaging which is more prone to motion during signal acquisition than *ex vivo* imaging. Motion can be either global, such as the involuntary movement of the subject, or internal, such as blood flow in arteries.

The development of computational aberration correction has been grounded in SDOCT systems. For this reason, most significant phase instabilities induced by the system arise from the galvanometer scanners, which can be experimentally avoided in some cases, therefore, in this area, major attention has been put on sample motion-induced phase noise, which is the focus of the following discussions.

Sample motion has two primary effects in the complex OCT signal; effective shift of the complex amplitude and phase-only jump [47, 66, 67]. The former effect is rather intuitive, it is the displacement of the apparent location of the signal in the tomogram, affecting both amplitude and phase. The latter effect is an additional

phase-only jump that is a consequence of the Doppler effect, and actually, it is used for functional imaging techniques such as flowmetry [152]. Both effects have an impact in the phase of the tomogram and therefore they affect phase stability, but their individual influence varies depending on system parameters [47]. Effective complex amplitude shift scales with the spatial resolution of the system; a system with fine resolution may be more susceptible to motion artifacts. In general, axial resolution is finer than lateral resolution, therefore this effect has a greater impact in the axial direction. On the other hand, phase-only jump δ is a consequence of motion in the axial direction only, and is proportional to the axial displacement δz and the central wavenumber, $\delta = 2k_c\delta z$, where the factor of two is due to the double-pass, reflection geometry. Since k is typically a relatively large value (of the order of 10^6) relatively small displacements δz can produce significant phase jumps δ, and this is the reason for optical phase-sensitive techniques being able to measure very small displacement using optical interferometry. However, in the case of CAC, the Doppler phase is an undesired phase contribution that in general has a greater influence than the complex amplitude shift effect. For this reason, in some cases, there is not an evident displacement in the tomogram intensity due to motion, yet there may be phase jumps reducing phase stability.

In practical terms, motion artifacts are negligible during one A-line acquisition under controlled circumstances, in the case of SDOCT because of the parallel acquisition in k-space, and in SSOCT because of the high A-line acquisition rate. However, motion artifacts may appear during the acquisition of multiple A-lines and more significantly during the acquisition of multiple B-scans which have a longer repetition time. Complex amplitude shifts appear as relative displacements between A-lines or B-scans, whereas phase-only jumps produce a relative phase offset between A-lines or B-scans. For these reasons, hereafter 1D and 2D phase stability are used to refer to phase stability along one or two lateral scan axes, obviating phase stability along the axial direction as it is often ensured.

Figure 2.14 illustrates motion artifacts in OCT, using a simulated B-scan generated similarly to that of Fig.2.11, but with axial motion added when computing the n-th A-line by changing the position z of all scatters by $z + \delta z_n$, where δz_n represents the magnitude of motion, with random values defined for each A-line, inside a predefined range. This corresponds to a rigid body or *bulk* motion because the entire sample is displaced by the same amount in every A-line. The simulated intensity B-scan with a static sample is shown in Fig.2.14(a), displaying defocus away from the focal plane located at $z = 0$. This image was re-generated inducing inter-A-line motion randomly distributed with standard deviation 1 μm, shown in Fig.2.14(d), and the resulting intensity B-scan showed in Fig.2.14(b) exhibits spurious relative shifts between A-lines, which in this case are evident because the magnitude of motion is of the order of axial resolution 5 μm.

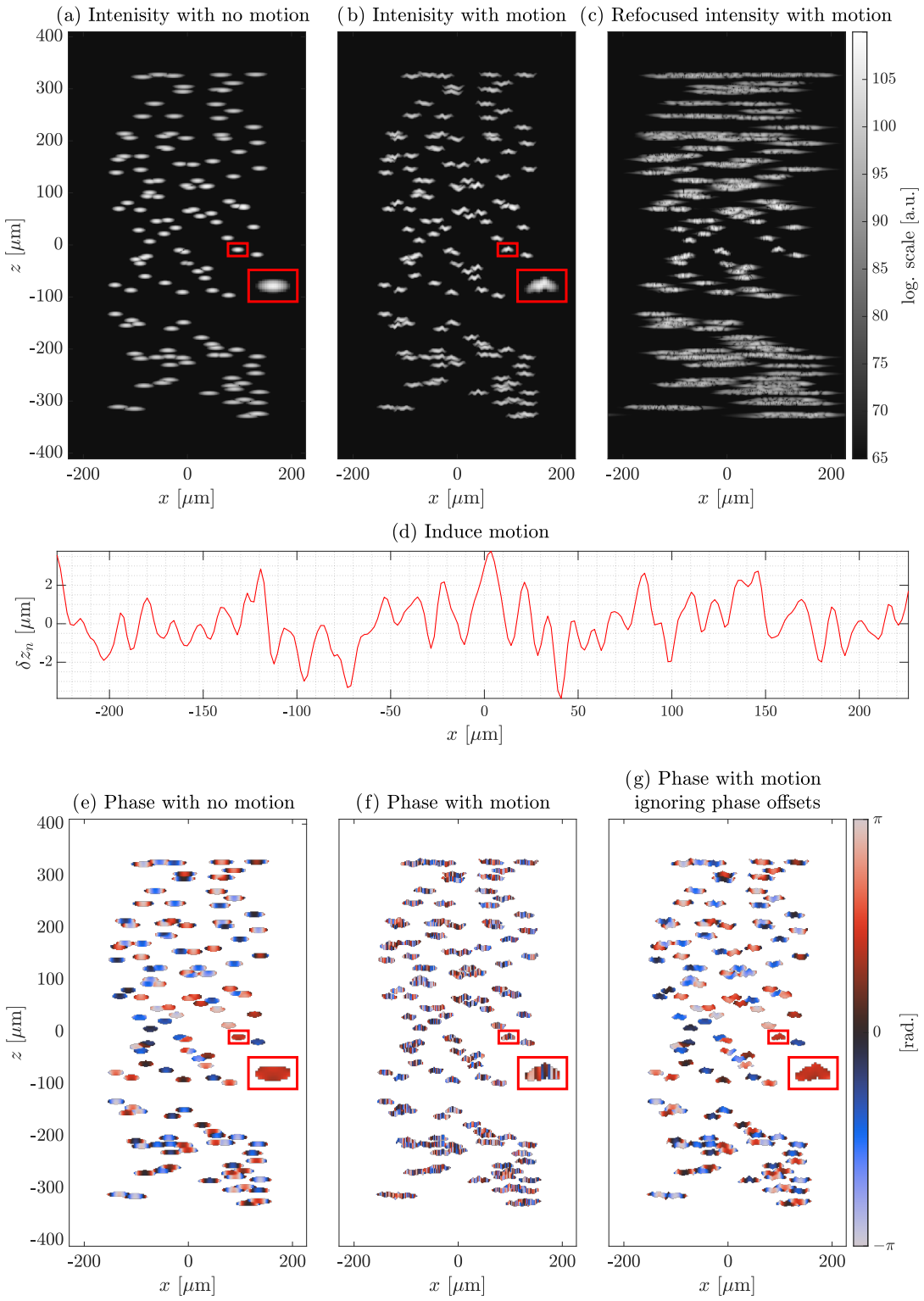

Figure 2.14: Illustration of the impact of motion in phase stability and digital refocusing. OCT image simulated using the forward model, (a) with the static sample; (b) with sample motion shown in (d), that results in the unsuccessful digital refocused image in (c). Note the relative shift between A-lines when comparing the insets in red rectangles. Phase images: (e) with the static sample; (f) with sample motion shown in (g) and the same of (f) but ignoring the Doppler phase jumps.

To evaluate phase stability, Fig.2.14 shows phase images computed as the argument $\arg\{S_{m,n,l}\}$ of the simulated data $S_{m,n,l}$, where a threshold was used to display only regions with high intensity, corresponding to the point scatterers. Fig.2.14(e) is the phase with the static sample, exhibiting a stochastic but smooth behavior, distinctive of phase-stable images. The phase image after inducing motion shown in Fig.2.14(e) exhibits very poor phase stability because of the relative shifts between A-lines, also observable in the intensity image in Fig.2.14(b), and more importantly due to the random phase offsets induced by Doppler jumps, not observable in the intensity image in Fig.2.14(b). Lack of phase stability frustrates the operation of digital refocusing or any other phase-dependent aberration correction method, as is evident in Fig.2.14(c). To compare the influence of the two effects of motion, Fig.2.14(f) shows the phase when ignoring the motion-induced phase offsets, thus considering only the complex amplitude shifts, and it can be noted that phase is smoother than that of Fig.2.14(g) affected by both motion artifacts, however, even ignoring phase jumps, complex amplitude shifts alone are strong enough to frustrate any aberration correction in this particular example.

To quantitatively determine that a given tomogram has sufficient phase stability for a phase-dependent technique to work properly is somehow not possible (unless attempting CAC and then visualizing if results are corrupted or not), instead, it is possible to recognize when phase stability is not enough for such techniques to provide reliable results. Some systematic studies have been carried out to show the effect of various types of motion on defocus correction, namely, 1-D Brownian motion, steps functions, and sinusoidal motion. They helped to determined thresholds for admissible motion magnitudes for successful aberration correction to assist the design of OCT systems, for instance, to determine an adequate imaging speed. Such works include simulated studies, as well as experimental studies with *ex vivo* sample [47], and a further extension with *in vivo* imaging [64], finding out that in terms of motion-induce phase noise, axial motion influences the most to phase stability, although in some experimental scenarios traverse motion may be significant as well.

It is important to recall that phase stability is more difficult to achieve in SSOCT compared to SDOCT given that the former is susceptible to phase-jitter describing a linear depth-dependent noise, in addition to the phase noise sources affecting in SDOCT.

2.3.5. Phase stabilization

Given that the presence of phase noise in acquired tomograms is quite difficult to avoid or suppress experimentally [117], phase stabilization in post-processing has been developed for phase-dependent imaging techniques in OCT like aberration correction and Doppler OCT. Phase stabilization techniques were designed to correct

for phase jumps between A-lines, whether they arise from sample-motion or the system itself, but they cannot address complex amplitude shifts, hence those must be negligible. In this section, numerical phase stabilization approaches are presented oriented to the correction of phase offsets. Correction of phase offsets is not sufficient for phase-jitter correction which is a linear depth-dependent phase noise, however, the methods presented here can be extended to address phase-jitter with slight modification, and the core discussions of this section applies equally for this type of phase noise.

An early phase stabilization approach employs a reference signal consisting in an highly reflective flat surface in the sample arm, like a mirror or even a coverslip [71,153]. The phase of this reference signal is assumed to be space-invariant, thereby any phase jump between A-lines must be due to phase noise. The procedure consist in identifying and extracting the reference signal in the tomogram $S(m, n, l)$, which should appear across the entire lateral field of view but typically occupy only a small set of pixels L in the axial direction. In a phase-stable tomogram reference signal should have a constant phase value. Then, the phase difference between adjacent A-lines m and $m-1$ are computed as

$$\delta(m, n) = \arg\left\{\sum_{l \in L} S(m, n, l) S^*(m-1, n, l)\right\}, \tag{2.35}$$

where * denotes complex conjugate and the summation over L is to average the phase of phasors along depth only in the pixels occupied by the reference reflector. Phase differences $\delta(m, n)$ are relative to consecutive A-lines. The absolute phase differences $\Delta(m, n)$ with respect to a reference A-line, typically the first A-line, are calculated using a cumulative sum as

$$\Delta(m, n) = \sum_{\hat{m}=1}^{m} \delta(\hat{m}, n). \tag{2.36}$$

Finally, the phase-corrected tomogram $\tilde{S}(m, n, l)$ is computed applying the conjugate phase differences,

$$\tilde{S}(m, n, l) = S(m, n, l) e^{-i\Delta(m,n)}. \tag{2.37}$$

To summarize, this phase stabilization process, refer to as *hardware-based* stabilization, consists of applying a conjugate phase offset that is determined for each A-line using the phase difference between consecutive A-lines considering only a

region of the signal containing a constant phase reference. There are some important features to remark. First, the correction phase is depth-independent; it consists of a global phase offset for every A-line, hence it cannot correct for phase-jitter which is a depth-dependent ramp phase noise as noted in Eq.(2.9). An extension to cover phase-jitter is possible and has been developed [63] as will be explained later. Second, a reflective surface in the sample arm is difficult to implement in practical terms, especially for *in vivo* imaging where it is not easy to add a reflective surface in the sample arm directly. A very used approach is to separate the sample arm into two paths, one for the sample and the other for a mirror, but this is based on hardware modifications not present in basic OCT setups.

The hardware-based phase stabilization approach was crucial for the development of CAC techniques like ISAM in an early stage [71]. However, this is an unpractical approach because it relies on a hardware modification of the system. A fully numerical approach was developed in the context of Doppler OCT [67], then its use migrated to the field of CAC and is currently in the use [65]. Fully numerical approaches rely on the use of the signal information itself to determine the relative phase offset between A-lines by using Eq.(2.35), except that the entire axial scan $S(m, n, l)$ is employed to compute the phase differences, instead of using the signal from a reference reflector.

The operation of this method relies on speckle correlation: in phase-stable tomograms, the phase difference between consecutive A-lines must approximate to zero if speckle is fully correlated, thus any phase fluctuation is due to phase noise [67]. Correct speckle sampling is necessary because, otherwise, phase difference would be due to phase noise but also due to speckle decorrelation, yielding an erroneous phase correction. A correct sampling of speckle is obtained when Nyquist sampling theorem is fulfilled, actually, this requirement is already imposed by CAC techniques. This method provides sufficient phase stability for phase-dependent techniques like CAC, but it suffers from some imperfections and thus results are limited.

More specifically, because tissue is not homogeneous as is the case of a reference reflector, there are phase differences associated with changes of the tissue. These differences are insignificant at local level, i.e. in the computation of relative phase differences $\delta(m, n)$, but become significant in the accumulation used to compute the absolute phase differences $\Delta(m, n)$ in Eq.(2.36). Imperfection also arises when there are noisy A-lines or with no signal at all where phase correction may fail, producing errors that propagate in the cumulative sum, denoted here as *long-range* errors. In other words, this method yields *local* phase stability but the propagation of errors due to the cumulative sum results in long-range errors that frustrate obtaining *global* phase stability. However, this is not a limitation for CAC techniques, because it is known that local phase stability is sufficient to perform the deconvolution operation that is the basis of CAC [47]. The deconvolution kernel in practical scenarios has a

relatively small size thus only local information from a small neighborhood of A-lines is merged in the deconvolution, which means that it is sufficient to have local phase stability, at the scale of the deconvolution kernel size.

It is important to remark that phase values that can be corrected are arbitrary despite phase wrapping may appear. Suppose a certain A-line S_A is experimentally phase-shifted by $2\pi r$ with $r \in \mathbb{R}$, resulting in $\tilde{S}_A = S_A e^{i2\pi r}$. Phase shift $2\pi r$ can be decomposed as $2\pi r = \Delta + 2\pi n$ with $n \in \mathbb{Z}$ and the effective computed phase shift Δ being in the range $[-\pi, \pi]$. Therefore, shifted A-line is $\tilde{S}_A = S_A e^{i\Delta} e^{i2\pi n} = S_A e^{i\Delta}$, showing that a phase correction in the range $[-\pi, \pi]$ is sufficient and the n additional cycles of 2π are inconsequential given that $\tilde{S}_A = \tilde{S}_A e^{i2\pi n}$. In fact, this discussion in valid in the context of computational aberration correction where the requirement is to maintain a constant phase relation between measurements [47]. However, in certain applications quantification of phase shifts is necessary thus in such cases phase wrapping must be properly addressed, for instance, for the proper quantification of flow velocity in Doppler OCT [101].

Examples of phase stabilization are shown in Fig. 2.15 for an OCT B-scan simulated using the forward model for a low-NA system as in previous examples. In this case, there are 10000 point scatterers with random positions and equal index of refraction to produce speckle and 128 points with random positions and random index of refraction producing higher intensity than the background scatterers, as can be noted in the intensity image in Fig. 2.15(a). Bulk sample motion randomly distributed with standard deviation 0.1 μm was added. Such motion does not induce noticeable complex amplitude shifts as can be seen in Fig. 2.15(a), but phase offsets are strong as shown in the phase image of Fig. 2.15(b) which presents strong fluctuations that greatly reduce phase stability.

Apart from the sample, a flat reflector marked by the green arrow in Fig. 2.15(a) was added to the top of the image covering the whole fast scan axis but with a small thickness of $L = 10$ μm. Note that the phase of the reference reflector in Fig. 2.15(b) appears constant across depth because no motion artifacts affect this direction, but it fluctuates randomly across the transverse axis due to sample-induce phase noise. This reference reflector was used to perform hardware-based phase stabilization by computing the phase differences only for pixels corresponding to the reference reflector, and the resultant corrected phase, shown in Fig. 2.15(c), exhibits a random but smooth behavior distinctive of correlated speckle, and the phase of the reference reflector is now constant as expected in a phase-stable system.

The original unstable phase was also corrected using fully numerical stabilization, employing only the signal information in the calculation of the phase differences and ignoring the pixels occupied by the reference reflector. The resultant corrected phase is shown in Fig. 2.15(d) and it seems fairly similar to that corrected using the

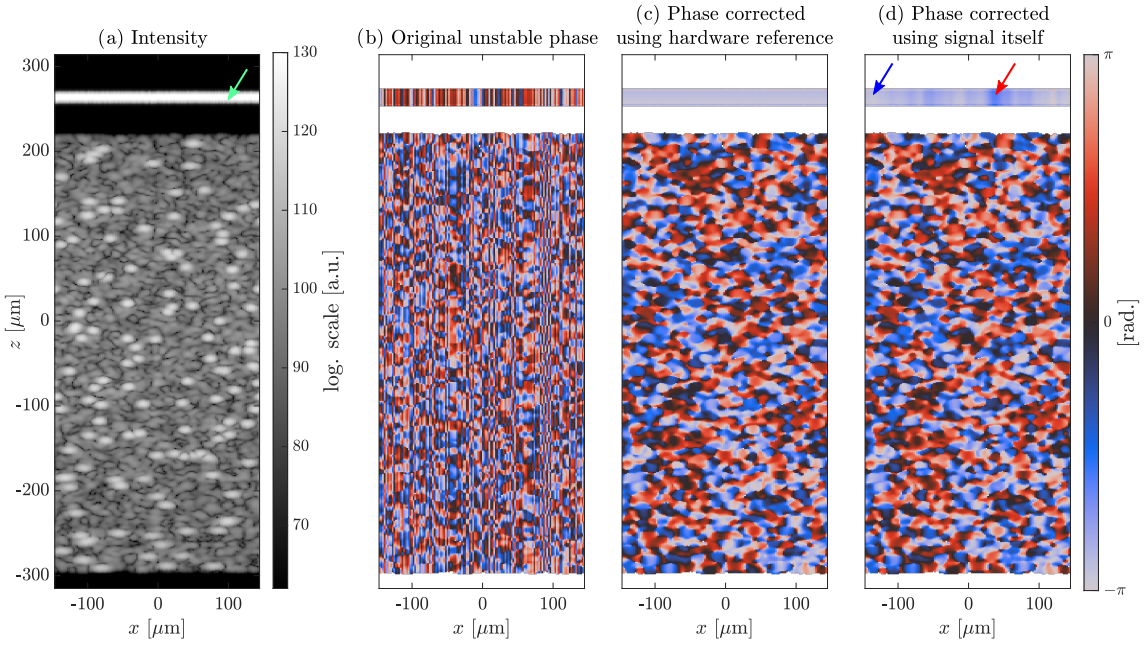

Figure 2.15: Illustration of phase stabilization. OCT image simulated using the forward model: (a) intensity and (b) phase presenting phase instabilities due to sample-induced phase noise. Corrected phase using (c) hardware-based stabilization and (d) fully numerical stabilization, based on tissue signal alone.

reference signal, showing that indeed phase correction is possible using the sample signal alone, with no need for reference reflections. Imperfections of the method can be visualized in the phase of the reference reflector in Fig. 2.15(d): at local scale, the phase is correlated as observed in the individual regions marked by arrows blue and red, but at global scale the phase is uncorrelated as noted when comparing the phase in these two regions, which in principle should have the same value.

In the previous models, phase differences for phase stabilization were calculated along fast scan axis x but the same procedure can be applied along the slow scan axis y. Since its operation is intrinsically 1D, fully numerical phase stabilization yields successful results only along a single axis at a time, and its imperfections hinder any 2D correction. It means that in the presence of 2D phase instabilities in xy, only one axis can be stabilized; the one along which phase differences are calculated. Furthermore, performing two successive corrections along each axis once at a time, e.g. correcting x axis first and then y axis, is not successful either, as will be demonstrated later, because the global errors induced in the first correction makes it impossible to correct along the second axis without destroying the phase stability in the first axis.

Apart from using a hardware reference signal which relies on physical modifications, there is not any fully numerical phase stabilization method capable of correcting phase noise in two dimensions. This limitation has been overcome using systems

that provide at least phase stability along one scan axis [34, 65, 68, 105, 154–156], in some cases even phase stability along the two scan axis is obtainable and therefore phase stabilization is unnecessary [61, 69, 70, 157, 158]. In particular, CAC techniques have been used mostly in SDOCT systems that have the potential to provide 1D, or even 2D phase stability using fast line-field systems. In raster scan SDOCT systems, scanning speed along the fast scan axis is fast enough to neglect motion artifacts in that direction, and phase offsets are only significant along the slow scan axis, this, in combination with numerical stabilization is sufficient for the operation of CAC techniques [65].

Numerical phase correction of phase-jitter noise is straightforward with extensions of the aforementioned phase stabilization methods, but they still provide 1D phase stability, and no 2D phase correction is yet known. Because SSOCT is intrinsically 2D phase-unstable in the presence of phase-jitter, CAC techniques in such systems have relied on hardware solutions. For instance, full-field systems have been used since they provide intrinsic 2D phase stability given the parallel acquisition of the entire transverse plane [61, 69], and more recently, operation in raster scan systems has been possible using k-clocked systems and a small FoV [62]. These solutions are considerably unpractical since they require major hardware components that are not present in most OCT systems. For instance, k-clocks require an additional interferometer and a compatible digitizer that not only increase cost but also the complexity of the systems.

Computational aberration correction is a powerful tool in many scenarios but it has been very restricted by the phase stability requirement; it is not possible to carry out any CAC technique in many raster scan OCT systems. There is therefore a great interest in developing fully numerical strategies to perform CAC techniques in 2D phase-unstable system.

In the following chapter, a technique for CAO in 2D phase-unstable systems developed in this work is described and successful experimental demonstrations are presented.

CHAPTER 3

COMPUTATIONAL ABERRATION CORRECTION IN PHASE-UNSTABLE OCT: SHARP

There are several techniques for computational aberration correction in OCT as presented in the previous chapter, all relying on a phase stability requirement to successfully operate the complex OCT signal. The core proposal of this work is described in detail in this chapter, a technique called SHARP to carry out CAO in tomograms having two-dimensional phase noise, and capable of correcting x-y-separable aberrations in tomograms affected by phase-jitter noise, which typically appears as 2D phase noise

The foundations of the method are presented in Section 3.1, starting with the description of a tool for the assessment of phase stability and the validation of Nyquist sampling, following with an illustration of attempts to 2D phase stabilization, to show the impossibility to succeed with current fully numerical correction, and to explain the motivation behind the operation of SHARP. By the end of the section, the steps of the method are described and explained in detail. Then, results from a proof of concept experiment are presented in Section 3.2, to evaluate the performance of SHARP in an experimental dataset and determine if its purpose is well accomplished. Finally, complementary steps for SHARP are explained in Section 3.3, oriented to solve specific issues not covered by the general proposal, to increase its applicability and improve results in particular situations. In particular, a strategy to perform SHARP in polarization-sensitive OCT is explained after briefly introducing the operation of Stokes PS-OCT processing. Finally, a non-local means denoising technique, called CTNode, for complex noise reduction in OCT is described and evaluated with simulated OCT data with synthetic noise.

3.1. SHARP: A CAO technique for OCT

3.1.1. Phase stability and sampling assessment

Phase stability of a system can be estimated by imaging an reflective surface and computing the phase difference between consecutive A-lines. However, this is not useful in practical situations to estimate phase stability in tomograms of real samples unless there is a reference reflector. Here, a tool for qualitative assessing phase stability and sampling in any complex tomogram is presented, based on the sample signal information itself and its acquisition process, based on a previous work [60].

Consider the lateral Fourier transform of the acquired signal $\hat{S}(x, y; z_d)$ for the low-NA regime in Eq. (2.29), which can be written as

$$\hat{S}(q_x, q_y; z_d) = H(q_x, q_y, z_d)\hat{\eta}(q_x, q_y, z_d), \tag{3.1}$$

where the phase term in Eq. (2.29) is included in the filter H, which can be described as $H(q_x, q_y, z_d) = \Omega(q_x, q_y, z_d)e^{i\varphi}$, being Ω its amplitude and $\varphi(q_x, q_y; z_d)$ its phase. Although the phase of H varies with depth, its amplitude can be approximated to be constant over depth, and it follows a Gaussian distribution in the case that the input collimated beam in the scan lens of the system is also Gaussian-distributed (as it is in standard systems). The latter can be noted in the amplitude term $e^{-\mathbf{q}^2\alpha^2/4k^2}$ of the forward model in Eq. (2.18). The power spectrum $\xi = |\hat{S}|^2$ of the signal is

$$\begin{aligned}\xi(q_x, q_y, z_d) &= |H(q_x, q_y, z_d)\hat{\eta}(q_x, q_y, z_d)|^2 \\ &= |\Omega(q_x, q_y)|^2|\hat{\eta}(q_x, q_y, z_d)|^2.\end{aligned} \tag{3.2}$$

The power spectrum of the sample $|\hat{\eta}(q_x, q_y, z_d)|^2$ is in general unknown but it is known to be a random distribution, given the random scattering property that characterizes tissue. Therefore, the expected value over depth of $|\hat{\eta}(q_x, q_y, z_d)|^2$ will yield a flat, nearly constant power spectrum γ, thus the mean power spectrum (MPS) $\bar{\xi}$ of the acquired discrete signal, averaged over N_z depths planes, is given by

$$\begin{aligned}\bar{\xi}(q_m, q_n) &= \frac{1}{N_z}\sum_{l=1}^{N_z}|\mathrm{FT}_{m,n}\{S(m, n, l)\}|^2 \\ &\approx \frac{1}{N_z}|\Omega(q_m, q_n)|^2\sum_{l=1}^{N_z}|\hat{\eta}(q_m, q_n, l)|^2 \\ &\approx \frac{1}{N_z}\gamma|\Omega(q_m, q_n)|^2,\end{aligned} \tag{3.3}$$

where (q_m, q_n) are discrete indexes for (q_x, q_y), Because Ω follows a Gaussian distribution, then **the MPS $\bar{\xi}$ is also expected to follow a Gaussian distribution**. The latter is true assuming that there are not phase or amplitude disturbances on the signal $S(x, y, z)$, implying that the MPS is a potential tool to evaluate phase stability.

Phase noise affecting local phase stability manifests as high-frequency disturbances in the OCT signal, thus the Fourier transform of the signal will be distorted, presenting more high-frequency content than expected and therefore the MPS will no longer follow a Gaussian distribution. In other words, **the MPS of a tomogram with local phase stability follows a Gaussian distribution** whereas the MPS of a tomogram with local phase instabilities follows a non-Gaussian distribution, approaching a flat distribution. This "rule of thumb" on the analysis of the MPS is useful to determine whether a certain tomogram has enough phase stability for a successful operation of any CAC technique.

In the presence of global or long-range phase noise, the MPS will be only slightly affected given that such phase noise manifests as low-frequency content that is less significant than the low-frequency content of the Gaussian function. Such observation is important given that the numerical phase stabilization method described in Section 2.3.5 yields only local phase stability and not global, yet the analysis on the MPS is valid for such case.

To visualize the previous explanations, Figure 3.1 shows the MPS of the simulated tomogram used for Fig. 2.12 that is intrinsically phase-stable as shown in Fig. 3.1(a). Phase noise was added consisting of phase offsets randomly distributed across A-lines to illustrate the MPS of a phase-unstable tomogram, which has a nearly flat distribution, as observed in Fig. 3.1(b). Although the phase-stable MPS in Fig. 3.1(a) approximates to a Gaussian function, residual non-constant contributions of the sample frequency content appears when no sufficient depth planes N_z are available (in this case $N_z = 256$). However, this does not prevent the analysis of the MPS in practical terms because the Gaussian distribution dominates.

On the other hand, given the importance of correct sampling for the operation of CAC techniques, it is worth to discuss the impact of sampling on the MPS, as depicted in Fig. 3.1(c). The Gaussian shape of the MPS is related to the fact that the optical system acts as a low-pass filter with cutoff frequency f_c defined by the spatial resolution, thus the bandwidth of the Gaussian distribution is determined by the spatial resolution. The MPS will be truncated depending on the sampling, therefore changing sampling will not change the width of the Gaussian MPS, it will just truncate the Gaussian distribution depending on the sampling frequency. A *correct/incorrect* sampling of the tomogram results in a *sufficient/insufficient* frequency bandwidth of the Gaussian-shaped MPS, as explained below.

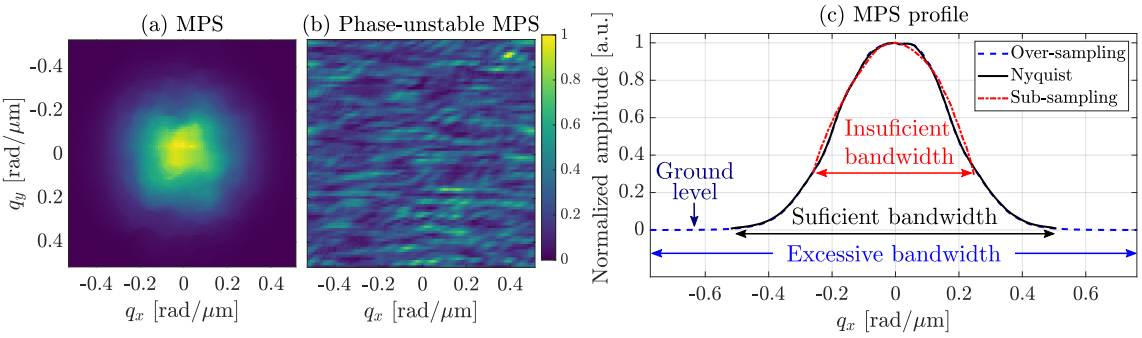

Figure 3.1: Illustration of the mean power spectrum with a simulated OCT tomogram. (a) MPS of the raw tomogram, (b) MPS of tomogram with induced phase noise, and (c) 1D profile of the MPS averaging along q_y, for the tomogram using different samplings

It is known that Nyquist frequency $f_N = 2f_{\max}$ provides the sufficient frequency bandwidth to correctly sample a signal with a known maximum frequency $f_{\max}$, which in this case is determined by the lateral resolution $f_{\max} = 1/\delta x$, thus $f_N = 2/\delta x$. In the case of having a correctly sampled tomogram (i.e. sampling less than $\delta x/2$), the frequency content will extend at least or beyond f_c, which means that the frequency bandwidth is *sufficient* to capture the Gaussian shape of the MPS, as occurs in blue and black curves in Fig. 3.1(c) which corresponds to the MPS of over-sampled and Nyquist-sampled tomograms, respectively. In the opposite case of having an incorrectly sampled tomogram (sampling greater than $\delta x/2$) the frequency content will be truncated before f_c, thus the frequency bandwidth is *insufficient* to capture the Gaussian shape of the MPS, as occurs with the red curve in Fig. 3.1(c) which corresponds to the MPS of a sub-sampled tomogram. Sub-sampled MPS does not reach the ground level, contrary to the other two cases. Therefore, **a tomogram with correct sampling will exhibit a MPS that captures the entire effective bandwidth of its Gaussian shape**. This means that the high-frequency content reaches the ground level, which is essentially zero but in practical terms will be an offset value corresponding to the noise floor level.

The two previous analyses on the MPS are useful tools to determine that certain tomogram satisfies the two main requirements for the successful operation of CAC techniques: phase stability and fulfillment of Nyquist theorem [72]. The MPS can be used to analyze the phase stability provided by the fully numerical phase stabilization method described in Section 2.3.5 that is of particular interest here. The simulated phase-unstable dataset used to exemplify the MPS in Fig. 3.1 was corrected using the phase differences of A-lines along x to compute the phase-jumps correction. Figure 3.2 shows *en face* phase images of the original tomogram, which is intrinsically phase-stable [Fig. 3.2(a)], of the tomogram with induced random phase-jumps, that is 2D phase-unstable [Fig. 3.2(b)], and after correcting phase-jumps along x axis,

resulting in phase stability only along that axis [Fig. 3.2(c)]. The original tomogram is 2D phase-stable as indicated by the 2D Gaussian shape of its MPS shown in Fig. 3.2(d), whereas phase-corrupted tomogram exhibits a nearly flat MPS in the two axes as shown in Fig. 3.2(e). Instead, the phase-corrected tomogram exhibits 1D phase stability, and this yields a MPS with Gaussian shape only along one axis, in this case, the x axis, whereas the orthogonal dimension remains phase-unstable and thus with a flat MPS as depicted in Fig. 3.2(f). To verify that certainly 1D phase stability is achieved after correction, the 1D profile of the MPS in the x axis can be computed by averaging along the q_y axis. This is shown in Fig. 3.2(e), where the 1D MPS of the original and phase-corrected tomograms approximate to a similar Gaussian shape, but corrupted tomogram has a constant MPS. Equivalent results are obtained if phase correction is computed using phase differences of A-lines along the y axis instead of x axis, except that now the only phase-stable axis will be y.

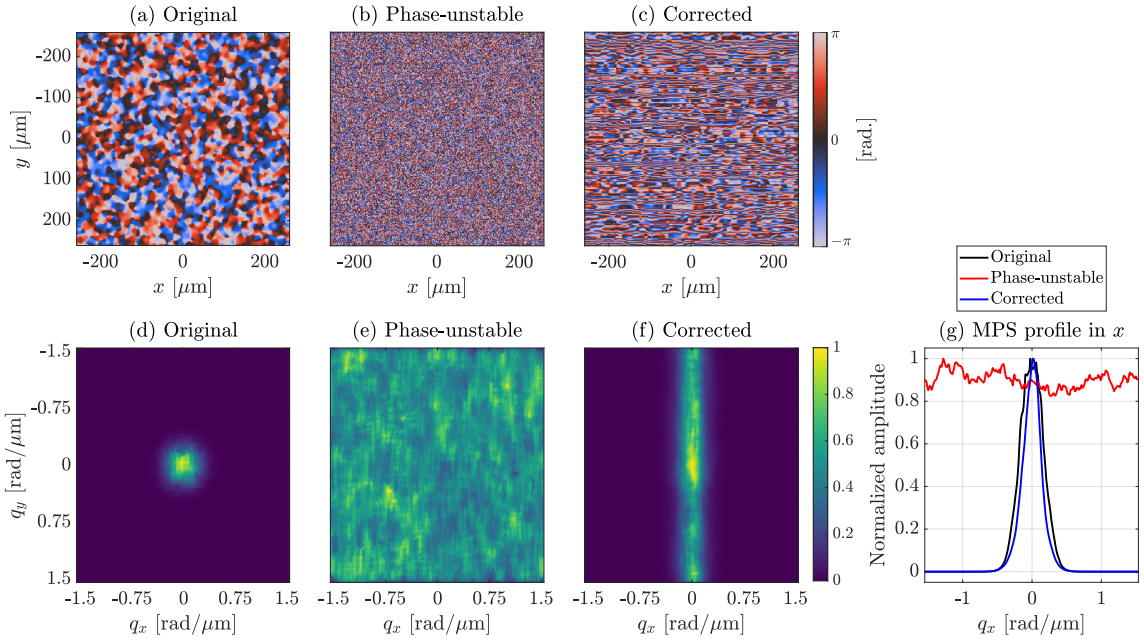

Figure 3.2: Illustration of the mean power spectrum after phase correction with a simulated OCT tomogram. *En face* phase images: (a) original, (b) phase-unstable with random phase-jumps and (c) phase corrected along x. (d)-(f) MPS images of (a)-(c), respectively. (g) 1D profile of the MPS by averaging (d)-(f) along q_y.

3.1.2. Attempts to 2D phase stabilization

The presence of 2D phase noise requires a 2D correction but the fully numerical phase stabilization described previously is insufficient since its operation is intrinsically 1D. Two particular expansions of the phase stabilization method could be devised to achieve 2D phase stability, however, it is shown here that such attempts do not succeed, and in general, any stabilization based on traditional 1D phase correction.

The first intuitive attempt to 2D phase stabilization is to perform two successive 1D phase corrections along the two scan axes. However, it has been found that the second correction would destroy the first correction, hence phase stability is achieved only along the axis that was corrected last. Results from this proposal were obtained using the phase-unstable simulated dataset used for Fig. 3.2 and are illustrated in Figure 3.3 showing cross-sectional images of the plane z-x (B-scan) and the orthogonal plane z-y.

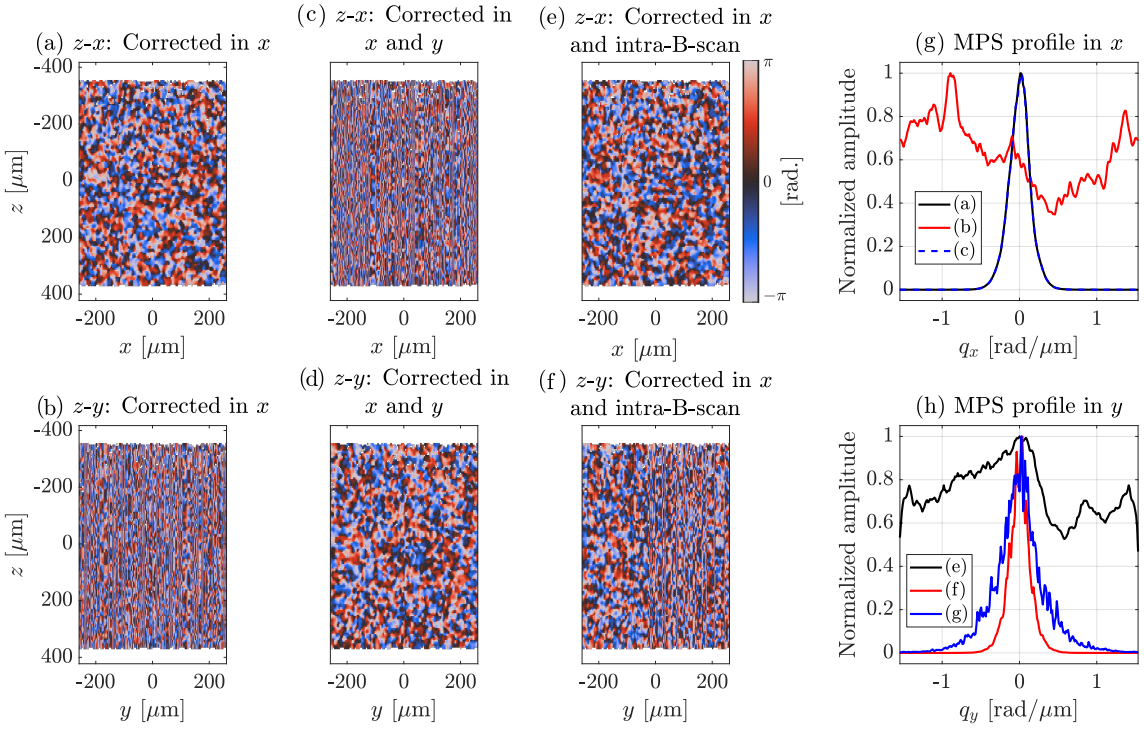

Figure 3.3: Illustration of attempts to 2D phase stabilization with a phase-unstable simulated dataset. Cross-sectional views of: (a)-(b) tomogram corrected along x axis, (c)-(d) tomogram corrected along x axis and then along y axis, (e)-(f), tomogram corrected along x axis and then inter-B-scan. (a),(c),(e) are views of z-x planes and (b),(d),(f) of z-y planes. 1D Profile of the MPS: (g) in x axis and (h) in y axis.

The phase-unstable tomogram was corrected along the x axis and resulting cross-sectional views are shown in Figs. 3.3(a) and (b), which exhibit phase stability in the plane z-x but not in the plane z-y. After the first correction, the phase was corrected along y axis expecting to obtain 2D phase stability, but instead, the phase is corrupted again in the plane z-x and only the plane z-y is stable, as shown in Figs. 3.3(c) and (d). This demonstrates that two consecutive 1D phase stabilizations are not suitable to correct 2D phase noise. Because cross-section images are representative of a single plane, it is useful to analyze the MPS in order to know the general behavior of the entire tomogram. The x and y profiles of the MPS of the tomogram corrected only in x and the one corrected in both axes are shown in Figs. 3.3 (g) and (h). Note that the MPS of the tomogram corrected only along x is phase-stable in this axis [black

curve in Fig. 3.3(g)] but it is phase-unstable in y axis [black curve in Fig. 3.3(h)], contrary to the MPS of the tomogram corrected consecutively along the two axes [red curves in Figs. 3.3(g) and (h)].

A second attempt to 2D phase stabilization is to correct the phase along one axis, and then to correct only for residual global phase noise between consecutive planes in the orthogonal axis. This way, the first correction will not be destroyed as in previous proposal. For instance, if phase is corrected along x, resulting in the corrected tomogram $\tilde{S}(m,n,l)$, then the second correction would be computed using the phase difference between A-lines along y axis, that are then averaged along x axis to obtain a global correction for each B-scan, instead of obtaining an individual correction for each A-line. The global corrections Δ_n between B-scans (or simply inter-B-scan) are calculated as

$$\begin{aligned} \delta(n) &= \arg\left\{\sum_{l=1}^{N_z}\sum_{m=1}^{N_x}\tilde{S}(m,n,l)\tilde{S}^*(m,n-1,l)\right\} \\ \Delta(n) &= \sum_{\hat{n}=1}^{n}\delta(\hat{n}), \end{aligned} \tag{3.4}$$

and are then applied as

$$\tilde{\tilde{S}}(m,n,l) = \tilde{S}(m,n,l)e^{-i\Delta(n)}, \tag{3.5}$$

where N_x is the number of A-lines in x axis and N_z is the number of depth samples. Note that $\Delta(n)$ is a function of B-scan index n only. The purpose of the inter-B-scan correction is to correct for errors along the second axis without destroying phase stability along the first axis since it is a global correction for each B-scan. The latter is well-accomplished as noted in the B-scan phase image in Fig. 3.3(e) that was corrected in x and then inter-B-scan, but the inter-B-scan correction seems insufficient to correct for phase noise along y axis. Fig. 3.3(f) appears to be phase-stable only in the left portion of the image, but not towards the right region, suggesting that a global correction is not sufficient. This is also observed in the MPS profiles; MPS in x axis [blue curve in Fig. 3.3(g)] is almost identical to that corrected only along x, but MPS in y axis [blue curve in Fig. 3.3(h)] exhibits residual high frequency content that suggests significant residual phase noise.

The impossibility to correct for 2D phase noise using traditional 1D phase stabilization may arise because small local errors, insignificant for local phase stability, are induced in the process, and they propagate along the orthogonal direction as a consequence of the cumulative sum used to compute the global corrections. Such errors result in long-range errors that randomly disrupt the phase along this axis and

frustrate any attempt to obtain 2D phase stability using traditional 1D corrections.

3.1.3. Description of the method

To enable the operation of CAC techniques in tomograms with 2D phase noise like those acquired with SSOCT systems presenting phase-jitter, it is possible to develop a scheme that leverages from 1D phase stability instead of aiming to succeed in 2D phase stabilization which is so far not possible with traditional phase correction. Here, a novel technique is proposed for computational correction of aberrations in OCT tomograms with 2D phase noise, which leverages from the fact that 1D short-range phase stability is sufficient to perform the deconvolution operation in which CAC techniques are grounded, from this arises the name of the technique **SH**ort **A**line-**R**ange **P**hase-stability adaptive-optics (SHARP) [72].

SHARP integrates sequential 1D numerical phase stabilization and aberration correction steps and it can operate in tomograms with phase noise arising from phase-jitter, galvanometer scanners, and sub-resolution sample axial bulk motion, as long as Nyquist sampling is fulfilled. SHARP is suitable for OCT systems with no special hardware phase reference signals nor specialized configurations that ensure phase stability along any scanning axis like those used often in the context of CAO. In particular, it is compatible with standard SSOCT systems, affected by 2D phase noise.

The procedure consists of two sequential steps linked by an intermediate step as follows. First, phase noise is corrected along one axis u (being u either x or y) followed by a 1D aberration compensation in that axis. Secondly, phase noise correction in u is rolled-back by applying the inverse correction to the 1D *corrected* tomogram. Then, phase noise is corrected along the other axis v, orthogonal to u, followed by a 1D aberration compensation in v, yielding a 2D computationally aberration-corrected volume. The intermediate roll-back (RB) step is a key step to remove the long-range phase errors introduced in the first correction that would frustrate the second phase correction, and thus it enables the second CAC step.

A flowchart summarizing the procedure is shown in Figure 3.4. $S_{m,n,l}$ is the input aberrated, phase-unstable tomogram. $\mathbb{C}_u\{\cdot\}$ represents the phase stabilization procedure applied along a generic axis u and $\mathbb{C}_u^{-1}\{\cdot\}$ is its inverse indicating that the inverse phase correction is applied to cancel out the initial correction. $\mathbb{A}_u\{\cdot\}$ represents the aberration correction procedure applied along a generic axis u. Finally, $\tilde{S}^{1D}_{m,n,l}$ and $\tilde{S}_{m,n,l}$ are the output, aberration-corrected tomograms, being $\tilde{S}_{m,n,l}$ the two-dimensional corrected tomogram that is the general interest, and $\tilde{S}^{1D}_{m,n,l}$ the one-dimensional aberration-corrected tomogram that is the aim in certain applications where 2D aberration correction is not possible for specific reasons subject to the

application, for instance, in catheter-based imaging. An optional, additional step is to roll-back the second phase noise correction, thus recovering the original phase-unstable tomogram but with aberrations already corrected. This could be useful to combine SHARP with other phase-dependent techniques that would be carried out after the application of SHARP.

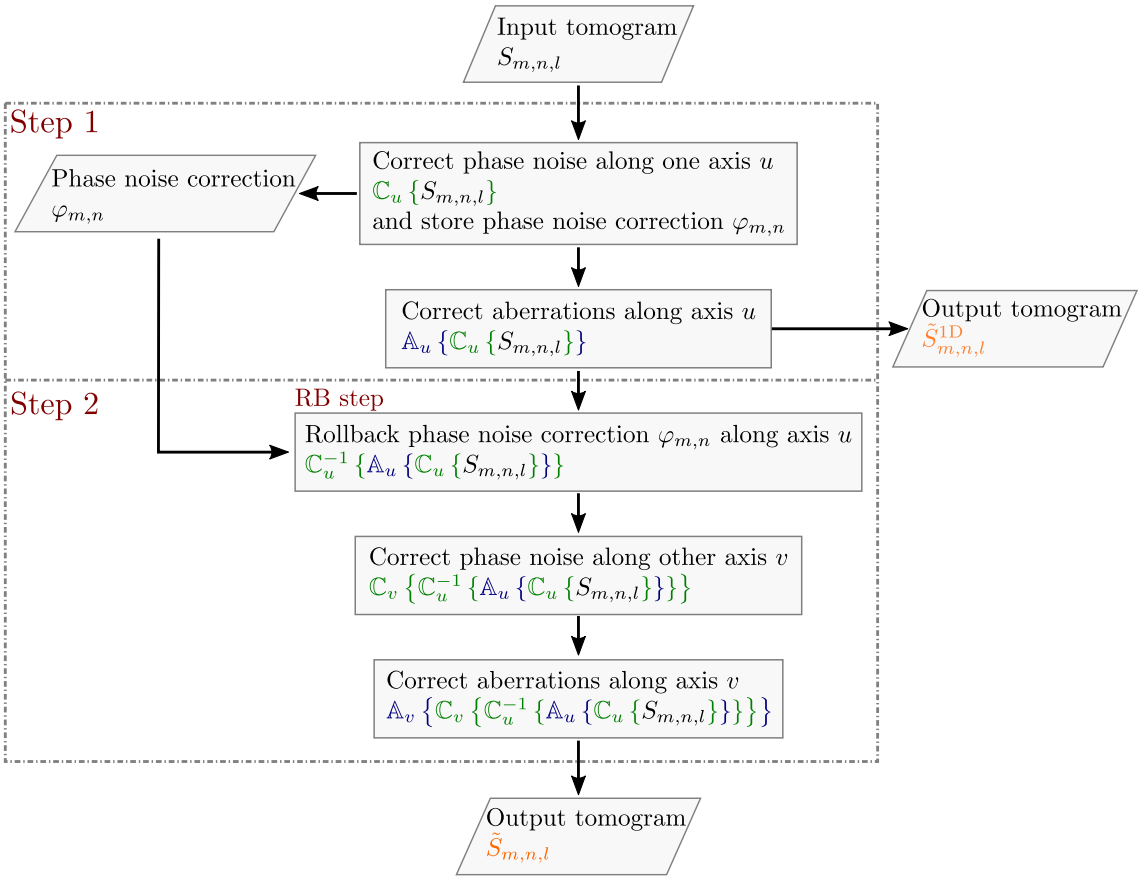

Figure 3.4: Flowchart of the SHARP procedure.

Phase noise correction

For the phase noise correction steps, a modification of the fully numerical method described in Section 2.3.5 is used in order to address phase-jitter noise in addition to phase-offsets already covered by the method. The phase differences between consecutive A-lines along the axis of interest, for instance x axis, are computed similarly to Eq. (2.35) as

$$\delta(m,n,l) = \arg\left\{S(m,n,l)S^*(m-1,n,l)\right\}, \tag{3.6}$$

except that instead of summing along depth as in Eq. (2.35), a linear fit of the form $\hat{\delta}(m,n,l) = b_0(m,n) + b_1(m,n)l$ is performed on $\delta(m,n,l)$. This allows to estimate

the phase offsets $b_0(m,n)$, arising from all potential sources such as galvanometer scanners or axial motion, as well as slopes $b_1(m,n)$ arising from phase-jitter noise. In other words, phase noise of each A-line is characterized by a phase-ramp noise with offset $b_0(m,n)$ and slope $b_1(m,n)$, with both parameters changing randomly across A-lines. Finally, phase correction operator $\mathbb{C}_x\{\cdot\}$ is applied to correct for phase-ramp noise as

$$\begin{aligned} \mathbb{C}_x\{S(m,n,l)\} &= e^{i\hat{\Delta}(m,n,l)}S(m,n,l) \\ \text{where} \quad \hat{\Delta}(m,n,l) &= \exp\left\{\sum_{\hat{m}=1}^{m}\hat{\delta}(\hat{m},n,l)\right\}. \end{aligned} \tag{3.7}$$

The same procedure is applied to correct along y axis, making y as the variable of interest (n in discrete notation). Logarithmic intensities of the conjugate products $10\log_{10}\left\{|S_{m,n,l}S^*_{m-1,n,l}|^2\right\}$ are used as weights to perform a weighted-linear fit. Furthermore, a mask is applied to ignore those pixels with logarithmic intensity below a threshold value, typically set to the noise floor level which is a parameter that in general is constant over the tomogram.

Given that the phase of a complex quantity is defined in the range $[-\pi,\ \pi]$, phase wrapping may appear in Eq. 3.7 if the phase-ramp exceeds these boundaries. It was already explained that phase wrapping is not an issue for phase-offsets correction (Section 2.3.5), but for the case of phase-slopes, wrapping can influence the linear fit, resulting in an erroneous correction. Therefore, phase unwrapping before the linear fit would be desirable to provide a more confident correction, however, it is challenging to perform an adequate phase unwrapping of the OCT signal given the presence of noise and speckle, and in practical terms, it has been found that phase wrapping is not as critical as anticipated in this particular case. To clarify this, first consider that SSOCT systems are equipped with a sampling clock to produce a trigger signal, typically using a fiber Bragg grating, making that the magnitude of phase-jitter is generally below one sampling cycle, equivalent to slopes below 2π, being this the limit for phase wrapping. Furthermore, timing jitter greater than two or three sampling cycles is seldom observed, in a standard system in normal conditions.

Furthermore, although the imaging range of SSOCT systems is typically up to $\sim$6 mm, the effective axial range covered by tissue is in general equal or less than half the imaging range due to light absorption in the tissue. This means that the range where the phase-ramp is fitted is less than half the imaging range, reducing the susceptibility to phase-wrapping because only a portion of the ramp is used and not its entire extension. For instance, a timing jitter of two sample clocks results in a phase-ramp with an effective range of 4π in the full axial range but only with an

effective range 2π if the half axial range is used. Finally, before performing the linear fit, global phase offsets computed by averaging $\delta(m,n,l)$ along depth are subtracted to $\delta(m,n,l)$ to avoid the phase-ramp starting at a value where it could wrap.

Further experimental validation of SHARP will demonstrate that in practical terms these considerations and strategies are sufficient for the linear fit in the phase correction procedure despite the lack of phase unwrapping.

Aberration correction: Phase filter

For the aberration correction step, the idea behind SHARP is to perform two 1D independent corrections instead of a single 2D correction, given that only 1D phase stability is achieved in each phase noise correction step. This is possible assuming that the deconvolution process performed in CAC techniques can be separated into two 1D deconvolutions performed independently and sequentially, which is valid only for certain aberrations, more specifically for those aberrations represented by a deconvolution kernel that can be separated into two 1D kernels, referred here as *x-y-separable aberrations*. In SHARP, computational adaptive optics (CAO) approach (see Section 2.3.3) is adapted to a 1D operation. To do so, consider the expression for CAO in Eq. (2.29) written as

$$\tilde{\eta}(x,y,z) = \mathrm{FT}^{-1}_{q_x,q_y}\left\{\mathrm{FT}_{x,y}\left\{S(x,y,z)\right\} H^{-1}(q_x,q_y,z)\right\}, \tag{3.8}$$

and assume that the complex filter $H(q_x,q_y,l) = H_{q_x}(q_x,z)H_{q_y}(q_y,z)$ is separable into two 1D complex filters, namely $H_{q_x}(q_x,z)$ and $H_{q_y}(q_y,z)$, that are applied independently using the 1D aberration correction operator $\mathbb{A}_x\{\cdot\}$ as

$$\mathbb{A}_x\left\{S(x,y,z)\right\} = \mathrm{FT}^{-1}_{q_x}\left\{\mathrm{FT}_x\left\{S(x,y,z)\right\} H_{q_x}(q_x,z)\right\}, \tag{3.9}$$

where x is the axis of interest, and similarly for y axis by making y as the variable of interest. The filter $H = \Omega e^{i\varphi}$ comprises amplitude Ω and phase φ. In CAO, an approximate estimation $\tilde{\varphi}$ of the ideal and unknown phase φ is defined in terms of a polynomial basis similarly to Eq. (2.30), but in SHARP a 1D polynomial basis P_j is used instead of a 2D basis,

$$\tilde{\varphi}(q_x,z) = \sum_{j=1}^{K} \vec{\alpha}_j(z) P_j(q_x), \tag{3.10}$$

where K is the number of polynomials used and $\vec{\alpha}_j(z)$ are the set of K weights defined for each depth z. In SHARP, we use Legendre Polynomials P_j (see Wolfram

or Ref. [159] for a quick revision if desired), being the first few orders

$$
\begin{aligned}
P_0(x) &= 1 \\
P_1(x) &= x \\
P_2(x) &= \frac{1}{2}(3x^2 - 1) \\
P_3(x) &= \frac{1}{2}(5x^3 - 3x) \\
P_4(x) &= \frac{1}{8}(35x^4 - 30x^2 + 3) \\
P_5(x) &= \frac{1}{8}(63x^5 - 70x^3 + 15x).
\end{aligned}
$$

There is not a 1D polynomial basis to describe aberrations, hence the choice of the polynomial basis is rather arbitrary because many bases will serve equally. For instance, defocus aberration can ideally be corrected with any quadratic polynomial (P_2 in Legendre's basis), although the weight value itself could vary from one basis to another. Zernike polynomials, the standard for the description of aberrations, is a 2D basis thus it is not suitable for SHARP.

To determine the optimal set of weights $\vec{\alpha}_j(z)$ that minimizes aberrations in the tomogram, SHARP employs an image sharpness quality metric based on Shannon's entropy given by Eq. (2.31). This metric, widely used in CAO literature [61,160,161] is robust to point objects as well as extended objects which are appropriate features for a reliable estimation of the optimal weights. The optimization procedure is carried out using the MATLAB's built-in function *fminsearch* that employs the simplex algorithm [162].

Amplitude filter

The amplitude term Ω of the filter H could be defined analytically based on the known properties of the probe beam, but this results in the amplification of undesired high-frequency noise because the inverse filter Ω^{-1} is applied in CAO. Given that amplitude term does not have a role in the correction of aberrations, but only in the apodization of signal strength for each frequency component, it is possible to simply use a unity-valued amplitude $\Omega = 1$ [34,35,61]. There are, however, better approximations that aim to improve the results of the deconvolution process in terms of robustness to noise. An alternative, initially proposed for the restoration of astronomical images [163], is the so-called optimum filter (OF) that is constructed under the reasonable condition that the deviation of the noisy image $\tilde{I}(u) = I(u) + N(u)$ affected by noise $N(u)$ from the ideal noiseless image $I(u)$ should be minimum in the root-mean-square

error sense [164], yielding the form of the OF as

$$\tilde{\Omega}(q) = \frac{|\hat{I}(q)|^2}{|\hat{I}(q)|^2 + |\hat{N}(q)|^2}, \tag{3.11}$$

where u is the variable in the measuring domain, q is its conjugate in the Fourier domain, $\hat{I}(q) = \mathrm{FT}_u\{I(u)\}$ and $\hat{N}(q) = \mathrm{FT}_u\{N(u)\}$. Developed models for noise in OCT predict that noise is additive following a zero-mean Gaussian distribution, namely *white* noise, thus its spectrum is flat, i.e. frequency-independent, which means that $|\hat{N}(q)|^2$ is nearly constant. Under the previous model, and because the noiseless signal is in general unknown, the OF can be rewritten as

$$\tilde{\Omega}(q) = \frac{|\tilde{\hat{I}}(q)|^2 - |\hat{N}(q)|^2}{|\tilde{\hat{I}}(q)|^2}, \tag{3.12}$$

where $\tilde{\hat{I}}(q) = \mathrm{FT}_u\{\hat{I}(u)\}$ is the Fourier transform of the measured noisy signal.

For the particular context of OCT, SHARP makes use of the MPS to define $|\hat{I}(q)|^2$, resulting in a smooth and overall filter for the entire tomogram. Given the 1D operation, the 1D MPS is used, obtained by averaging $\bar{\xi}(q_m, q_n)$ over the lateral axis that is not the interest, for instance averaging over q_y as $\bar{\xi}_{q_m}(q_m) = \frac{1}{N_y}\sum_{q_n}^{N_y}\bar{\xi}(q_m, q_n)$ when filtering along x axis. Therefore the OF in SHARP is

$$\tilde{\Omega}(q_m) = \frac{\bar{\xi}_{q_m}(q_m) - \bar{\xi}_{q_m}(q_{N_m})}{\bar{\xi}_{q_m}(q_m)}, \tag{3.13}$$

where $|\hat{N}(q)|^2 = \bar{\xi}_{q_m}(q_{N_m})$ is an approximate estimation to the noise floor level assuming that the content of the MPS at the maximum frequency q_{N_m} is dominated by noise, which is indeed valid given the Gaussian-shape of the MPS. In practice, rather than using directly the value at the maximum frequency, it is convenient to average the value for a few more frequencies around it. The OF is an effective tool, not only to avoid amplification of high-frequency noise, but also to slightly reduce the noise floor level in the complex tomogram. Its application is straightforward since it is defined based on the data information alone; it is an adaptive filter. Handling noise is advantageous particularly for CAO because it is known that out-of-focus tomograms present lower signal-to-noise ratio (SNR) than in-focus tomograms.

An example of the optimum filter calculated from an ideal Gaussian MPS is depicted in Fig. 3.5. The amplitude of the filter is nearly constant and equal to one for the low-frequency content, where the signal dominates, and decreases to zero towards the maximum frequency to filter out high-frequency components beyond the

cutoff frequency that are dominated by noise.

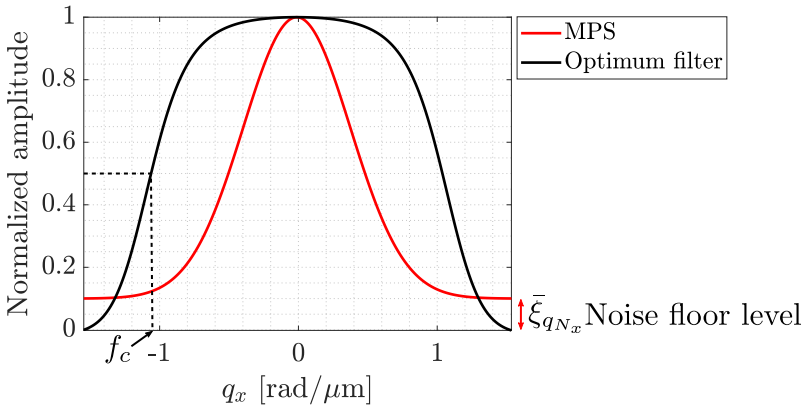

Figure 3.5: Example of the optimum filter for a Gaussian MPS. fc: cutoff frequency of the filter.

Now that the phase stabilization and aberration correction procedures have been defined, the two 1D steps of SHARP can be condensed as

$$\tilde{S}^{1\mathrm{D}}(x,y,z) = \mathbb{A}_x\left\{\mathbb{C}_x\left\{S(x,y,z)\right\}\right\}, \tag{3.14}$$

$$\tilde{S}(x,y,z) = \mathbb{A}_y\left\{\mathbb{C}_y\left\{\mathbb{C}_x^{-1}\left\{\tilde{S}^{1\mathrm{D}}(x,y,z)\right\}\right\}\right\}, \tag{3.15}$$

where $\tilde{S}^{1\mathrm{D}}(x,y,z)$ is the partially corrected tomogram and $\tilde{S}(x,y,z)$ is the x-y-separable aberration-corrected tomogram.

There are some particularities to discuss concerning the described procedure. Because SHARP employs CAO, its operation is limited to low-to-medium NA systems, that are typically used in OCT. An extension to operate with high-NA systems could be possible by integrating ISAM in SHARP, however, this is the regime of OCM, which is not the aim in this work, and it is yet unclear whether the ISAM procedure is compatible with the 1D operation of SHARP.

The x-y separability requirement limits the correctable aberrations to those with a deconvolution kernel that can be separated into two 1D kernels. Among the x-y-separable aberrations, the most important for practical terms are defocus, xy-astigmatism, and comma, being defocus the most relevant in many OCT applications given that it is intrinsic to the nature of the focused Gaussian beam used to illuminate the sample. In fact, defocus can be considered the only significant aberrations in many applications of OCT apart from retinal imaging where complex wavefronts may be induced by the eye of the subject. This means that SHARP is sufficient for many scenarios despite its x-y-separability requirement, in particular, to numerically extend the depth of field, relaxing the lateral-resolution–DoF trade-off.

Another important aspect is the role of the roll-back step. The process of phase

noise correction along the first axis adds random phase errors along the orthogonal axis that can become strong enough to frustrate the subsequent phase correction along the second axis. With no RB step, second phase noise correction results in lower local phase stability than the case of correcting the second axis directly, i.e. without correcting the first axis previously. The purpose of the RB step is to cancel out the first phase noise correction to avoid any significant error induced in the first correction. The RB step uses the phase noise correction computed before correcting aberrations along the first axis but the RB itself is performed after correcting aberrations, which may change the phase pattern. Interestingly, the aberration correction applied along the first axis does not perturb the relative phase relationship in the second axis although the phase pattern itself may have changed, hence the exact same phase noise correction is still valid for the RB (but conjugated) even though it is applied after aberration correction.

3.2. Proof of concept experimental validation

To validate SHARP, an experiment was carried out in which a sample was imaged with a phase-unstable SSOCT system, inducing defocus on purpose by placing the focal plane of the scan lens outside the tissue. A raster-scan, non-k-clocked SSOCT system with a polygon-based wavelength-swept source was employed, similar to that in the schematic of Figure 2.5. This custom-built system is affected by strong jitter in synchronization, as well as additional phase noise sources, such as the frequency shifter used to double the axial imaging range, that adds spurious phase offsets [102] and the galvanometer mirrors, since the back-focal plane of the lens is not aligned with the pivot points of the galvos. The A-line repetition rate was 54 kHz, in a 120 nm 10-dB-sweep spectral range centered at wavelength 1310 nm. The light was focused onto the sample using a scan lens with a transverse e^{-2} beam diameter of $2w_0 = 22$ μm in a Rayleigh range of $z_R = 290$ μm in air (Thorlabs LSM03, USA).

A *cucumis sativus* sample was selected for the experiment as it displays prominent cellular walls with strong scattering and large vacuoles with low scattering. The sample was imaged in a 3×3 mm^2 lateral FoV within a ranging depth of 6 mm in air, acquiring 1024 samples per A-line, 512 A-lines per B-scan, and 512 B-scans, for a total tomogram size of 1024×512×512 ($N_z \times N_x \times N_y$). A reference dataset was acquired by placing the focal plane roughly 0.6 mm below the sample surface, referred to as *in-focus* or reference tomogram and the out-of-focus (OoF) dataset was acquired after shifting up the focal plane roughly 0.9 mm, thus located above the sample surface.

SHARP was applied to the OoF tomogram using Legendre polynomial P_2 to describe the phase filter given that defocus is the only significant aberration in the

experiment. Figure 3.6 illustrates the results of each step of SHARP. A zx cross-sectional phase image in a small region of interest (ROI) of the raw unstable phase tomogram is shown in Fig. 3.6(a), and after phase noise correction in x, or simply $\mathbb{C}_x$, in Fig. 3.6(b), a point in which the MPS profile in x exhibits a Gaussian shape and not a distorted one as original tomogram [Fig. 3.6(c)]. After 1D CAO along x axis (denoted as SHARP-x), the zy plane remains phase-unstable [Fig. 3.6(d)], but after the RB step and $\mathbb{C}_y$, the zy plane is now phase-stable [Fig. 3.6(d)] obtaining a MPS profile with Gaussian shape along y [Fig. 3.6(f)]. Without RB the MPS is distorted, approaching a Gaussian function but with remnant high-frequency noise that suggests the presence of local phase instabilities that could frustrate CAO, as noted in the offset of the green curve compared to the orange curve in Fig. 3.6(f). Finally, a 2D refocused tomogram is obtained after applying 1D CAO in y.

Figures 3.6(g)–(l) show intensity *en face* views of the original tomogram, after SHARP-x showing 1D refocusing only, after SHARP showing 2D refocusing and after SHARP without RB resulting in degraded quality of fine details, for instance in the region enclosed by the red circle, demonstrating the importance of the RB step. Additionally, results from failed attempts are illustrated; refocusing without any phase stabilization in Fig. 3.6(j), showing the destruction of signal information, and refocusing after phase stabilization only along the out-of-plane axis in Fig. 3.6(k), as is traditionally performed in SDOCT systems having in-plane phase stability [65], which also fails here because it is not sufficient for systems having 2D phase noise.

Figure 3.7 presents *en face* views located at depths $\sim 2.0z_R$, $3.5z_R$ and $5.0z_R$ from the focal plane of the OoF tomogram before and after SHARP, and of the corresponding in-focus reference tomogram. SHARP successfully restored the OoF tomogram despite the strong phase noise, providing images with better resolution and contrast than original images as a result of blurring correction. Also, the filtering effect of the optimum amplitude filter served to reduce the average noise floor level from 63 dB to 59 dB, a difference corresponding to 1/10 of the images dynamic range 60–100 dB. In particular, cell walls of the sample are significantly sharper after SHARP compared to the original, approaching the in-focus counterparts, demonstrating the effectiveness of SHARP to correct for defocus.

For shallow depths, $2.0z_R$ and $3.5z_R$, SHARP produced successful results when compared to the reference images. For the deepest plane shown, at $5.0z_R$, refocusing seems to be efficient only for a small region having low signal density (see red boxes in Fig. 3.7), whereas the surrounding signal-dense region seems to be uncorrected. This may be a consequence of multiple scattering, which is likely to be stronger in these dense regions, and it is known that the deconvolution model only accounts for single-scattered or *ballistic* photons, thus it is expected that the large contribution of multiple scattering hinders CAO, in this case for planes at $z > 5.0z_R$ but this limit

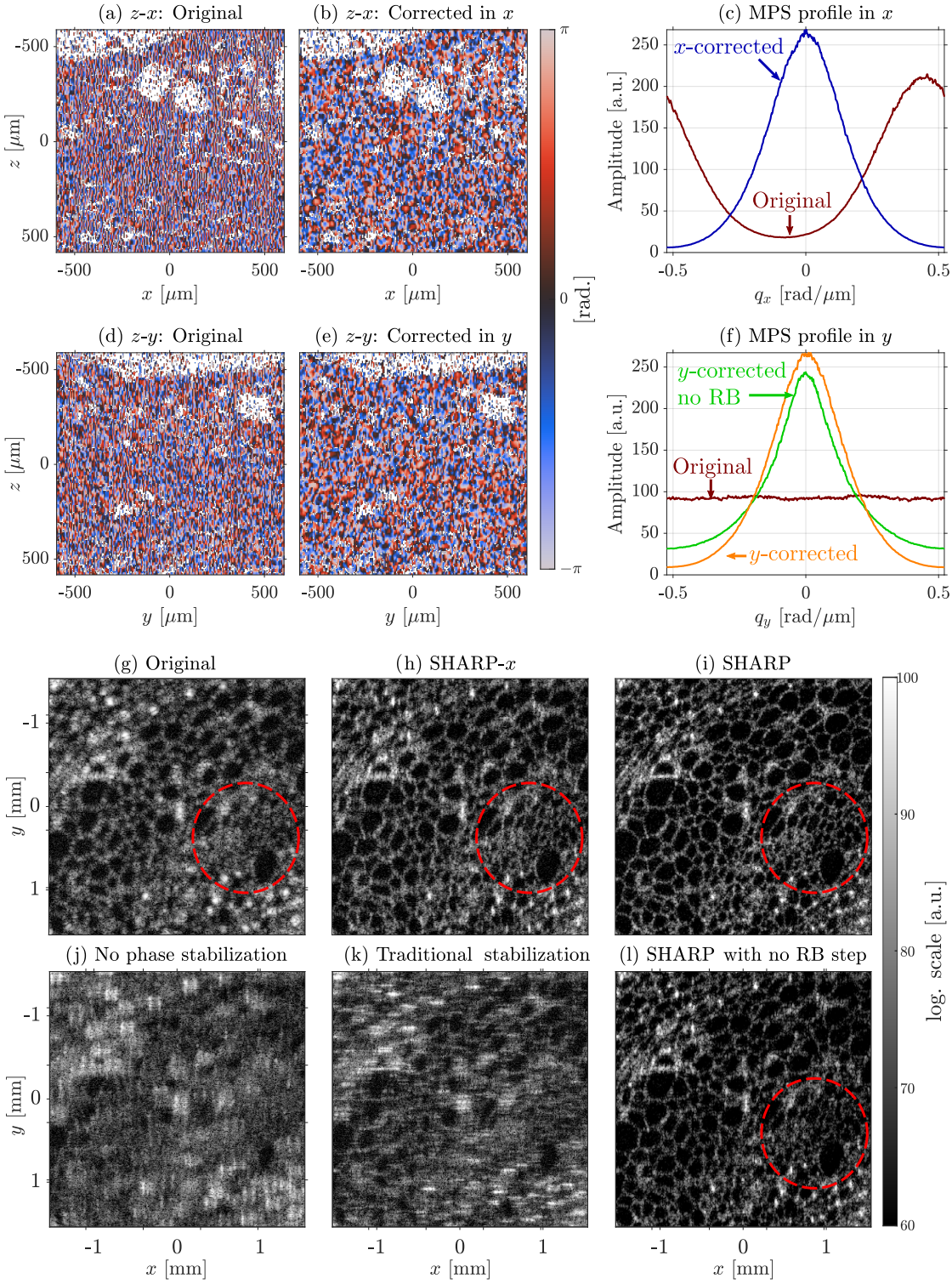

Figure 3.6: B-scan phase maps of *cucumis sativus* sample in a small ROI; (a) before, (b) after $\mathbb{C}_x$ and (c) corresponding MPS profiles. z-y phase maps; (d) before, (e) after $\mathbb{C}_y$ and (f) corresponding MPS profiles with and without RB step. Intensity *en face* views; (g) original, (h) SHARP-x, (i) SHARP, (l) SHARP without RB step, (j) 2D CAO with no phase stabilization and (k) with out-of-plane stabilization [65].

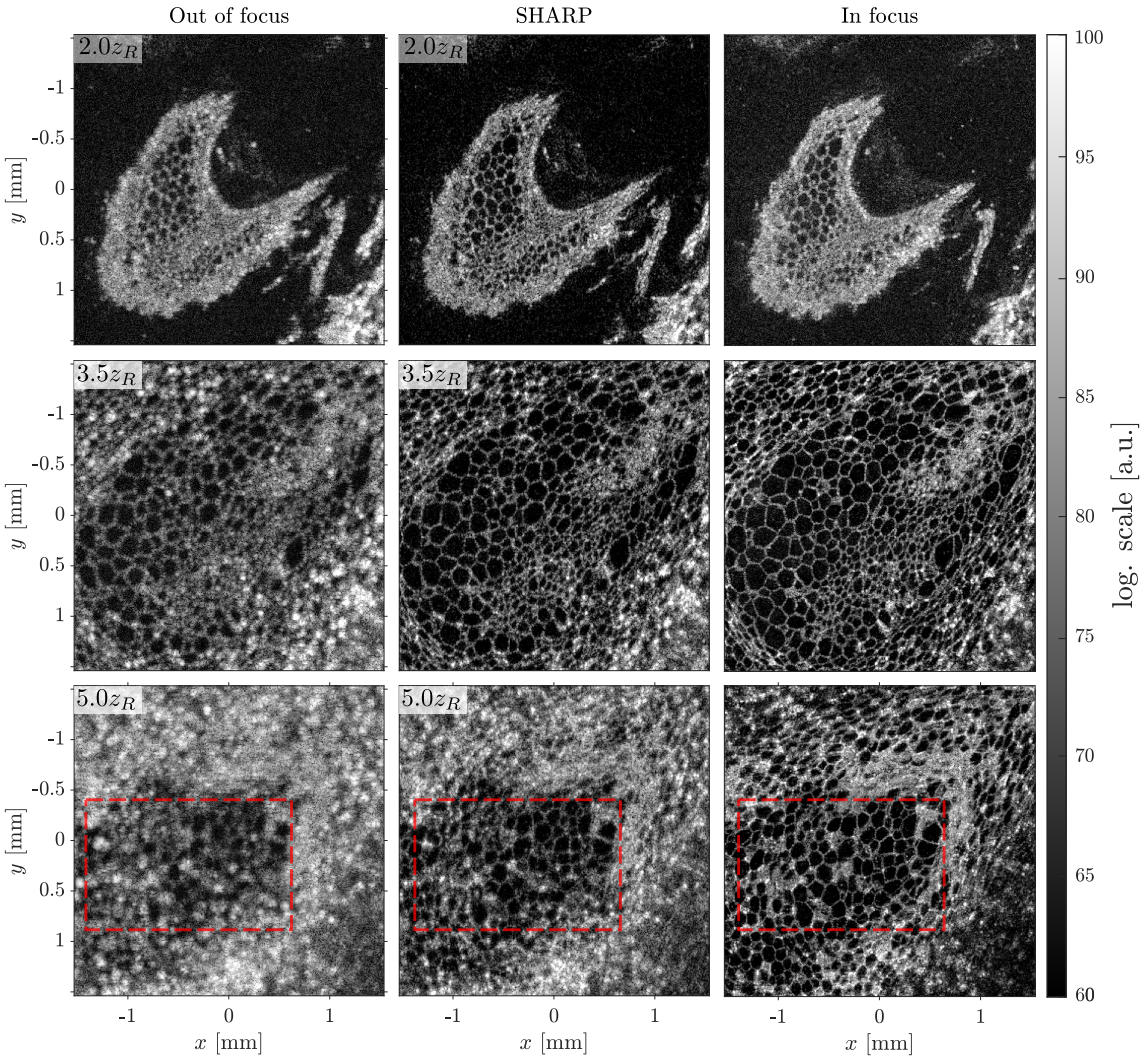

Figure 3.7: Comparison of several *en face* views of out-of-focus, SHARP, and in-focus tomograms, at depths $2.0z_R$, $3.5z_R$, and $5.0z_R$ as indicated in each image.

is sample-dependent.

SHARP was implemented in MATLAB and it took around 560 seconds to process the OoF tomogram in an ROI of size 450×512×512, using MATLAB 2019a in a workstation computer running on an Intel Core i7-8700 processor @ 3.2GHz. Aberration correction steps are the most computational expensive because of the optimization procedure performed in CAO, taking around 528 seconds for all planes including the two 1D corrections. In practical scenarios, it is possible to run the optimization only for certain planes and then to fit the optimal weights to find the correction for the intermediate planes, given that evolution of aberrations over depth is certainly smooth, and this will effectively reduce computation time.

3.3. Extending SHARP

3.3.1. Complex amplitude motion artifacts correction

Relevant effects of motion in the OCT signal for the context of CAC were already explained in Section 2.3.4, namely complex amplitude shift and phase-jump. The latter often has greater relevance for CAC, thus phase stabilization methods correct phase offsets, including the phase stabilization performed in SHARP. However, in many *in vivo* applications, complex amplitude shifts may also have a significant influence and could be more noticeable since they affect both the phase and the amplitude of the tomogram, appearing as signal distortions in the structural image [165]. In general, OCT systems are equipped with sample holders or interfaces to reduce the impact of large acute motion. For instance, chin rests and forehead holders in ophthalmic systems or handheld scanners for skin imaging, but there is yet slow, low-frequency motion arising from the heartbeat and respiration of the subject [165].

Motion artifacts can be prevented or corrected by using; a reference motion-free image from other imaging modality [166]; a tracking system that follows and corrects for sample motion *in situ*, employed especially in retinal imaging [167]; or a fast system with volume acquisition rate such that sample appears static during the scanning. A recent report has achieved volume acquisition rates in the order of tens of milliseconds with A-lines rates of the order of MHz [168], but utilizing very specialized components.

With A-line acquisition rates of the order of 100 kHz in current widespread systems, it is possible to assume that, in normal conditions, the sample is static during the acquisition of a single B-scan and motion manifests as rigid-body displacements across different B-scans, in other words, as inter-B-scan bulk displacements. In such a case, complex amplitude shifts can be corrected straightforwardly using image registration [169].

The idea of bulk image registration is to find the relative global shift between two given images $I_1(m,l)$ and $I_2(m,l)$ [170]. Most used method is intensity-based registration where the cross-correlation $r_{\text{cc}} = I_1(m,l) \star I_2(m,l)$ of the two images is computed and the location of the peak is detected to determine the relative shift $(m_{\text{cc}}, l_{\text{cc}})$ between the two images, assuming that they are almost identical except for the relative shift between them. Then, the shift is applied to one of the two images to match one to the other.

Commonly, cross-correlation is computed in Fourier domain as

$$r_{\text{cc}} = \text{FT}^{-1}_{q_m,q_l} \left\{ \text{FT}_{m,l} \left\{ I_1(m,l) \right\} \text{FT}_{m,l} \left\{ I_2(m,l) \right\}^* \right\}, \tag{3.16}$$

where * denotes complex conjugate, then the shift is corrected as

$$I_2 = \mathrm{FT}^{-1}_{q_m,q_l}\left\{\mathrm{FT}_{m,l}\left\{I_2(m,l)\right\}\exp\left[-i2\pi\left(m_{\mathrm{cc}}\frac{q_m}{M}+l_{\mathrm{cc}}\frac{q_l}{L}\right)\right]\right\}, \tag{3.17}$$

where m_{cc} and l_{cc} are given in pixels and $M \times L$ is the image size.

When a sub-pixel estimation is required, the product of the two Fourier-transformed images in Eq. (3.16) is zero-padded prior to computation of the inverse FT in order to have an up-sampled cross-correlation r_{cc}. However, this zero-padding will increase the size of the input of the inverse FT increasing computational cost significantly as the sub-pixel resolution increases, for instance, a $1/20$ resolution requires a zero-padding of $20M \times 20L$. Fortunately, there are efficient sub-pixel image registration methods that significantly improve speed without sacrificing accuracy [170].

Using efficient sub-pixel image registration, it is possible to include a step for inter-B-scan bulk motion correction in SHARP procedure, assuming that transitions between B-scans is smooth, which is valid for typical biological samples scanned with a proper sampling, ideally equal or better than Nyquist sampling. This step, if necessary, is performed after the first phase stabilization step since correcting the complex signal requires phase-stable data. Correction of complex amplitude shifts could enable operation of subsequent steps of SHARP for *in vivo* imaging. Motion is corrected in SHARP by registering the intensity of adjacent B-scans n and $n-1$ and finding the relative lateral and axial shifts $(m_{\mathrm{cc}}(n), l_{\mathrm{cc}}(n))$ as

$$(m_{\mathrm{cc}}(n), l_{\mathrm{cc}}(n)) = \arg\left\{\max\left\{|S(m,n,l)|^2 \star |S(m,n-1,l)|^2\right\}\right\}, \tag{3.18}$$

where the cross-correlation is performed inside the B-scan plane, i.e. along coordinates x and z. Shifts across B-scans are accumulated to computed global shifts with respect to the first B-scan as

$$\mu_{\mathrm{cc}}(n) = \sum_{\hat{n}}^{n} m_{\mathrm{cc}}(\hat{n}) \qquad \text{and} \qquad \Gamma_{\mathrm{cc}}(n) = \sum_{\hat{n}}^{n} l_{\mathrm{cc}}(\hat{n}), \tag{3.19}$$

that are applied to obtain a bulk motion-corrected complex tomogram $S_{\mathrm{mc}}(m,n,l)$,

$$S_{\mathrm{mc}}(m,n,l) = \mathrm{FT}^{-1}_{q_m,q_l}\left\{\mathrm{FT}_{m,l}\left\{S(m,n,l)\right\}\exp\left[-i2\pi\left(\mu_{\mathrm{cc}}(n)\frac{q_m}{M}+\Gamma_{\mathrm{cc}}(n)\frac{q_l}{L}\right)\right]\right\}. \tag{3.20}$$

Additionally, to preserve the surface geometry of the sample, global shifts can be high-pass filtered to cancel out the spurious low-frequency shifts that appear when the sample has a non-flat geometry, for instance, the curvature of the cornea.

With this motion correction step, it could be possible to correct for x-y-separable aberrations with SHARP in tomograms acquired *in vivo* affected by bulk motion subject to the B-scan plane (inter-B-scan), but insignificant out-of-plane motion (intra-B-scan) since it is not addressed in the approach described above, actually out-of-plane corrections demands more sophisticated solutions out of the scope here [171]. To register B-scans, the efficient sub-pixel image registration by cross-correlation algorithm [170] is used here, available in MATLAB Central File Exchange [172].

Figure 3.8 illustrates motion correction with the simulated OCT tomogram used in previous demonstrations. Global lateral and axial shifts were defined randomly for each B-scan and applied to the original motion-free tomogram, then the motion correction procedure was carried out to compensate for the induced shifts using a sub-pixel resolution of 1/20. Figs. 3.8(a)-(c) compare *en face* views of each tomogram, and the effect of inter-B-scan bulk motion can be visualized in Fig. 3.8(b) as distortions and discontinuities along the y axis. This is also evident when comparing the cross-

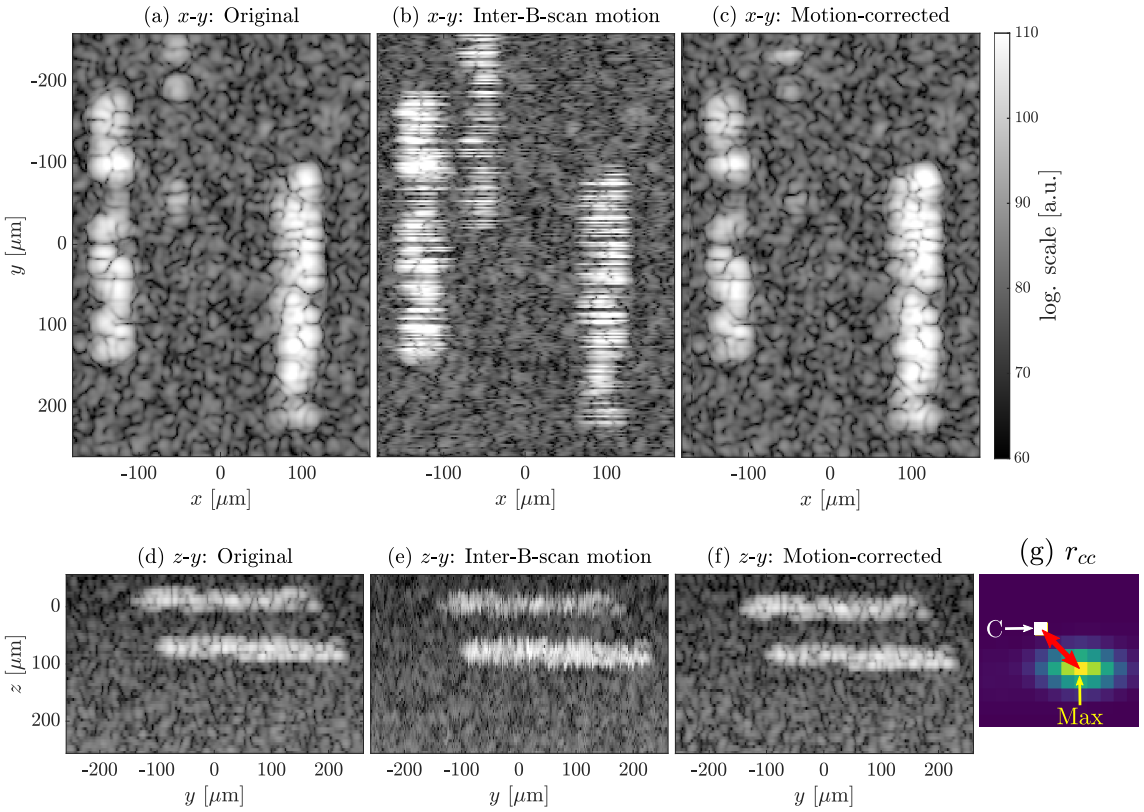

Figure 3.8: Illustration of intra-B-scan motion correction with a simulated OCT tomogram. (a), (d) original; (b), (e) original with induced axial and lateral in-plane bulk motion; (c), (f) motion-corrected using image registration. (a)-(c) are en-face views and (d)-(f) are cross-sections of z-y plane. (g) Example of the cross-correlation between two B-scan with relative motion (not shown). C: center pixel, Max: location of the maximum value of the cross-correlation. The red arrow indicates the estimated shift between the two B-scans.

sectional z-y planes in Figs. 3.8(d)-(f). In both views, it is clear that the motion correction yields a tomogram with no visual artifacts, approaching the appearance of the original one. In Fig. 3.8(g), a zoomed region of the cross-correlation image between two B-scan with a relative shift of 3 pixels is shown, to illustrate how the location of the peak is shifted from the center of the image, indicating the relative displacement.

3.3.2. Spatially-varying aberrations correction

Although the numerical deconvolution in CAO is performed in the Fourier domain for practical simplicity, by applying a complex filter to each *en face* plane, the physical convolution in the image formation process occurs in the spatial domain. The possibility to perform the numerical deconvolution in the Fourier domain relies on the fact that the deconvolution kernel in the spatial domain is constant over the lateral field of view (FoV) —not to be confused with axial depth of field.— The region within this assumption is valid is known as the *isoplanatic-patch*, a term originated from astronomy [173], defined as the region within which aberrations and therefore the point spread function (PSF) do not vary [158]. There are scenarios where the lateral FoV is greater than the isoplanatic-patch, consequently, the PSF is anisotropic, resulting in aberrations that vary across the FoV thus they cannot be corrected entirely using a global filter in the Fourier domain. For instance, it is known that large numerical aperture systems often have a small diffraction-limited lateral FoV and outside this, the resolution degrades progressively. Additional causes of an anisotropic PSF may be imperfect optical components, misalignment, or inhomogeneous samples, for instance, in corneal imaging, where the axial focal position is no longer constant forming a plane, instead, it is curved as a consequence of cornea curvature.

In rigorous terms, spatial-varying aberrations must be corrected locally, using a deconvolution kernel defined individually at each spatial coordinate. This would be computationally expensive and a fully localized correction might not be necessary for certain practical scenarios because the variation of aberrations across the FoV is indeed smooth. To deal with spatial-varying aberration, a CAO approach based on regions of interest has been proposed for sub-aperture-based and optimization-based CAO [156, 158] under the general idea of splitting the FoV into several regions of interests (ROIs) or windows to perform CAO individually in each ROI and then stitching the aberration-corrected ROIs into the original full FoV. Ideally, aberrations within each ROI should be nearly constant, this is achievable using small ROIs, but in practice, there is a limit on the minimum size given that the determination of aberrations in the CAO procedure could fail if few pixels are used.

Based on the former idea, it is possible to perform spatially-varying aberration

correction in the SHARP procedure, as is illustrated in Figure 3.9, instead of using the standard global aberration correction. To do so, each *en face* plane is split into windows of size $W_x \times W_y$ with an overlap of half window size along the axis being corrected, for instance, an overlap of $W_x/2 \times 0$ when correcting in x axis, or $0 \times W_y/2$ for y axis. Given the 1D operation of SHARP, the overlap is not necessary for the axis that is not the interest in each aberration-correction step. The purpose of overlapping the windows is to avoid boundaries artifacts that appear in the composite images when there is no overlap. After performing CAO in each window, full *en face* planes are assembled by extracting a centered ROI of size $W_x/2 \times W_y$ from each window when correcting along x, or $W_x \times W_y/2$ when correcting along y axis. For windows occupying the frontier of the full image in the axis of interest (red box in Fig. 3.9), an extended ROI is selected to keep the same full image size. The appropriate number of windows may change for every tomogram depending on the sample and the anisotropy of aberrations.

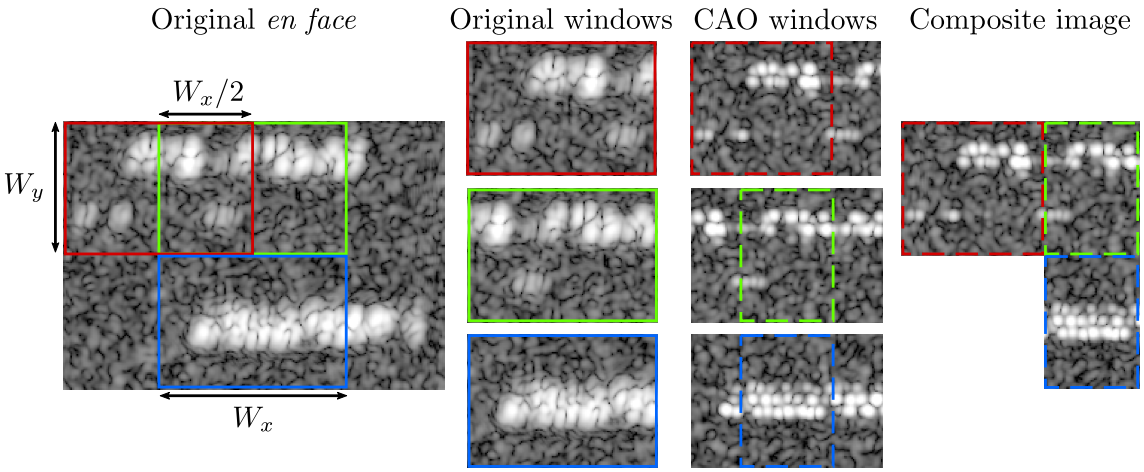

Figure 3.9: Illustration of spatially-varying aberration correction with a simulated OCT *en face*, showing the process for three windows only to facilitate interpretation.

3.3.3. Beyond correction of separable in x-y aberrations

Although SHARP is capable of correcting for defocus and xy-astigmatism, the two major aberrations in OCT for many applications, a clear drawback is the constrain to only correct for x-y-separable aberrations. This restriction could limit the applicability of SHARP, in particular, in retinal imaging applications given that arbitrary aberrations are present depending on the subject's eye [61, 62, 68], It is, therefore, desirable to extend the procedure to cover more general aberrations and expand its applicability throughout more practical scenarios.

In the standard or SHARP-xy procedure, aberrations are corrected along the two main axes x and y. Keeping in mind the 1D operation, it is possible to correct

aberrations along two secondary axes x' and y' obtained as the original axes x and y rotated by 45 degrees with the relationships $x' = x\cos 45° - y\sin 45°$ and $y' = x\sin 45° + y\cos 45°$. In principle, correcting for aberrations in the axes x-y and then in the axes x'-y' provides a global correction of aberrations oriented at an arbitrary angle. For instance, SHARP-xy and SHARP-$x'y'$ can correct for xy- and oblique-astigmatism respectively, then complementing both procedures, it is possible to correct for astigmatism oriented at an arbitrary angle obtained from a combination of the two independent astigmatisms.

The procedure for SHARP-$x'y'$ follows the idea behind the simple steps of the original method with slight differences as explain next and illustrated in Figure 3.10 for a grid of 6×6 pixels. Local phase differences $\delta(m, n)$ for phase noise correction are computed between consecutive A-lines oriented in oblique paths [red lines in Fig. 3.10(b)], denoted by indexes (m, n) and $(m-1, n+1)$ in the case of correcting along x' axis or (m, n) and $(m+1, n-1)$ when correcting along y' axis, then the proper accumulative sum is performed and this way phase stability is achievable across any oblique axis, either x' or y'. After phase stabilization, it is now possible to perform aberration correction along the phase-stable oblique axis.

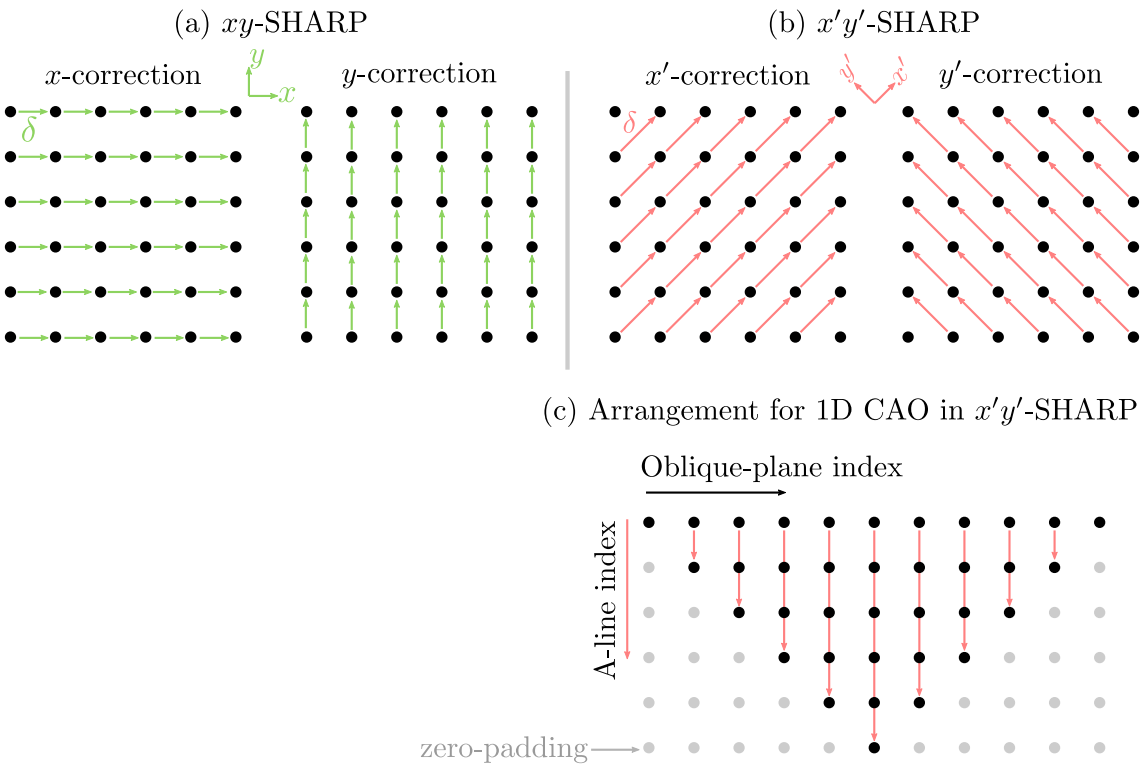

Figure 3.10: Comparison of operation of SHARP-xy and SHARP-$x'y'$ for a grid of 6×6 pixels. (a) Phase differences in SHARP-xy are computed along vertical and horizontal paths, whereas (b) for SHARP-$x'y'$ are computed along oblique paths. (c) The tomogram grid is rearranged to perform CAO along the oblique axes.

The essence of 1D CAO for the oblique axes is the same as that for the main axes but there are changes in the numerical implementation to carry out the corresponding calculations. In a standard tomogram, *en face* plane is arranged with one dimension being the A-line index (x axis) and the other being the B-scan plane index (y axis). To carry out 1D CAO in SHARP-$x'y'$, the tomogram is rearranged in the *en face* plane in such way that one dimension corresponds to the A-line index (x' axis) and the other to the oblique-plane index (y' axis) [see Fig, 3.10(c)]. In addition, the rearranged tomogram is zero-padded to keep a constant oblique-plane size because original planes have different numbers of A-lines. Then, the standard 1D CAO procedure can be applied directly to the rearranged tomogram using the A-line index dimension as the aimed dimension for the calculations.

The zero-padding in the rearrangement step provides a tomogram with uniform size, but it is clear that the number of A-lines with effective (non-zero) information in each oblique-plane index is different, and it approaches one A-line towards the tomogram frontiers. Because of that, planes having fewer A-lines than the deconvolution kernel size are likely to end up with a wrong correction, however, this effect is inconsequential given that it occurs only towards the corners of the FoV.

Because phase differences for noise correction in SHARP-$x'y'$ are computed between A-lines separated by $\sqrt{2}$ times the lateral sampling (and not by exactly the lateral sampling as in SHARP-xy), then to fulfill sampling requirement for CAO, the effective sampling of the tomogram should be $1/\sqrt{2}$ times the Nyquist sampling, i.e. $\delta_x/(2\sqrt{2})$, or smaller. This means that finer lateral sampling is required. This is a key aspect to keep in mind but it does not have important experimental consequences given that in most systems sampling can be adjusted.

In the case of performing SHARP-$x'y'$ after applying SHARP-xy, it is important to roll-back the last phase noise correction after the second aberration correction of SHARP-xy, otherwise, subsequent phase noise corrections are likely to fail. In general, the entire SHARP procedure consists of four steps, each one performing a phase noise and aberration correction along a single axis at a time, connected by their corresponding rollback step. An intuitive order for the axis of interest is each step is first x, then y, then x', and finally y', although the order can be changed indistinctly.

A preliminary test using the simulated OCT tomogram mentioned previously was carried out to verify the correct operation of SHARP-$x'y'$ and results are summarized in Fig. 3.11. To establish a reference for comparison, the intrinsic defocus of the tomogram was corrected using 2D CAO. Aberrations were induced in the original tomogram by applying a phase filter created with Zernike polynomials Z_4 and Z_5 for xy- and oblique-astigmatism with weights 0.8λ and 2.4λ respectively. Figs. 3.11(a) and (b) show one *en face* plane of the aberration-free and aberrated tomograms.

Fig. 3.11(e) shows the induced astigmatism oriented at an arbitrary angle, but close to 45 degrees given that the magnitude of the weight of Z_5 is greater, and it also shows the total aberrated wavefront for the *en face* plane of Fig. 3.11(b) including the intrinsic defocus.

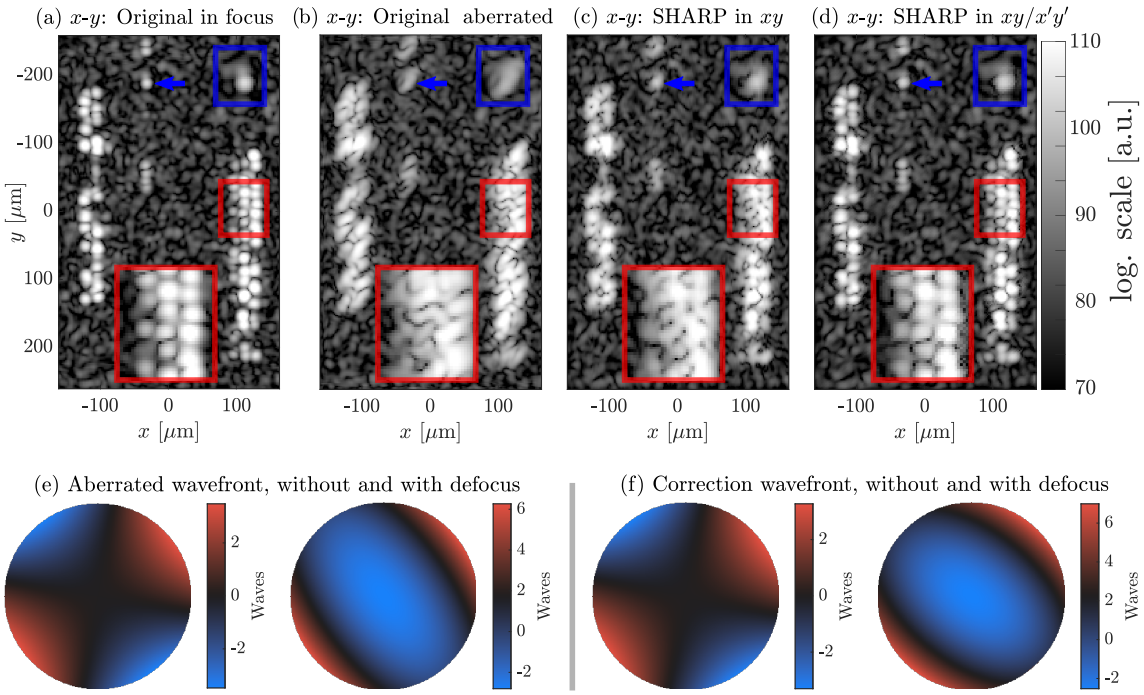

Figure 3.11: Testing aberration correction with SHARP-$x'y'$ using a simulated OCT tomogram. *En face* views of tomograms; (a) original in focus, (b) aberrated, (c) after SHARP-xy and (d) subsequent SHARP-$x'y'$. Wavefront maps for the same *en face* as before; (e) aberrated wavefront and (f) correction wavefront, without (left) and including defocus (right).

Phase noise comprising random offsets and slopes in the range $[0,\ 2\pi]$ was added to the aberrated tomogram. For describing the phase filter in 1D CAO, Legendre polynomial P_2 was used. First, the SHARP-xy procedure was applied, obtaining partial aberration correction as visualized in the *en face* plane of Fig. 3.11(c), followed by application of SHARP-$x'y'$ that resulted in a more noticeable image quality improvement due to aberration correction as noted in Fig. 3.11(d), and approaching the image quality of the original aberration-free tomogram. Compare the red and blue insets for a direct evaluation. Finally, the correction wavefront was computed as a superposition of the individual 1D corrections in the four axes [right panel in Fig. 3.11(f)] and its distribution shows that indeed correction of aberrations not oriented along the main axes x and y is feasible. Projection of the correction wavefront into Zernike basis yielded the weights 0.9λ for Z_4 and 2.2λ for Z_5, and using these weights to generate the correction wavefront without including defocus yields the wavefront in the left panel of Fig. 3.11(f).

To illustrate better the phase stabilization procedures performed along oblique axes, Figure 3.12 shows phase views of *en face* and cross-sectional oblique planes of the original tomogram [Figs. 3.12(a) and (d)], after correcting phase noise along x' [Figs. 3.12(b) and (e)] and along y' [Figs. 3.12(c) and (f)]. In the original phase images, 2D phase instability is clear. Instead, the *en face* views after correcting phase noise exhibit 1D phase stability along the oblique axis that was corrected. The

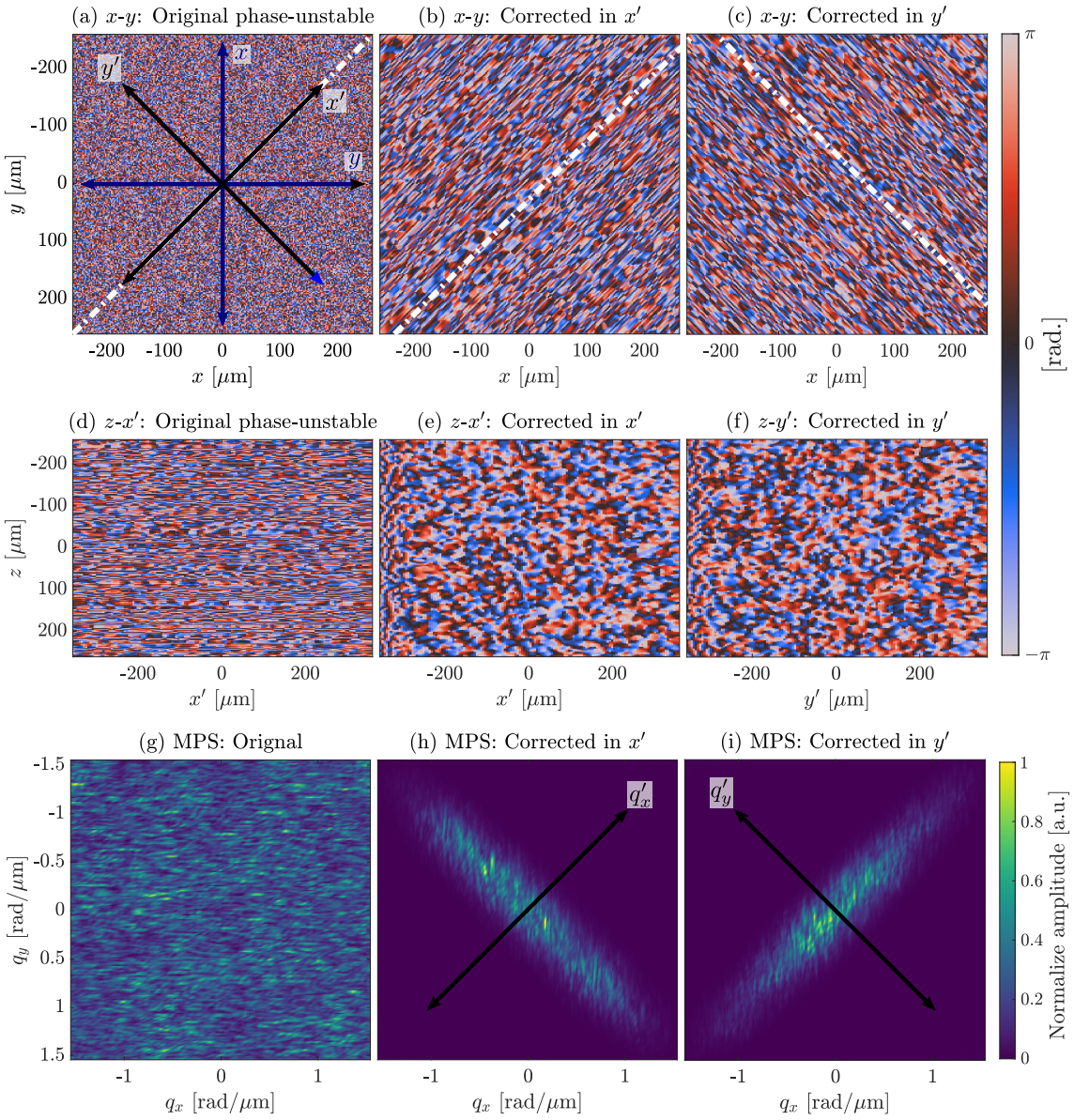

Figure 3.12: Testing phase stabilization along oblique axes for a simulated OCT tomogram. *En face* views of tomograms; (a) original, (b) corrected in x' and (c) corrected in y'. Oblique cross-sections z-x'; (d) original and (e) corrected in x'. (f) Oblique cross-sections z-y' corrected in y'. MPS of tomograms; (g) original, (h) corrected in x' and (i) corrected in y'. Note that axes in the MPS maps are q_x, q_y and not $q_{x'}$, $q_{y'}$.

oblique-planes images in Figs. 3.12(d)-(f), which correspond to the path marked by the white lines on the *en faces*, exhibit phase stability as expected. Interestingly, the analysis on the MPS [see Figs. 3.12(g)-(i)] is yet valid for this case, only that the axis along which the MPS displays a Gaussian profile is now rotated, depending on the corrected oblique axis.

3.3.4. SHARP in polarization-sensitive OCT

The operation of CAC techniques so far has been described for intensity images used for structural contrast, however, in functional extensions of OCT, the effects of aberrations in the acquired complex signal are also transferred through the post-processing methods used for calculating additional useful information of the sample. Such is the case of polarization-sensitive (PS-)OCT, which is used for the measurement of polarimetric properties of tissue [42, 174]. PS-OCT has great clinical interest due to its sensitivity to fibrillar tissue and its organization, and is used in intravascular OCT [175], retinal imaging [40, 176], anterior segment [177], among others.

Adaptive optics (AO) has been integrated into PS-OCT systems for aberration-free retinal imaging with improved effective lateral resolution [40], however, it is known that AO does not extend the depth of field, whereas numerical alternatives like ISAM or CAO are capable of extending the depth of field by correcting for the depth-dependent defocus. The phase stability requirement has hindered the adaptation of CAC techniques in many systems oriented to PS-OCT that may not satisfy the phase stability requirement. Apart from the work of Davis *et. al.* where they developed a vectorial description of ISAM for polarization-sensitive imaging [116, 129], CAC techniques have not been demonstrated in PS-OCT, and thus it is unclear whether the processing performed in such techniques affects negatively the PS-OCT processing.

Given that SHARP can operate with phase-unstable systems, its operation can be extended to PS-OCT systems, which often do not satisfy the phase stability requirement. In this section, a procedure to properly apply SHARP in PS-OCT taking into consideration the particularities of Stokes tomograms processing is presented. Because the theory and models used in PS-OCT are rather extensive and out of the scope of this work, only the sufficient information required to understand the operation of SHARP in PS-OCT is provided here, and detailed information if required by the reader can be explored in complementary bibliography [174, 178].

Overview of Stokes processing

In PS-OCT processing, briefly summarized in Figure 3.13, the polarimetric properties of the light backscattered by the sample are retrieved from a collection of several

polarization-diverse measurements. More specifically, the sample is illuminated using two polarization states $p = \{p_1, p_2\}$ orthogonal in the Poincaré sphere and the backscattered signal is measured by a polarization-diverse receiver with two orthogonal polarization channels $c = \{c_1, c_2\}$, for a total of four tomographic complex measurements $S_{p,c}(x, y, z)$. In standard Stokes processing for PS-OCT, these four complex measurements forming two Jones vectors are converted into two Jones-Stokes vectors $\mathbb{S} = [I, Q, U, V]^T$ composed of the four Stokes parameters. Polarimetric properties of the sample are estimated using the two Stokes vectors [174], being I the total intensity and Q, U and V quantities related to the degree of linear, oblique, and circular polarization, when properly normalized. Polarimetric properties retrieved in Stokes processing are the degree of polarization (DOP) and birefringence comprising phase retardation or retardance Δn and optic-axis orientation ψ.

Because of the coherent nature of the OCT signal, the Jones-Stokes vectors are affected by speckle which appears as strong noise in the subsequent calculation of polarimetric properties. For this reason, each Jones-Stokes parameter is spatially averaged, typically using a Gaussian kernel, to produce incoherent Stokes parameters $\bar{\mathbb{S}} = [\bar{I}, \bar{Q}, \bar{U}, \bar{V}]^T$ with reduced speckle resulting in polarimetric properties with reduced noise. However, a resolution loss is associated with this spatial average, which in combination with aberrations has imposed a relatively coarse lateral resolution in PS-OCT imaging [40], making it difficult to obtain highly-localized measurements of polarimetric properties of tissue which may be of great interest [40, 177].

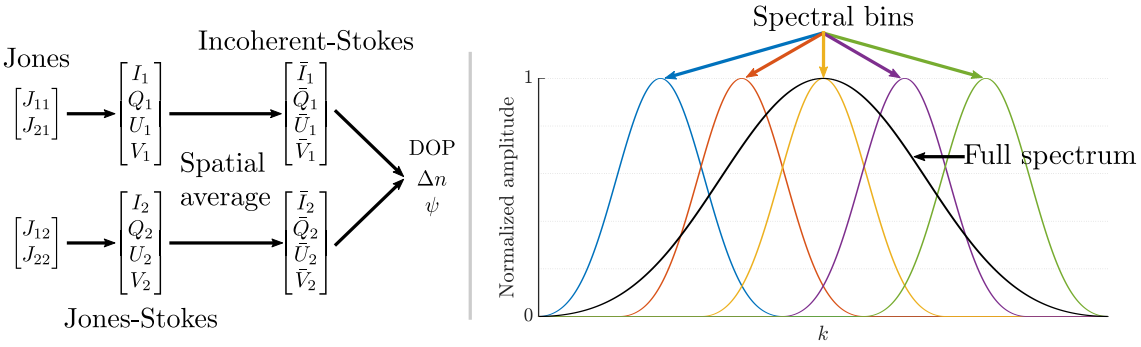

Figure 3.13: Overview of Stokes processing for PS-OCT and spectral binning.

In certain PS-OCT systems, fiber-based components induce wavelength-dependent changes on the polarization state of light that prevent to obtain reliable information from the acquired signals $S_{p,c}(x, y, z)$ directly [174]. Spectral binning processing has been proposed to overcome this issue [178], in which the acquired spectral signals $S_{p,c}(x, y; k)$ are split in k-space into several bins covering smaller portions of the bandwidth, as depicted in Fig. 3.13, such that wavelength-dependent effect of the system is made more constant within each spectral bin since they have a narrower bandwidth than the original spectrum. Then, PS-OCT processing is performed independently for each reduced-bandwidth tomogram, with additional steps based

on vectorial analysis to align the estimated polarimetric properties into a single estimation comprising the information of the entire original spectrum [178]. There is an additional resolution loss in spectral binning processing, but this time in the axial direction only, because the bandwidth of each spectral bin is narrower than the original spectrum, resulting in a coarser axial resolution.

Polarization-sensitive SHARP

Given that aberration correction operates on the complex field, SHARP must be applied to the four complex tomograms $S_{p,c}$ before conversion to Stokes parameters which are intensity values. Particularities of the process are following explained, but first, it should be clarified that the goal here is to correct non-polarizing aberrations, which are different to polarization aberrations that include changes in the polarization state of light associated with ray paths through optical systems [179].

The determination of the optimal weights for CAO from individual spectral bins tends to be ineffective since each spectral bin has a reduced axial resolution and different amount of signal-to-noise ratio. Therefore, the tomogram with the full spectral bandwidth of the system is employed to determine the optimal weights rather than finding the optimal weights for each spectral bin independently. The optimization procedure is performed only for a single polarization state p and the image sharpness metric is computed from the total intensity given by $|S_{p,c1}|^2 + |S_{p,c2}|^2$, assuming that aberrations are polarization-independent thus they are the same for both polarization states. Strictly speaking, polarizing media may induce undesired changes in wavefront that depend on the polarization state of light, but these changes generally contribute less than wavefront aberrations, even more with the magnitude of polarizing effects of tissue.

Phase offsets and slopes required for phase stabilization are determined also in the full-bandwidth tomogram but for the two polarization states p independently because phase noise is not necessarily the same for the two states. After determining phase noise correction (offsets and slopes) and the optimal weights for aberration correction using the full-bandwidth tomograms, these parameters are then applied to all spectral bins and input polarization states. To summarize, the operation of SHARP in PS-OCT consists of determining the parameters for phase noise and aberration correction in the full-bandwidth tomograms and then using those to correct each spectral bin independently. This is possible since the filter applied in CAO is k-independent and since phase noise correction operates on each A-line globally, therefore it does not change across spectral bins. Aberration-corrected complex tomograms $\tilde{S}_{p,c}$ for each spectral bin are then transformed into Stokes vectors followed by the subsequent steps in PS-OCT processing. The positive effect of CAO applied to the complex tomograms is translated into the Stokes parameters

and ultimately into the polarimetric properties.

3.4. Complex noise reduction: CTNode

High sensitivity of typically ∼100 dB is provided by OCT systems, meaning that backscattered light as weak as 10^{-10} times the reference mirror reflection can still be detected [55, 88]. Further improvements are possible with post-processing, and the most used approach is to average multiple repetitions frames to reduce noise, taking advantage of the high imaging speed provided by FDOCT that enables the acquisition of multiple repeated frames [56, 180]. Averaging can be either incoherent, i.e. using the intensity signal, or coherent, i.e. using the complex signal, but it has been found that coherent averaging is more efficient in improving the SNR in phase-stable data [56], whereas incoherent averaging is mostly used for speckle reduction. Although frame averaging has been effective to increase SNR of OCT images for improved visualization and diagnosis [181], it demands the acquisition of multiple frames which is unpractical in certain scenarios, especially in volumetric imaging given a large amount of data, the significant increase in acquisition time, and the susceptibility to be negatively affected by motion artifacts.

Analyzing and addressing noise in the complex signal is advantageous for phase-dependent post-processing techniques [57]. In particular, in CAC there is an explicit interest in improving SNR because aberrations produce a significant reduction of signal collection, and as a consequence, acquired images have a reduced dynamic range that is not expanded by aberration correction. The optimum amplitude filter integrated into SHARP is a straightforward tool to address noise and although its performance could be improved through oversampling, its effectiveness is limited especially when sampling approaches Nyquist limit.

In this section, a statistical approach for noise reduction is proposed as an alternative to current strategies, in which the 2D or volumetric information of the tomogram is exploited to reduce noise with no need for frames repetitions. The framework of this proposal is based on the previously developed technique **T**omographic **NO**n-local means **de**speckling (TNode) that suppresses speckle on the intensity while preserving resolution [53], except that here the aim is to denoise the complex signal thus the new proposal is called **C**oherent **T**omographic **NO**n-local means **de**noising (CTNode). A description of CTNode is provided below.

3.4.1. Non-local means

Non-local means has been used widely in image processing in several fields [182–185] as it outperforms traditional averaging in resolution preservation. The core idea

behind non-local means is to perform a spatial average using an adaptive kernel defined explicit for each pixel of the image using the information of neighboring pixels [53]. To define the weights of the kernel used to filter a target pixel, a statistical metric is used to determine how similar are each neighboring pixel to the target pixel. Defining the acquired noisy tomogram as $S_N(\boldsymbol{r})$ with $\boldsymbol{r}$ being a 3D vector representing the three coordinates $\boldsymbol{r} = (x, y, z)$, the weighted estimation $\hat{S}(\boldsymbol{r})$ of the noiseless signal $S(\boldsymbol{r})$ is computed as

$$\hat{S}(\mathbf{r}) = \frac{\sum_{\boldsymbol{r}' \in \boldsymbol{\nu}} w(\boldsymbol{r}, \boldsymbol{r}') S_N(\boldsymbol{r}')}{\sum_{\boldsymbol{r}' \in \boldsymbol{\nu}} w(\boldsymbol{r}, \boldsymbol{r}')}, \tag{3.21}$$

where $w(\boldsymbol{r}, \boldsymbol{r}')$ are the weights of target pixel $\boldsymbol{r}$ with respect to all neighbor pixels $\boldsymbol{r}'$ inside a search window $\boldsymbol{\nu}$. The search window $\boldsymbol{\nu}$ is a collection of pixels centered at $\boldsymbol{r}$ with sizes (ν_x, ν_y, ν_z) for a total size of $V = (2\nu_x + 1) \times (2\nu_y + 1) \times (2\nu_z + 1)$ that defines the spatial extension of the filtering kernel. In other words, the search window controls how many pixels are included in the weighted average of the target pixel. The following step is to find a proper definition of $w(\boldsymbol{r}, \boldsymbol{r}')$ based on statistical properties of noise in order to produce an appropriate filtering.

3.4.2. Derivation of weights for noise reduction

Noise in FDOCT is originated in the acquisition of the spectral fringes under an additive model, allowing to express the measured noisy signal in k-space as $s_n(x, y, k) = s(x, y, k) + n(x, y, k)$ where $s(x, y, k)$ is the true noiseless signal and $n(x, y, z)$ is the randomly distributed noise. After Fourier transform of the spectral fringes used to compute the depth-dependent signal $S_N(x, y, k)$, noise still follows an additive model since

$$\begin{aligned} \mathrm{FT}_k\{s_n(x, y, k)\} &= \mathrm{FT}_k\{s(x, y, k)\} + \mathrm{FT}_k\{n(x, y, k)\} \\ S_N(\mathbf{r}) &= S(\mathbf{r}) + N(\mathbf{r}), \end{aligned} \tag{3.22}$$

where $S(\mathbf{r})$ is the true noiseless depth-dependent signal and $N(\mathbf{r})$ the additive noise, setting $\mathbf{r} = (x, y, z)$ for simplicity as before. The task is therefore to cancel out the contribution of noise. It has been shown that noise in OCT follows a zero-mean complex Gaussian distribution with equal standard deviation σ_N on both the real and imaginary parts [57, 186]. Analyzing only the real part of the signal $R_N = \mathrm{Re}\{S_N\}$ by now, the probability of measuring a realization R_N given a true value $R = \mathrm{Re}\{S\}$

and the standard deviation σ_N of noise is [187]

$$\mathcal{P}(R_N|R,\sigma_N) = \frac{1}{\sqrt{2\pi}\sigma_N}\exp\left\{-\frac{(R_N-R)^2}{2\sigma_N^2}\right\}, \tag{3.23}$$

and similarly for the imaginary part $I_N = \mathrm{Im}\{S_N\}$.

Now, to determine the similarity between a pair of values $R_N(\boldsymbol{r})$ and $R_N(\boldsymbol{r}')$ in CTNode, a similarity criterion is defined using the likelihood-ratio test (LRT),

$$\mathcal{L}\{R_N(\boldsymbol{r}), R(\boldsymbol{r})\} = \frac{\mathcal{P}[R_N(\boldsymbol{r})|R(\boldsymbol{r},\boldsymbol{r}'),\sigma_N]\mathcal{P}[R_N(\boldsymbol{r}')|R(\boldsymbol{r},\boldsymbol{r}'),\sigma_N]}{\mathcal{P}[R_N(\boldsymbol{r})|R(\boldsymbol{r}),\sigma_N]\mathcal{P}[R_N(\boldsymbol{r}')|R(\boldsymbol{r}'),\sigma_N]}, \tag{3.24}$$

which evaluates the probability that the underlying noiseless parameters $R(\boldsymbol{r})$ and $R(\boldsymbol{r}')$ are different between them or equal to a common parameter $R(\boldsymbol{r},\boldsymbol{r}')$. More specifically, the numerator of the LRT is the probability of the two values $R_N(\boldsymbol{r})$ and $R_N(\boldsymbol{r}')$ being different realizations of the same distribution, in which case the similarly is high and the numerator tends to one, while the denominator is the probability of the two values $R_N(\boldsymbol{r})$ and $R_N(\boldsymbol{r}')$ being realizations of different distributions, in which case the similarity is small. In consequence, the LRT tends to one when the two pixels being compared are likely similar and to zero when they are dissimilar. The standard deviation of noise is assumed equal in all probabilities given that σ_N tends to be constant over the entire tomogram.

In practice, the underlying parameters are in general unknown and the LRT cannot be computed directly, therefore it is replaced by the generalized likelihood ratio (GLR) $\mathcal{L}_G$ [53] where the parameters are changed by their maximum likelihood estimates [187], enabling to obtain a closed-form expression given by

$$\mathcal{L}_G\{R_N(\boldsymbol{r}), R_N(\boldsymbol{r}')\} = \exp\left\{-\frac{[R_N(\boldsymbol{r})-R_N(\boldsymbol{r}')]^2}{4\sigma_N^2}\right\}, \tag{3.25}$$

for the case of the Gaussian distribution of Eq. (3.23). The GLR in Eq,(3.25) was derived using the real part of the signal, but the expression for the imaginary part is equivalent.

The probability of the real and imaginary parts must be compounded in order to avoid corruptions in the phase due to dissimilar filtering. This compounding imposes the condition that two pixels are similar only when the real *and* imaginary parts are

similar. Hence, the GLR for the complex signal $\mathcal{L}_C$ is

$$\begin{aligned}\mathcal{L}_C\left\{S_N(\boldsymbol{r}), S_N(\boldsymbol{r}')\right\} &= \exp\left\{-\frac{[R_N(\boldsymbol{r}) - R_N(\boldsymbol{r}')]^2}{4\sigma_N^2}\right\}\exp\left\{-\frac{[I_N(\boldsymbol{r}) - I_N(\boldsymbol{r}')]^2}{4\sigma_N^2}\right\} \\ &= \exp\left\{-\frac{[R_N(\boldsymbol{r}) - R_N(\boldsymbol{r}')]^2 + [I_N(\boldsymbol{r}) - I_N(\boldsymbol{r}')]^2}{4\sigma_N^2}\right\} \\ &= \exp\left\{-\frac{|S_N(\boldsymbol{r}) - S_N(\boldsymbol{r}')|^2}{4\sigma_N^2}\right\},\end{aligned} \tag{3.26}$$

where the property of complex numbers $|\mathcal{Z}|^2 = \mathrm{Re}\left\{\mathcal{Z}\right\}^2 + \mathrm{Im}\left\{\mathcal{Z}\right\}^2$ was employed. $\mathcal{L}_C$ depends only in the two observed values $S_N(\boldsymbol{r})$, $S_N(\boldsymbol{r}')$ and the standard deviation of noise that can be estimated experimentally.

The GLR is a point-wise estimation but comparing patches of pixels around the two pixels of interest could yield a more robust estimation. Similarity between patches $\mathcal{L}_P$ is calculated by computing the point-wise similarity between corresponding pixels of the patches and then compounding the logarithmic probabilities as

$$\mathcal{L}_P\left\{S_N(\boldsymbol{r}), S(\boldsymbol{r}')\right\} = \sum_{\boldsymbol{\tau}\in\boldsymbol{p}} \log\{\mathcal{L}_C[S_N(\boldsymbol{r}+\boldsymbol{\tau}), S_N(\boldsymbol{r}'+\boldsymbol{\tau})]\}, \tag{3.27}$$

where $\boldsymbol{p}$ is a collection of 3D shifts such that $\boldsymbol{r}+\boldsymbol{\tau}$ and $\boldsymbol{r}'+\boldsymbol{\tau}$ span the pixels in the patches around $\boldsymbol{r}$ and $\boldsymbol{r}'$, respectively, which form a similarity window of sizes (p_x, p_y, p_z) and total size $P = (2p_x+1)\times(2p_y+1)\times(2p_z+1)$.

Finally, the expression for the weights in Eq. (3.21) is

$$w(\boldsymbol{r}, \boldsymbol{r}') = \exp\left[\frac{\mathcal{L}_P\left\{S_N(\boldsymbol{r}), S_N(\boldsymbol{r}')\right\}}{h}\right], \tag{3.28}$$

where an additional parameter $h > 0$ is introduced to modify the distribution of weights and control the overall filtering. Additionally, because the weight of the self-similarity $w(\boldsymbol{r}, \boldsymbol{r}')$ is significantly larger than any other weight, it is replaced by the maximum similarity found in the patch to obtain a better performance [53].

To summarize, to estimate the noiseless value of each pixel, CTNode performs a non-local means around a search window centered in the target pixel, using weights calculated based on the similarity between pixels inside a similarity window. This is depicted for two patches in Figure 3.14 in a 2D arrangement, although 3D similarity and search windows can be used, depending on the information available.

The purpose of CTNode in the context of this work is to complement SHARP to increase the dynamic range of aberration-corrected images. The reduction of complex

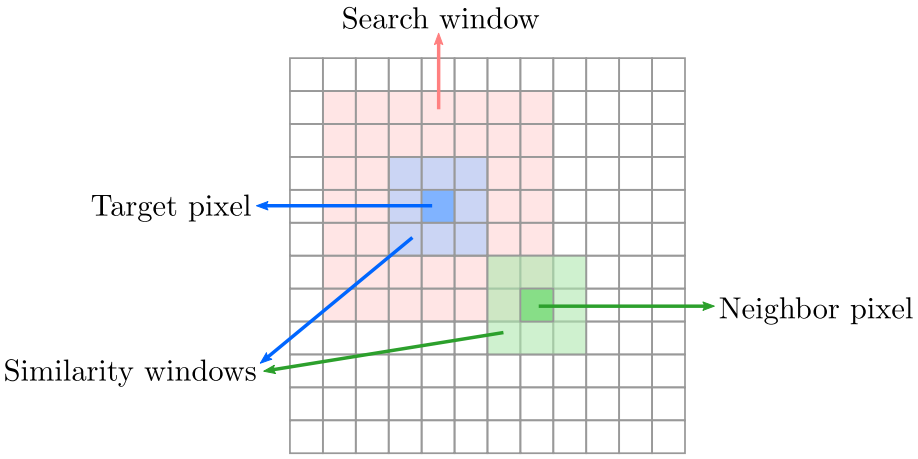

Figure 3.14: Illustration of the operation of non-local means using search window of size 7×7 and similarity window of size 3×3.

noise could benefit the subsequent operation of SHARP improving the procedure of optimizing image quality in CAO steps in regions with low SNR. Furthermore, there is a wide variety of applications yet to explore where CTNode could also be beneficial, in particular in phase-dependent or complex signal-based techniques like angiography [186], flowmetry [188], and elastography [189]. In such techniques, sensitivity is greatly influenced by noise level thus pre-processing the complex signal with CTNode could boost the subsequent performance of these techniques, with no need of acquiring multiple repetitions frames as demanded in traditional averaging.

3.4.3. Evaluation of CTNode in simulated OCT signal

To evaluate CTNode, it is desirable to have a noise-free reference but it is in principle impossible to achieve experimentally, therefore, the noise-free simulated OCT tomogram used previously was employed for this purpose. Figure 3.15 shows a selected B-scan from the original tomogram in Fig. 3.15(a), showing the cross-section of the bright-intensity cylindrical objects, immersed in the low-intensity and nearly homogeneous medium that constitutes the tomogram. Synthetic zero-mean Gaussian noise was added to the real and imaginary parts of the noiseless simulated tomogram with a constant variance of σ_N^2 over the entire tomogram, as illustrated with the noisy B-scan of Fig. 3.15(b). There is a signal decay over depth in the original tomogram emulating light absorption, although it may not be clear in Fig. 3.15(a). This signal decay causes a variation of SNR despite σ_N being constant, as can be appreciated in the logarithmic-SNR map shown in Fig. 3.15(c), where a threshold was used to display only values greater than -3 dB, corresponding to 0.5 in linear scale, which means that the signal level is half the noise variance, hence signal is masked by noise. A limit for the SNR of the minimum detectable signal is 0 dB (1 in linear scale), indicating that the signal level is equal to the noise variance.

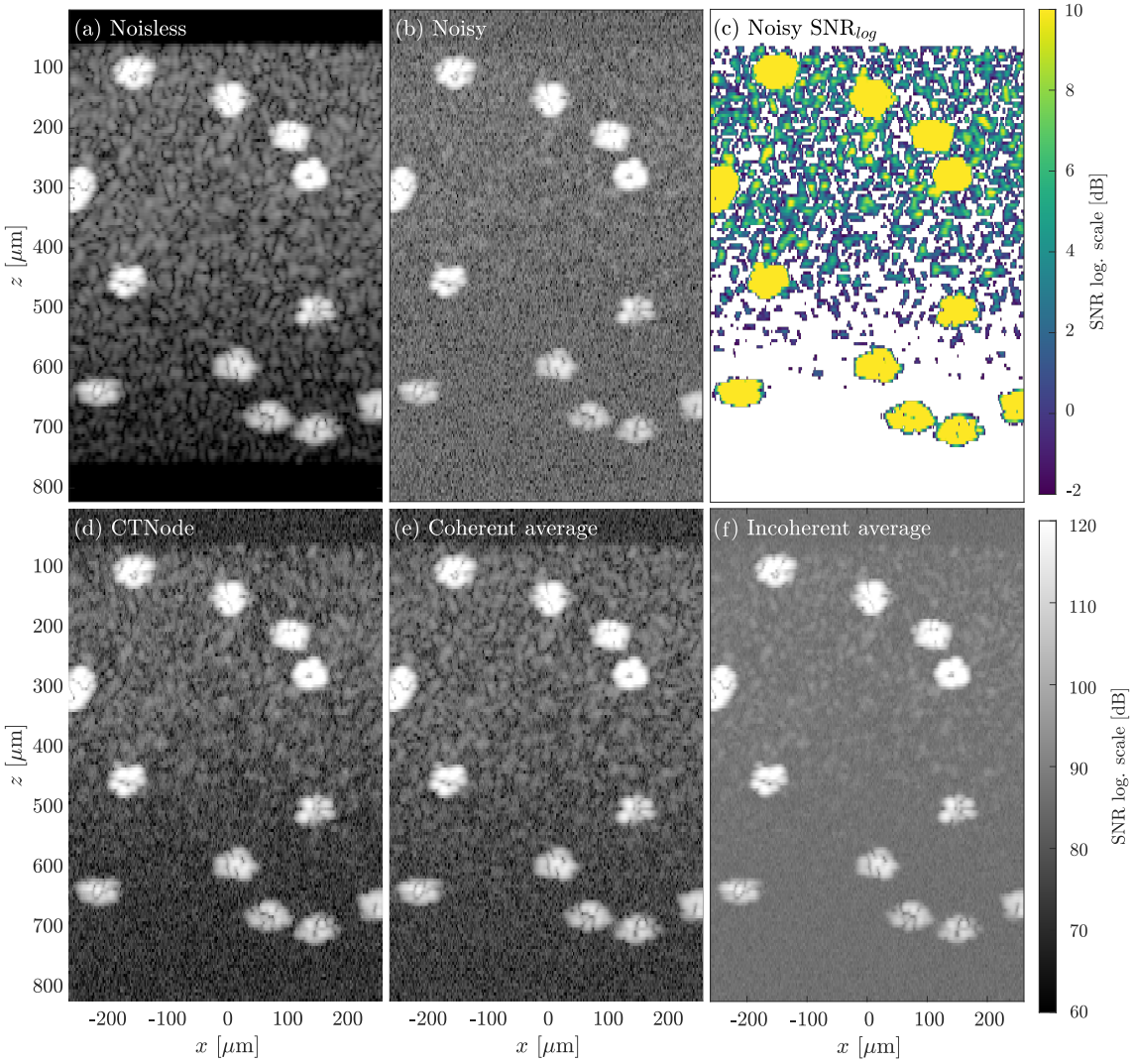

Figure 3.15: Evaluating the performance of CTNode in a simulated OCT tomogram. Intensity B-scan planes: (a) Original noise-free (b) noisy with zero-mean Gaussian noise, (d) after CTNode, after (e) coherent, and (f) incoherent averaging. (c) Logarithmic SNR for B-scan in (b) threshold to show only values > -3 dB.

Then, CTNode was applied to the noisy tomogram. It was found that the use of large search and similarity windows yields strong noise reduction but at the cost of degrading resolution because the filtering kernel is large and prone to smear information. Conversely, the resolution is better preserved by using small windows but filtering efficiency is reduced. Furthermore, a large value of h is desired for an efficient noise reduction but it causes strong filtering of high SNR pixels which are expected to be slightly filtered since the effect of noise is not significant. These observations are expected from the general operation of non-local means algorithm and in particular from the operation of TNode for speckle suppression [53]. Parameters were iteratively tuned by visual inspection of results seeking for an optimal trade-off between the thee competing aspects: efficient noise reduction, resolution preservation, and avoidance

of corruption of pixels with high SNR, resulting in a search window of 15×15×15, a similarity window of 3×3×3 and a filtering parameter $h = 0.10$. Processing time was about 8 seconds per B-scan of size 160×256 px^2, in a workstation computer running on an Intel Core i7-8700 processor @ 3.2GHz, using a GPU-based implementation in MATLAB 2019a running on a 6 GB GPU NVIDIA P4000.

For comparison, images using coherent and incoherent frames averaging were also computed. The set of repetition frames was created by replicating the noiseless B-scan, then adding synthetic noise to each repetition with the same variance, and finally computing the arithmetic mean of the complex signal for coherent averaging and the intensity signal for incoherent averaging. It is known that coherent averaging of N frames produces a reduction of noise variance by a factor of $1/N$ whereas incoherent averaging only of $1/\sqrt{N}$, however, coherent averaging also reduces signal level resulting in a less SNR improvement than expected, although it is still higher than improvement achieved by incoherent averaging [56]. For this test, N was set to 12, a value at which coherent averaging performed similarly to CTNode.

Fig. 3.15(d)-(e) shows the noisy B-scan after CTNode, coherent and incoherent averaging, respectively. There is not any signal degradation after CTNode suggesting that its application to the tomogram did not produce any detrimental effect in signal quality, and indeed there is a clear overall reduction of noise level as expected, compared to noisy B-scan. For the following analysis, two regimes can be identified, one where SNR is below 0 dB and the other where SNR is above 0 dB. For SNR > 0, CTNode and coherent averaging recovered the underlying signal at an acceptable level, allowing to visually distinguish the speckle pattern from the noise, and in particular, the upper dark band can be distinguished from the object information. For incoherent averaging, the speckle pattern is also visually perceptible but the contrast is greatly reduced because in this approach the noise floor level is not reduced, only the noise variance, contrary to coherent average where both, the noise mean and noise variance are reduced [56]. In all cases, the bight intensity structures appear unchanged, as is expected given that noise reduction is less significant when SNR is high. For this reason, noise reduction is intended to improve contrast in regions with SNR approaching zero, whereas in regions with high SNR it is unlikely necessary because the contribution of noise is unimportant.

For SNR < 0 dB, it can be observed that despite the noise reduction, underlying signal information is lost in all filtering approaches, since in this regime the mean intensity signal is below the noise variance and therefore underlying true signal cannot be distinguishable from noise. It is possible to increase negative SNRs values using coherent average and for this case, it was achieved at $N = 100$ which is a relatively large and possibly unpractical amount.

The relevance of complex noise reduction is not only evident in intensity images in

terms of contrast improvement but also in phase information that is very sensitive to noise. Figure 3.16 shows phase images of the B-scan plane used for Fig. 3.15, of the original and noisy tomogram in Figs. 3.16(a) and (b). The speckle pattern is directly visualized in noiseless phase B-scan, whereas noisy phase shows regions dominated by noise, and even in the high SNR regions noise is perceptible, making it difficult to visualize the speckle pattern. Phase B-scans after CTNode and coherent averaging are shown in Fig. 3.16(c) and (d), respectively, and both exhibit a reduction of noise in high and low SNR regimes, partially recovering the speckle pattern lost in low SNR regions and improving visualization of high SNR regions.

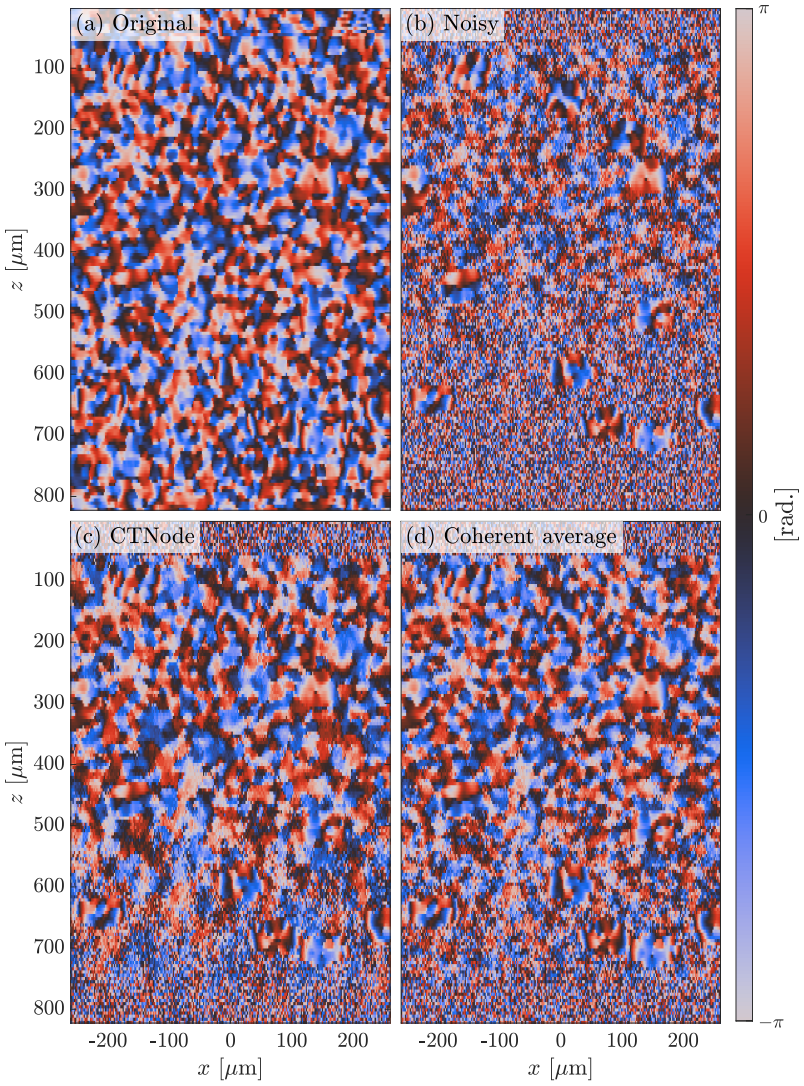

Figure 3.16: Evaluating the reduction of Gaussian noise in phase information with CTNode in a simulated OCT tomogram. B-scan phase images: (a) Original noise-free, (b) noisy with zero-mean Gaussian noise, and then filtered (c) with CTNode and (d) with coherent wavering.

Although with the current implementation of CTNode it appears to be unfeasible to filter pixels with negative SNRs to recover the underlying signal properly, it is

clear that CTNode outperforms coherent averaging in the sense that it required a single repetition to obtain a similar result of averaging 12 repetitions. This is possible given that CTNode (and non-local means in general) efficiently exploits the available information. It is expectable that the extension of CTNode to operate with multiple frame repetitions, like it is possible with TNode currently, could boost its operation even more compared to arithmetic frame averaging. Anyhow, the possibility to efficiently reduce complex noise with a single acquisition is attractive for phase-dependent techniques where multiple repetitions of frames are not practical given its specific acquisition scenarios [57].

CHAPTER 4

EXPERIMENTAL APPLICATIONS

In the previous chapter, the SHARP technique was explained in detail, including additional steps and modifications to address specific issues encountered in certain situations, as well as a proof of concept validation using a straightforward to image sample with prominent structures, convenient to readily visualize and verify computational refocusing. Also, the CTNode technique was described and evaluated with a simulated tomogram. In this chapter, the experimental operation of SHARP is demonstrated with samples with medical relevance including *ex vivo* and *in vivo* imaging, to show the potential of SHARP to improve the quality of OCT tomograms to provide more detailed information of tissue and to facilitate visualization of images and to improve analysis of specialists, more importantly in intensity-based imaging but in polarization-sensitive imaging as well. Additionally, the experimental application of SHARP is complemented with the previously developed technique TNode and the new proposal CTNode, to provide a more significant improvement of image visualization.

First experimental demonstration is presented in anterior segment imaging of an excised swine eye, where SHARP is complemented with TNode and CTNode independently. Anterior segment imaging is an application with great relevance in OCT given that it possesses structures with fundamental roles for vision, including cornea, limbus, iris, sclera, among others. An additional demonstration of the performance of CTNode is then presented in the human retina *in vivo*, independently of SHARP. The second demonstration of SHARP is presented in catheter-based imaging, which is the second-largest imaging modality in OCT after ophthalmic-OCT, using a dataset from the airway of a swine acquired *in vivo*. An additional *in vivo* demonstration is showed in skin imaging of human hand dorsal where involuntary sample motion arising from pulse heartbeat and respiration must be corrected. Finally, the operation of SHARP in polarization-sensitive OCT is demonstrated in the limbal region of an excised swine eye, showing computational refocusing of polarimetric parameters.

The experimental datasets of the anterior segment and human skin were acquired with the bench-top system used for the proof of concept experiment, varying in some cases the scan lens and sampling configuration accordingly. The endoscopic dataset was provided by NinePoint Medical. The human retina dataset was acquired with a bench-top retinal SSOCT system integrated into a modified commercial ophthalmic interface [190]. Relevant parameters used in each experiment are described in the corresponding section.

4.1. Anterior segment imaging *ex vivo*

The eyeball is in general divided into two main sections for its study; the anterior segment depicted in Figure 4.1 and the posterior segment. The former is primarily responsible for light collection and image formation by the cornea and the lens, and there are additional functional structures that support the normal operation of the eye, including the iris, sclera, and ciliary body. OCT systems for anterior segment imaging typically have a large depth of field of ∼3 mm to provide focused images across the entire axial extent of the anterior segment that is relatively large, but this implies a coarse lateral resolution. In some cases, the local structure of specific tissue is desired, for instance, in the study of corneal layers thickness and stroma arrangement [191], achievable using high-resolution systems at the cost of having a relatively short depth of field.

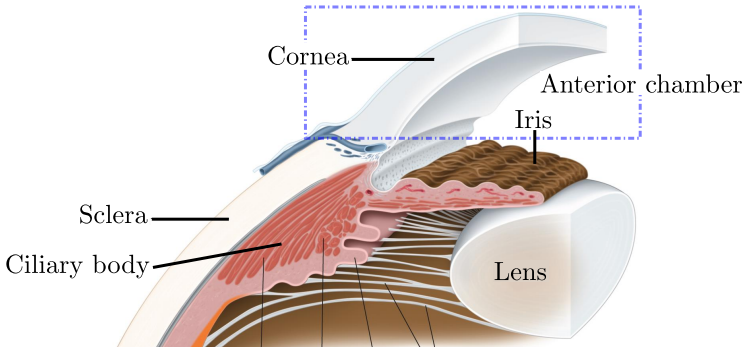

Figure 4.1: Illustration of anterior segment anatomy. [Adapted from © 2020 American Academy of Ophthalmology].

Computational refocusing has the potential to extend the depth of field in anterior segment imaging to provide images with a high lateral resolution in an extended depth covering a larger axial range of anterior segment [192]. As an initial experimental demonstration, the SSOCT system used in the proof of concept experiment previously described was used to image the anterior segment of an excised swine eye, emphasizing in the cornea, around a region similar to that enclosed by the blue rectangle in Fig. 4.1. From the measured tomogram, an ROI was selected consisting of 700

samples per A-line, 768 A-lines per B-scan, and 256 B-scans, and covering a lateral field of view of 6×2 mm^2 in an axial ranging of 4 mm in air. Two datasets were acquired; a reference tomogram with the focal plane located at the paracentral zone of the cornea, and an OoF tomogram with the focal plane located at the iris, not visualized in the selected ROI. Figure 4.2(a) shows a B-scan of the original tomogram where defocus is evident in all the corneal layers and structures inside the stroma. Due to the confocal gating, there is a drop in signal-to-noise ratio (SNR) due to the large offset from the focal plane, observed as a low contrast between signal level in corneal tissue and noise floor level in regions having no signal from tissue.

Standard SHARP procedure was applied to the OoF tomogram, using Legendre polynomials P_2, P_3, P_4, and P_5. The correction weights in y were set equal to those found in x given that the optimization procedure in y was prone to fail at certain planes, possibly because there is not enough signal information for a robust estimation of the image quality metric, since the FoV in y is small and the structures are oriented toward the y axis. Fig. 4.2(b) shows that using the optimum filter $[\tilde{\Omega}(q_x, q_y)]$ alone (i.e. setting phase filter $\tilde{\varphi}$ to zero) is very effective at reducing noise in this particular case where SNR in intrinsically low, achieving a floor noise reduction of ∼6 dB, which improves overall contrast. However, optimum filter alone does not improve the blur, contrary to Fig. 4.2(c) that shows that after applying SHARP structures appear both sharper and with better contrast. Image improvement with SHARP can be observed in the fibrilar structure in the stroma, but the presence of speckle hinders visualization and assessment as noted when comparing insets in Figs. 4.2(a)-(c). For this reason, images were despeckled with TNode technique, known to preserve resolution and improve image contrast [53], to facilitate visual inspection and assessment, using similarity and search windows of 5×5×5 and 15×15×15 pixels ($z \times x \times y$) respectively, and filtering parameters $h_0 = 0.035$ and $h_1 = 0.010$. B-scans of the original and SHARP tomograms are shown in Figs. 4.2(d) and (e) after despeckling with TNode, where successful refocusing is distinguishable in SHARP image, which approaches the image quality of the despeckled reference B-scan in Fig. 4.2(f), being the loss in signal strength the major difference and a significant drawback in CAC.

Figures 4.2(g)–(o) show three despeckled *en face* views of the original, SHARP and reference tomograms at three depths indicated by lines in Figs. 4.2(d)–(f). The dynamic range of each *en face* view was adjusted to equalize the contrast for visual comparison. Blurring increases towards the cornea apex in the original views in Figs. 4.2(g)–(i). In contrast, SHARP views [Figs. 4.2(j)–(l)] have perceptually very similar resolution at all depths, enabling improved visualization of structures inside the stroma and clearer boundaries of the corneal epithelium, resembling reference images Figs. 4.2(o)–(m). These results show that SHARP could enable the examination of the iris and the full cornea in a single-shot acquisition with higher lateral resolution than currently possible, facilitating the accurate determination of

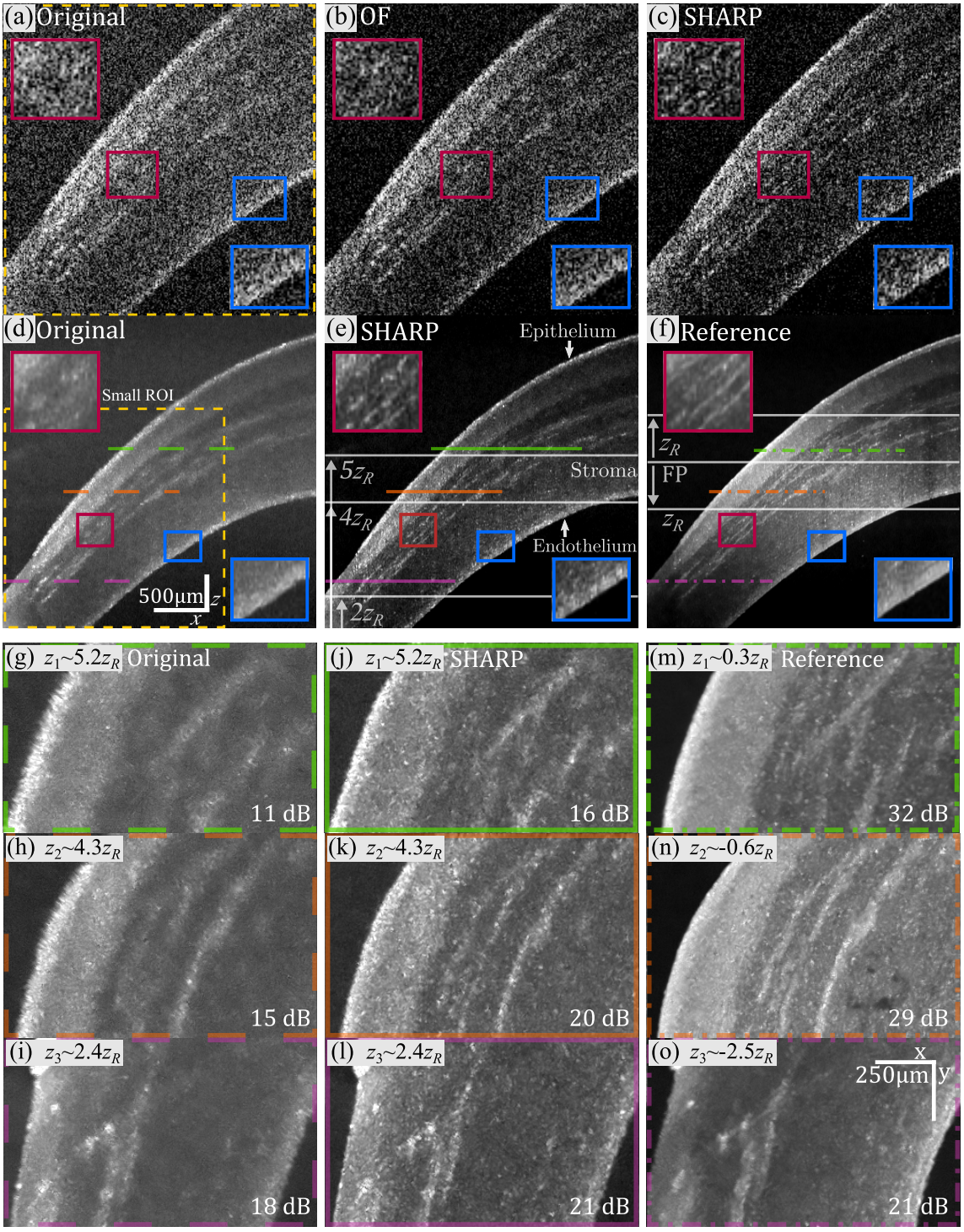

Figure 4.2: Application of SHARP in the anterior segment of an excised swine eye. Small ROI B-scans: (a) original, (b) optimum filter, and (c) SHARP. Full ROI B-scans after despeckling with TNode: (d) original, (e) SHARP, and (f) reference (FP: focal plane, in (a)–(e) FP is in the iris, out of image range). *En face* at depths z_i marked with lines in the B-scans: (g)–(i) original, (j)–(l) SHARP and (m)–(o) reference. Each *en face* image shows its dynamic range.

parameters of clinical interest such as the stromal demarcation line and tissue layer thicknesses with existing OCT systems without regard to phase noise. Finally, the combination of SHARP and TNode provided a significant improvement of image quality compared to the original tomogram in terms of resolution improvement, noise reduction, and contrast.

4.1.1. CTNode in combination with SHARP

Back-scattering of the cornea is relatively low because its constitutive tissue is inherently translucent for functional purposes, making that cornea stroma generally exhibits low to medium SNR, even lower in the presence of aberrations. In the previous demonstration of SHARP, the optimum filter proved to be a key tool to improve visualization of results in terms of noise suppression, providing an extended dynamic range. The aim now is to combine SHARP with CTNode to further improve contrast by reducing noise floor level.

After applying SHARP to the tomogram of the previous demonstration, CTNode was applied using search and similarity windows of 11×11×11 and 3×3×3, respectively, and $h = 0.15$. Figure 4.3 shows a selected B-scan of the original tomogram, after SHARP and after subsequent CTNode. The upper value of the dynamic range of all images is the same but the lower limit was equalized to the noise floor level (μ_N) of each image, computed as the average intensity within the blue rectangles in Figs. 4.3(a)-(c), to match the visual contrast at the cost of having different dynamic ranges. More specifically, the original B-scan in Fig. 4.3(a) has a noise floor level of 56 dB and a dynamic range of 16 dB, in SHARP B-scan in Fig. 4.3(b) the noise floor was reduced by 6 dB, allowing to increase the dynamic range to 22 dB and after CTNode noise floor was additionally reduced by 5 dB, for a total reduction of 11 dB, allowing to increase the dynamic range to 27 dB.

Apart from the correction of defocus, the image after SHARP and CTNode presents an overall improvement in contrast of low- and medium-SNR regions, such as the regions enclosed in circles of Fig. 4.3(c) where the signal is more clearly visualized than in their counterparts in Figs. 4.3(a) and (b). A notable side effect is that contrast of high-intensity signal seems to be reduced, as a consequence of the asymmetric extension of dynamic range: the noise floor level is decreased but the signal strength is not increased, but in fact, it is technically impossible to increase signal strength computationally. Despite that, the beneficial effect of noise reduction is more significant, for instance, the corneal stroma presents a better contrast after CTNode than in the original image where stroma exhibits a signal just above the noise floor level because of its relative low back-scattering and the negative effect of aberrations. This suggests that CTNode has the potential to improve the visualization of tissue with low to medium SNR signal through noise reduction.

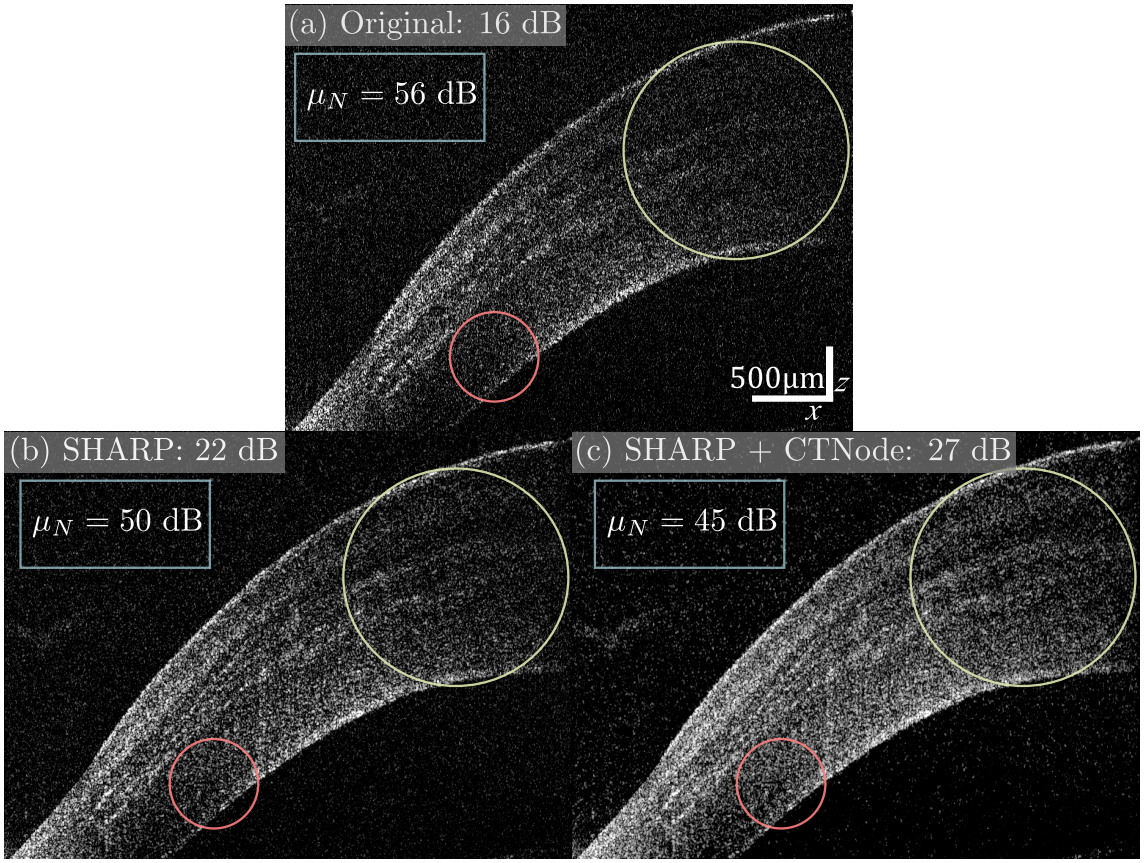

Figure 4.3: Combination of SHARP and CTNode in the anterior segment of an excised swine eye. B-scan images: (a) original, (b) after SHARP and (c) after subsequent CTNode. The number in the label of each image corresponds to its dynamic range.

Another important aspect is that no resolution loss was observed after CTNode, which is particularly relevant for SHARP given that it is desired to maintain the resolution improvement provided by the correction of aberrations.

4.1.2. Correction of anisotropic defocus in the cornea

The optical properties of tissue affect the propagation of the probe beam, and in particular, this may give rise to spatial variations of the focal position, which means that the focus does not follow a plane but a deformed surface, depending on sample geometry. The cornea possesses a curved surface and an index of refraction different to air. These features combined produce variations of focal position across the field of view following a smooth curvature, resulting in a *focal curve* rather than a focal plane. This phenomenon, encountered mainly in high-NA systems, demands spatially-varying aberrations correction.

To demonstrate the correction of anisotropic defocus in the cornea, the SSOCT

system was equipped with a scan lens producing an effective e^{-2} beam diameter of 9 μm in a Rayleigh range of 97 μm. The excised swine eye was imaged around the cornea apex, tilting the sample to avoid signal saturation due to specular reflection near to the apex, which ultimately resulted in an even greater spatial variation of the focal position. An ROI of 350 samples per A-lines, 1536 A-lines per B-scan, and 1024 B-scans was selected, covering a lateral field of view of 5×3.3 mm^2 in an axial ranging of 2 mm in air. It has been found that a better aberration correction is obtained if window-based CAO is applied after global CAO in each 1D aberration correction step, possibly because global correction serves as an initial estimation to aberration correction which is then improved locally with window-based correction. In this case, Legendre polynomial P_2 was employed, and, for window-based SHARP, the window size was set to 128×128 px^2 (0.4×0.4 mm^2).

Figure 4.4 shows an *en face* view of the original tomogram and after correction of aberrations with global and window-based SHARP. In this case, the optimum filter reduced noise floor level by 6 dB, but contrast improvement is not evident because the dynamic range of the original image in Fig. 4.4(a) was adjusted to match the contrast of the SHARP image in Fig. 4.4(b) for comparison purposes. Displayed *en face* planes are located at a depth within the corneal stroma, marked by the yellow line in original B-scan image in Fig. 4.4(c), presenting very dense signal but also

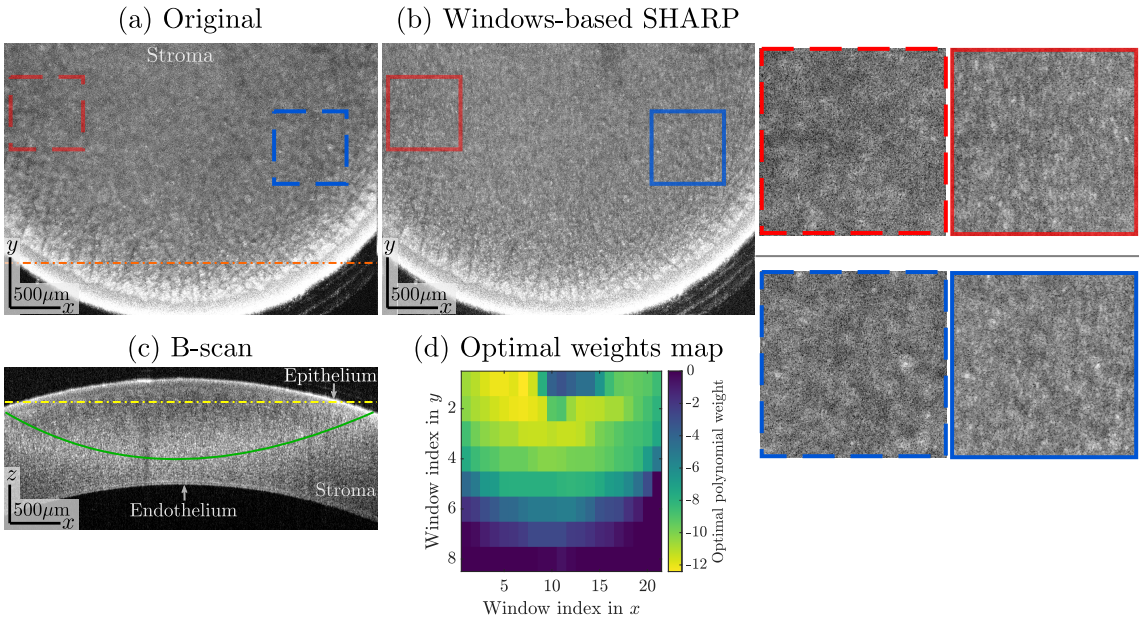

Figure 4.4: Application of SHARP in the cornea of an excised swine eye. *En face* views: (a) original and (b) after global and window-based SHARP, located at depth marked by the yellow dashed line in the original B-scan in (c), that at the same time corresponds to the location marked by orange dashed line in (a). (d) Two-dimensional map of optimal weights for all windows found for correction along x of *en face* plane in (b).

fine structures that are significantly blurred in the original tomogram, whereas after SHARP they appear sharper given the improvement of lateral resolution, as noted when comparing the insets that show zoomed regions of the images.

In practical terms, the depth of field can be often identified in cross-sectional views as a bright intensity band because the signal inside the depth of field is intrinsically stronger than outside. This way, it is possible to roughly determine the position of the focus as the center of this bright band. In the B-scan view of Fig. 4.4(c), the focus follows a curve instead of a plane, as marked by the green line, indicating that indeed the location of the focus varies with lateral position, resulting in a focal curve. This effect can be also inferred from the two-dimensional map in Fig. 4.4(d) that shows the optimal weights determined for each window for the *en face* plane in Fig. 4.4(b), which resemble the cornea curvature, instead of being constant across all windows as expected if the correction were purely global.

4.2. Complex noise reduction in human posterior segment imaging *in vivo*

The posterior segment of the eye is rich in structures that support the normal operation of the eye, such as the retinal nerve fiber layer, the photoreceptors layer, and the choroid [193]. In general, these structures present high back-scattering that varies between them allowing a readily visual identification in the intensity-contrast image. However, choroid and sclera typically present a lower signal, especially the sclera, given that they are at deep depths where signal strength is greatly affected by tissue absorption and the high reflectance of precedent layers like the retinal pigment epithelium. Measurement of the choroid thickness has been of great interest for diagnosis and study of pathologies [194], and this requires to identify the choroid/sclera (C/S) junction in order to reliable identify the choroid and measure its thickness, but this task is difficult given the relatively low contrast of the C/S junction.

Additional experimental validation of CTNode was performed, aiming to reduce noise in retinal imaging to improve the contrast of structures, including the C/S junction. The posterior segment of a healthy subject was imaged using a retinal system described in [190]. This SSOCT system is based on a VCSEL wavelength-swept source (Axsun Technologies, Inc., MA, USA) with an A-line repetition rate of 100 kHz and a spectral bandwidth of 91 nm centered at wavelength 1040 nm for an axial resolution of 10 μm in air. The system has a modified commercial ophthalmic interface (Heidelberg Engineering, Germany), that provides a diffraction-limited spot-size of 18 μm on the retina, with an integrated scanning laser ophthalmoscope (SLO) to track the motion of the subject's eye by analyzing motion-induced affine image

transformations compared to a pre-acquired reference SLO image, and then motion correction is translated to the control wave-forms of the galvanometers scanners of the SSOCT system on-the-fly, to follow eye motions during the acquisition. Additionally, a reference reflection in a separated arm of the sample arm is available for 2D phase stabilization.

The acquired tomogram consisted of 2048 depth samples, 1024 A-lines per B-scan, and 1024 B-scans, from which an ROI of 820×960×768 was extracted for processing. The phase was stabilized using the reference reflection [63]. Furthermore, a residual motion was observed despite the use of the motion tracking system, mostly slow-frequency motion, that was corrected using intra-B-scan bulk motion correction as described in Section 3.3.1. Phase stabilization and motion correction enabled the use of 3D search and similarity windows, which otherwise would be restricted to 2D or 3D with limited performance. CTNode was applied using search and similarity windows of size 15×15×15 and 3×3×3, respectively, and $h = 0.12$.

B-scan views of the original tomogram and after CTNode are shown in Figures 4.5(a) and (b), corresponding to the cross-section marked by red dashed lines in *en face* views shown in Figs 4.5(d) and (e). In the original image, the signal decays smoothly in the choroid making it difficult to identify the C/S junction. Application of CTNode provided a noise level reduction of 6 dB, allowing to increase the dynamic range of the image from 38 dB to 44 dB. This improvement is visualized in the medium-SNR layers in between the retinal nerve fiber layer and the photoreceptors layer that present a high contrast compared to noise floor level, but the contrast between layers seems to be reduced, due to the side-effect of CTNode mentioned before. Anyhow, the interest is not to visualize high-intensity layers, but in the signal in the choroid that is more clearly identified from the sclera which is masked by the noise level, and this could improve further determination of C/S junction.

The plot in Fig. 4.5 shows A-line profiles of the original and CTNode tomogram, at the location marked by the blue dashed lines in Figs. 4.5(a) and (b). The signal within the green line has high intensity, thus reduction of noise is inconsequential, but for low signal regions within the orange line, such as the sclera, noise reduction is perceived as a decrease in signal intensity. Finally, Figs. 4.5(d) and (e) show *en face* views of the original and CTNode tomograms at depths marked by the purple dashed lines in the B-scans. Signal around the optic disc is very homogeneous in the original *en face* because SNR is low and noise dominates, instead, CTNode *en face* view displays a transition in signal intensity from the choroid to the sclera.

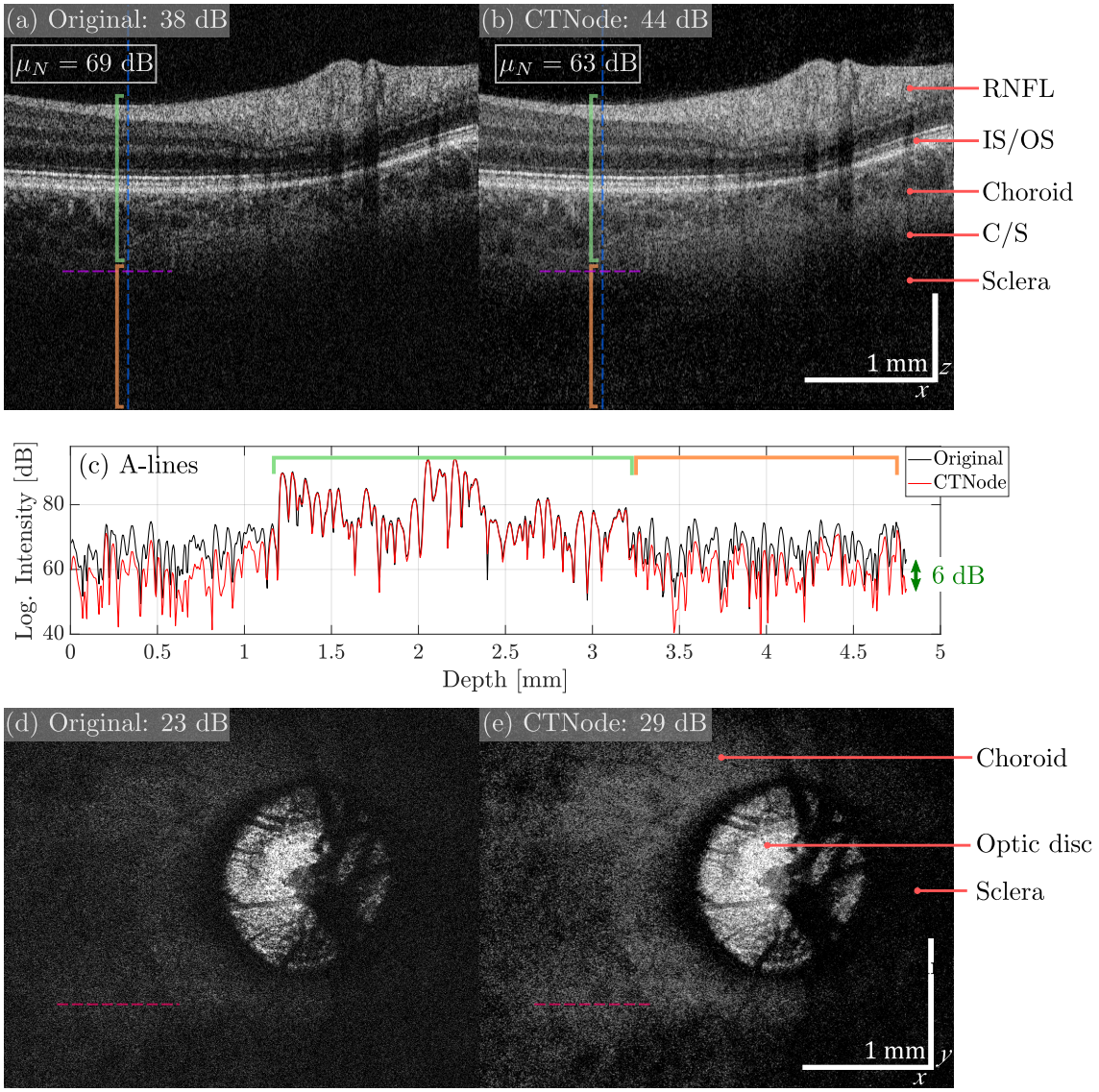

Figure 4.5: Reduction of noise with CTNode in retinal imaging *in vivo*. B-scan views: (a) original and (c) after CTNode, corresponding to the plane marked by red dashed lines in *en face* views: (d) original and (e) after CTNode, at depth marked by purple dashes lines in (a) and (b). (c) A-line profile of original and CTNode tomograms at locations marked by blue lines in (a) and (b). RNFL: retinal nerve fiber layer, IS/OS: inner and outer photoreceptors segment junction, C/S: Choroid/sclera junction.

4.3. Endoscopic imaging *in vivo*

To access internal tissue like coronary artery [195] or gastrointestinal tract [196] with endoscopic OCT, the scanner system composed of galvanometer mirrors is replaced by a catheter that is inserted into the tissue lumen to guide light and to image internal structures. Light propagates inside the catheter through an optic fiber until the output tip, then it is focused by a gradient-index (GRIN) lens and finally, it is reflected by a mirror or a prism by 90°, perpendicular to the lumen direction towards

the interior of tissue [37], as illustrated in Figure 4.6. To scan the sample, A-lines are acquired while the catheter is being rotated by an external or internal actuator, providing B-scans of axial and *azimuthal* axes. Additionally, the catheter is pulled back along the *longitudinal* axis during the scanning to acquire multiple frames producing volumetric data. The probe is enclosed in a protective transparent tube to provide stability and prevent mechanical damage arising from the direct contact of the optics and the tissue, but this element induces astigmatism given its cylindrical geometry [37, 137, 197]. As a consequence, the beam spot size in the longitudinal axis is different from that in the azimuthal axis. Furthermore, the working distance in the B-scan plane d_x becomes larger than in longitudinal plane d_y [197], as depicted in Fig. 4.6.

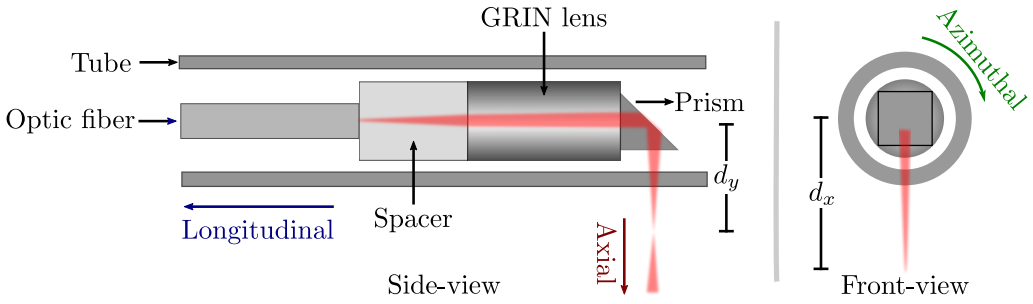

Figure 4.6: Schematic of the side and front view a catheter for OCT imaging.

In raster scan systems, it is possible to adjust the distance between the scan lens and the sample to locate the region of interest inside the imaging range: However, because the catheter-sample distance is fixed in endoscopic imaging, the working distance is a critical feature in practical scenarios. For instance, a long working distance is required in esophageal imaging, whereas a short one is demanded in coronary artery imaging [197], thus the optical design of catheters has become important [37, 137, 198], to produce astigmatism-free catheters with the desired working distance. Computational refocusing has the potential to facilitate the optical design of catheters by correcting the negative effect of astigmatism and providing focused images across a larger depth of field without the need of changing the working distance of the catheter.

The pullback of the catheter is typically performed such that the longitudinal sampling is often very sub-Nyquist and unevenly sampled. Also, severe motion artifacts appear due to the probe rotation and the pullback, and for these reasons longitudinal axis is unsuitable for numerical aberration correction, thus only 1D refocusing is possible in endoscopic imaging, which is indeed possible with SHARP-x, computing only $\tilde{S}^{1D}$ in Eq. (3.14).

To demonstrate 1D operation of SHARP in endoscopic OCT for defocus and/or astigmatism correction, pullbacks of the airway of a swine were acquired *in vivo*

with a non-k-clocked catheter-based OCT system (NinePoint Medical Inc., Bedford, MA) having a 50 kHz polygon-based wavelength-swept source with 90 nm 10-dB bandwidth at central wavelength 1310 nm and e^{-2} beam diameter of $2w_0 = 40$ μm with Rayleigh range $z_R = 1$ mm in air. SHARP was applied using P_2 only and TNode despeckling was performed afterwards using similarity and search windows of 5×5×0 and 31×31×5 pixels, respectively, and filtering parameters $h_0 = 0.06$ and $h_1 = 0.03$.

Figure 4.7 presents original and SHARP B-scans after TNode at two pullback positions showing an ROI of 450×750 px^2 above the focal plane, which is located close to the lower edge of the images, making that structures near to the catheter wall appear blurred. Although 1D correction alone is more limited than 2D correction, SHARP-x still provides an enhancement for depths $z > z_R$. In particular, debris in the mucus layer, located just below the catheter wall, is brought into focus as seen in the insets. This result suggests that SHARP-x could improve endoscopic

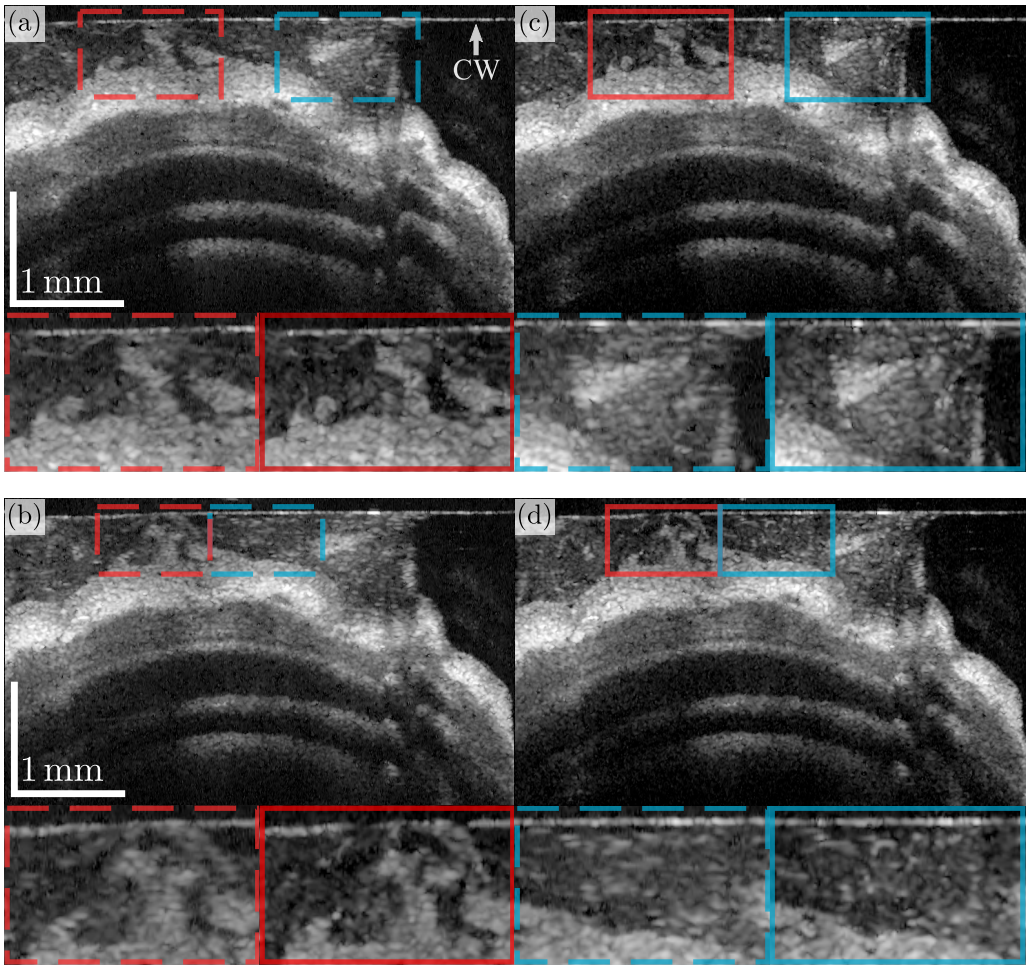

Figure 4.7: Application of SHARP in endoscopic imaging of swine airway *in vivo*. B-scan views: (a)-(b) original and (c)-(d) SHARP-x. CW: catheter wall.

imaging when there is no fixed probe-tissue working distance, such as in airway and intravascular imaging, by combining long working distance catheters with SHARP to provide focal resolution in an extended range.

4.4. Skin imaging *in vivo*

OCT offers readily observation of features of the skin such as stratum corneum, sweat ducts, and dermal/epidermal junction and promises to offer key information for quick reliable diagnosis, in applications where avoiding skin biopsy is desirable [199].

To demonstrate the operation of SHARP in skin imaging, a tomogram of a human hand dorsal surface was imaged *in vivo* with the focal plane above the sample surface, using the same system and configuration used for the proof of concept experiment but selecting now an ROI of 500 samples per A-line, 512 A-lines per B-scan and 256 B-scans. The sample was imaged around the metacarpophalangeal joint, which presents an inhomogeneous surface inducing spatial variations of defocus that make it insufficient to correct the entire lateral FoV globally. Therefore, windows-based SHARP was applied using windows of size 64×64 px^2. Although the hand of the subject was resting on a platform, small, low-frequency motion is evidenced in the tomogram, possibly dominated by heartbeat. Inter-B-scan motion correction was performed after phase stabilization along x, obtaining axial and lateral shifts of the order of a few micros, as shown in Figure 4.8(a). Small shifts can be observed in the blue inset aside Fig. 4.8(d), which do not appear after correction. TNode despeckling was applied to display all images using similarity and search windows of 7×7×7 and 15×15×15 pixels, respectively, and filtering parameters $h_0 = 0.07$ and $h_1 = 0.01$.

Figure 4.8 shows three different *en face* planes of the motion-corrected and SHARP tomograms at depths indicated by the lines on B-scan views in Figs. 4.8(b) and (c). Original *en face* views in Figs.4.8(e)-(g) present strong blurring, particularly towards the tissue surface, whereas corrected *en faces* in Fig.4.8(h)-(j) present sharper features with reduction of smearing that allows to visualize small details throughout the FoV with better contrast. For instance, fine bright structures appear after refocusing such as those marked with arrows, and differences in contrast between tissues are observed clearer, like those enclosed with circles. Most notably, the stratum corneum is brought to focus showing a reduction of the visual thickness. The major limitation of CAC techniques in dermatology is the presence of high multiple scattering that is particularly stronger in the skin than in other tissues, frustrating aberration correction for depths deep into the tissue. However, skin imaging is in general shallow due to the relatively high light absorption of skin tissue. These successful results demonstrate the ability of SHARP to refocus *in vivo* addressing not only phase noise but complex amplitude shifts as well.

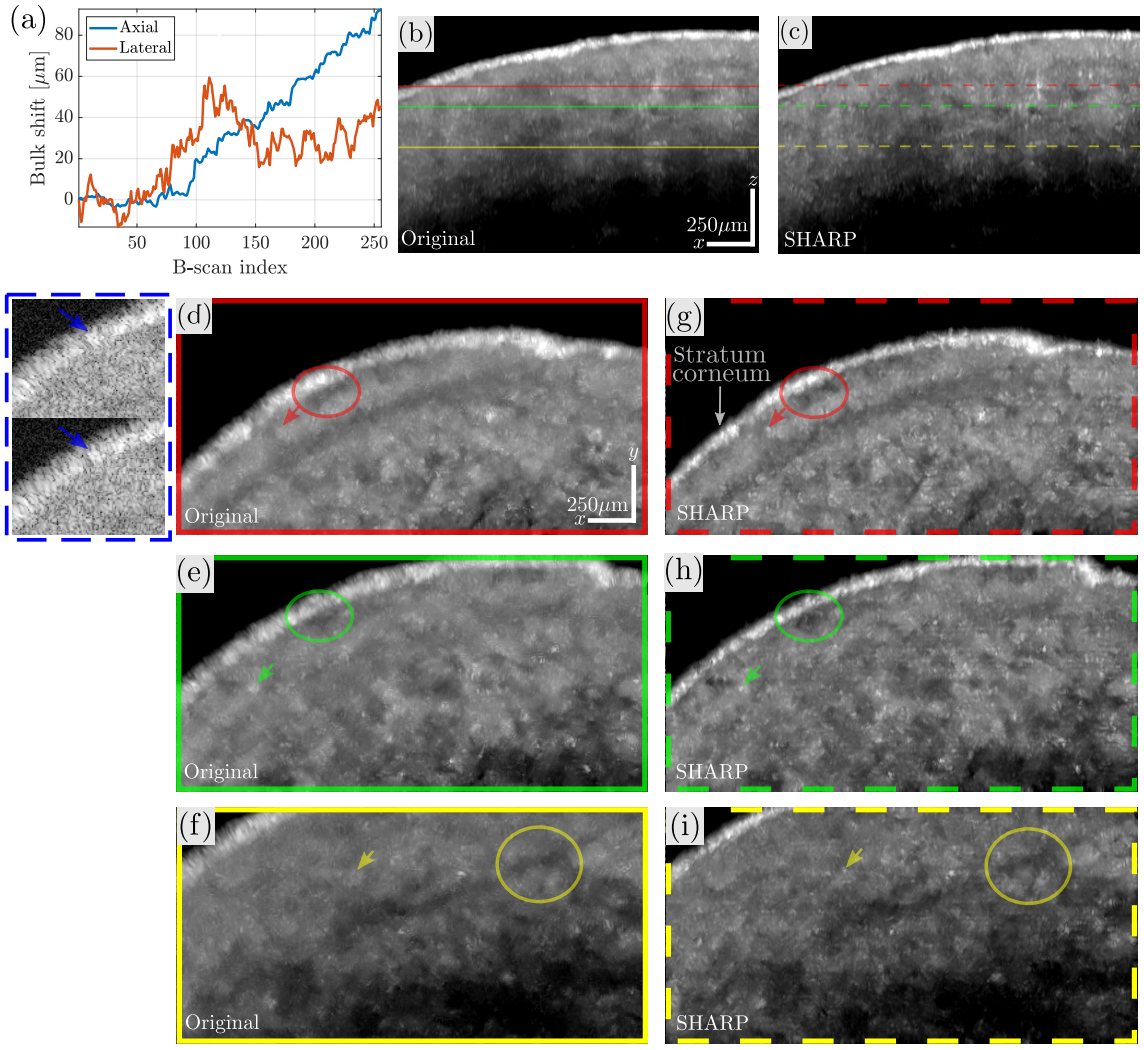

Figure 4.8: Application of SHARP in human skin imaging *in vivo*. (a) Axial and lateral shifts determined in motion correction. B-scan views: (b) before and (c) after windows-based SHARP. *En face* views at different depths marked in (b) and (c): (d)-(f) original tomogram and (g)-(i) windows-based SHARP tomogram. Blue inset corresponds to a small *en face* ROI before (top) and after (bottom) motion correction.

4.5. Computational refocusing in polarization-sensitive OCT

To demonstrate the possibility to perform computational refocusing in PS-OCT, a dataset of the anterior segment of an excised porcine eye was acquired. As seen in the previous experiments, anterior segment imaging is an attractive application that could benefit from computational refocusing due to its surface topography, which posses a long axial extension that precludes the use of medium-NA, and in particular, for PS-OCT there is a potential clinical interest in high-resolution polarimetric parameters of tissue in this application [177].

The sample was imaged around the limbus with the focal plane located deep

into the tissue targeting the trabecular meshwork. The dataset was acquired with the polygon-based SSOCT system and configuration used for the experiment in Section 4.1.2, but this time activating an integrated electro-optic modulator used to modulate the two illumination orthogonal polarization states between alternating A-lines in the fast scan axis and using a beam with a e^{-2} diameter of $2w_0 = 8.5$ μm with Rayleigh range $z_R = 90$ μm in air. The acquired spectra were split into 5 spectral windows for spectral binning processing with an overlap of 66 % between them. The tomogram contains 1024 B-scans and 1024 A-lines with 1024 depth samples, with a pixel size of 3.3 μm in lateral axes and 6 μm in the axial axis in air, from which different regions of interest were selected to process. SHARP was applied following the procedure proposed for polarization-sensitive imaging, using only defocus correction since it is the dominant aberration in the experiment, and then the Stokes parameters were spatially-averaged by using a Gaussian kernel with e^{-2} diameter 13×13 μm^2 (4×4 px^2) oriented in the lateral axes only.

The analysis was centered on the limbal region, depicted in the B-scan of Figure 4.9(a), where the short vertical yellow line represents the length of the confocal parameter. The focus is visualized approximately in the middle of the yellow box. This configuration is representative of medium-NA imaging of the limbus, where the axial extent of the tissue makes it impossible to have the whole ROI in focus. Figs. 4.9(b) and (c) show *en face* intensity views before and after SHARP, respectively, at the depth indicated by the dotted line in Fig. 4.9(a). The intensity after SHARP

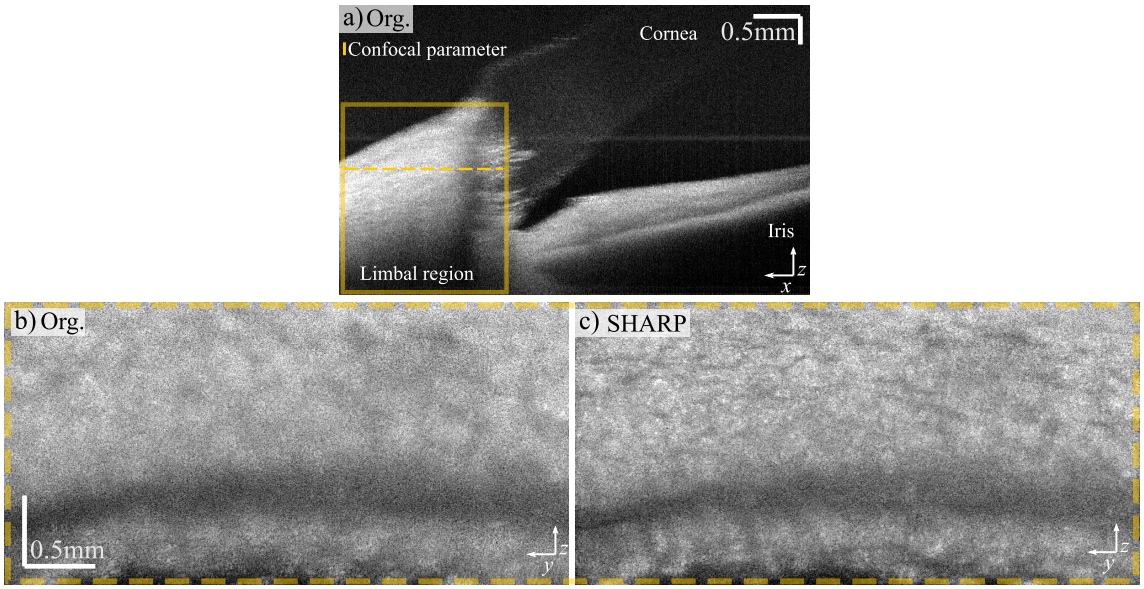

Figure 4.9: Application of SHARP in polarization-sensitive anterior segment imaging of an excised swine eye. (a) B-scan around the limbal region. The limited depth of field is very apparent. The focus is near the center of the solid box. Dotted line indicates location of *en face* views: (b) original (Org.) and (c) after SHARP.

exhibits a higher contrast and better resolution given the correction of defocus and the effect of the optimum filter.

Figure 4.10 presents cross-sectional views after PS-OCT processing of the original and SHARP tomograms. Fig. 4.10(a) shows an intensity B-scan view with a yellow line marking the location of the cross-sectional views on Figs. 4.10(b)-(d), and a red line marking the location for the *en face* views on Figs. 4.10(e)-(g). Insets show different tissue polarimetric parameters of the original data and the SHARP data side-to-side. The degree of polarization (DOP) is overlaid with the intensity in Figs. 4.10(b) and (e), local retardation is shown in Figs. 4.10(c) and (f) using a DOP threshold to display the intensity where DOP is < 0.65, and the optic axis is overlaid with the local retardation in Figs. 4.10(d) and (g). Structures in the uncorrected images appear highly affected by defocus, spatial averaging, and spectral binning. Polarimetric parameters calculated after SHARP do not exhibit any corruption in their information, furthermore successful refocusing is indicated by the clear

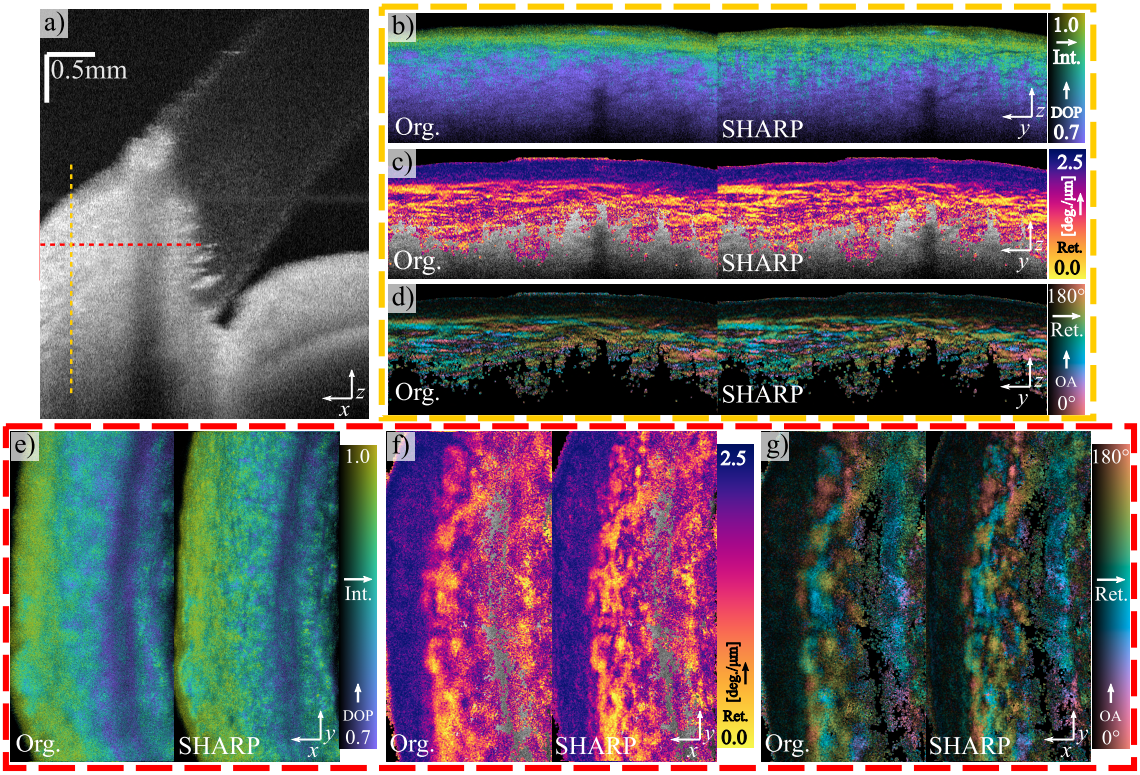

Figure 4.10: Demonstration of computational refocusing in polarimetric parameters of the anterior segment of an excised swine eye. (a) Intensity B-scan ROI around the solid box in Fig. 4.9. Cross-sectional views of tissue polarimetric parameters, showing original (Org.) and after SHARP side-to-side: (b), (e) DOP (isoluminant colormap) overlaid with intensity (luminance); (c), (f) local retardation for regions with DOP > 0.65 over the intensity; (d), (g) optic axis (cyclic isoluminant colormap) overlaid with local retardation (luminance). Axes of each cross-section are indicated in its corresponding panel.

improvement in spatial resolution in the polarimetric parameters, indicating that PS-OCT processing is indeed compatible with computational refocusing.

Correcting for defocus reveals structures that appear blurred in the original images, and provides better contrast and sharpness associated with the improvement of lateral resolution. This is noticeable in all polarimetric images, especially in the *en face* views given that refocusing operates on both lateral axes. In particular, ridges-like structures can be visualized in the DOP images with SHARP, which may be associated with the Palisades of Vogt which are functionally important structures containing stem cells, associated with the regeneration of the corneal tissue after damage [200].

There are two main limitations to the use of SHARP in PS-OCT. First, the axial resolution of the retardance and optic axis depends on the magnitude of spectral binning and the step size for local PS processing [178]. Thus, cross-sectional views [like Figs. 4.10(b)-(d)] show a less remarkable improvement than *en face* views in which defocus is corrected in both axes [like Figs. 4.10(e)-(g)]. Axial resolution loss that occurs in spectral binning Stokes processing can be avoided using Mueller processing [201] but in this case, phase stability becomes relevant because input the two orthogonal polarization states have to be phase-stable between them which currently is not achieved with SHARP. It could be possible to develop a strategy to leverage from the 1D phase stability like in SHARP but oriented to the tomograms from the two input polarization states to perform a full correction of the wavelength-dependent noise introduced by the system while maintaining the full axial resolution by using Mueller processing [201]. Although this will limit spatial averaging to the axial and only one lateral dimension, this could have attractive implications for the extraction of diattenuation information from tissue imaged with inter-A-line modulation PS-OCT systems, such as those used in intravascular OCT.

Second, the improvement in the lateral resolution after SHARP is partially neutralized by the spatial averaging required for PS-OCT processing. For this reason, advanced resolution-preserving despeckling is demanded to take full advantage of computational refocusing in PS-OCT. An extension of TNode to despeckle Stokes parameters is on current development, called polarization-sensitive-TNode (PS-TNode), and its combination with SHARP promises to be a powerful tool to improve and preserve resolution in PS-OCT imaging.

CHAPTER 5

CONCLUSIONS AND FUTURE WORKS

5.1. Conclusions

In this work, post-processing techniques were developed to improve image quality in optical coherence tomography, employing mathematical physics-based models that take advantage of the vast information contained in the OCT complex signal. These techniques provided a significant image quality enhancement in a wide variety of experimental applications, even more when complementing its operation with previously developed post-processing techniques, showing the importance and potential use of post-processing techniques in OCT for exploiting signal information to facilitate and support visualization of images for its analysis.

5.1.1. In regard to the objectives

The central aim of this work was materialized and satisfactorily accomplished with the development and experimental validation of SHARP, a technique to perform computational adaptive optics in OCT systems having 2D phase instabilities, that enables computational aberration correction in SSOCT systems with no hardware mitigation of phase-noise that were deemed unsuitable for it because of the phase stability requirement. SHARP technique is fully numerical and entirely based on the signal information itself, thus it does not require any prior knowledge of system parameters for its normal operation, and its operation does not rely on any specific configuration, thus it is compatible with standard SSOCT systems like those based on polygon wavelength-swept sources that are widespread in research and medical scenarios. SHARP operates with tomograms having phase instabilities arising from jitter in synchronization of the acquisition system, as well as other sources of phase noise like sub-resolution axial sample motion and galvanometer mirror scanners, and even inter-B-scan bulk motion with the proper complex-amplitude shifts correction also described in this work.

Given its 1D operation, SHARP is capable of correcting only x-y-separable aberrations, yet it is sufficient for many practical scenarios where defocus dominates, as is the case of most systems given the intrinsic defocus of the Gaussian beam used to probe the sample. To overcome this requirement, an extension of the method for further correction of additional aberrations, non-separable in x-y, was proposed and demonstrate with simulated data, although experimental demonstration is indeed necessary for complete validation.

SHARP proved to be a useful tool to improve lateral resolution of low and medium NA systems outside the Rayleigh range to computationally extend the depth of field in phase-unstable systems. This was demonstrated with a proof of concept experiment and additional applications in a variety of samples, including ocular, skin, and endoscopic imaging. Comments on each specific objective are given above.

To develop SHARP, a comprehensive review of state-of-art computational aberration correction techniques was carried out and then condensed in the theoretical basis of this work. Starting with the description of the general optical process occurring in the acquisition of the OCT signal, then describing in detail the most relevant computational aberration correction techniques in OCT, making particular emphasis on how phase stability requirement has been addressed throughout the development of CAC techniques. The collection of concepts, models, and bibliography in the field of CAC provided in Chapter 2 could serve as a good first general approximation for readers interested in this field.

The review of the state-of-art also allowed to identify that, indeed, the operation of CAC techniques has been very jointed to SDOCT systems in which phase stability is more straightforwardly achieved, and other custom and less common configurations like full-field systems. Furthermore, understanding the origin of phase-jitter noise and the impact of sample motion in phase stability was essential to understand the phase stabilization methods used in phase-resolved OCT and to identify key motivations for the development of SHARP, for instance, the impossibility to correct for 2D phase noise using existent 1D methods.

With the comprehension of the foundations of CAC techniques and phase stabilization methods, it was possible to properly integrate them into a fully computational method for aberration correction of OCT tomograms with no intrinsic phase stability, which was called SHARP. The method exploits 1D phase stability instead of attempting to obtain 2D and consists of an original integration of sequential 1D phase stabilization and aberration correction, performed twice to accomplish a 2D correction with an unobvious connective step. The operation of the method was exemplified in detail with a proof of concept experiment acquired with an OCT system having strong phase-jitter noise, showing successful 2D correction of defocus. Furthermore, an extension of SHARP to operate in PS-OCT was described and

demonstrated in the computational refocusing of polarimetric properties.

Performance of SHARP was evaluated in real tissue in three applications with medical relevance; ocular, airway, and skin imaging, including *ex vivo* and *in vivo* measurements, achieving successful results in all cases despite the differences in tissue and systems configuration. This is a great advantage of the fully numerical operation of SHARP that depends only on signal information. These experimental validations demonstrated the wide range of potential applications where the operation of SHARP could be beneficial. In particular, computational refocusing in skin imaging *in vivo* was possible despite the involuntary motion of the subject by integrating bulk motion correction into the SHARP procedure.

Finally, limitations of SHARP arising from its particular operation as well as inherited from the general model of CAC were discussed, but more importantly, strategies to overcome specific limitations were explained and integrated into the SHARP procedure, some of which are supported by experimental demonstrations. Furthermore, the proposed analysis on the MPS is a straightforward alternative to evaluate the minimum requirements of SHARP and CAC techniques in general. Although restriction to correct only x-y-separable aberrations is a major limitation, an alternative to overcome this was also proposed here.

5.1.2. In regard to the results

The general outcome of this work consists of two advanced techniques for OCT that aim to improve image quality through post-processing with no dependence on hardware modifications or custom configurations. The core development is SHARP, a technique that enabled computational correction of defocus in all experimental demonstrations using SSOCT systems with strong phase noise, resulting in sharper images across a larger depth of field. Proof of concept experiment showed successful refocus up to 5 times the Rayleigh range, but this limit is sample-dependent, being multiple scattering and signal loss the major practical constraints on the maximum amount of defocus that is correctable, i.e. the maximum possible extension of the depth of field. In this experiment, computational refocused images after SHARP exhibit a resolution similar to the experimental in-focus reference images.

Introduction of the MPS as a tool for assessing CAC requirements, namely phase stability, and sampling, and the use of the optimum filter for noise filtering are valuable side results not only for the field of CAC but also for the OCT community.

Anterior segment imaging profiles as a potential relevant application for SHARP given the interest of obtaining high-resolution images in an extended axial range to cover the extent of the cornea. Also, because of the spatial variation of aberrations that may introduce the corneal curvature, that can be corrected by SHARP. In

this case, the use of a resolution-preserving despeckling technique like TNode in combination with SHARP provided a very significant improvement of image quality in comparison to original images where defocus and speckle make visualization difficult.

Improvements in anterior segment imaging were also achieved complementing SHARP with CTNode technique, which offered a great noise reduction allowing to visualize low- and medium-intensity regions with better contrast. CTNode showed to be an effective technique to reduce noise exploiting the available information given its non-local means operation, as analyzed in the validation with simulated data, where an equivalent performance to coherent averaging of 12 repetition frames was achieved with CTNode but needing a single repetition frame. Furthermore, noise reduction was demonstrated in human retina imaging *in vivo*, aiming to improve SNR in low-intensity regions like the choroid and sclera, at the cost of reducing the contrast of medium and high-SNR layers. Although the demonstration here is shown only in intensity-contrast images, CTNode promises to be a useful technique for noise reduction in phase-dependent techniques.

In endoscopic imaging, successful refocusing was demonstrated *in vivo*, close to the catheter wall which is a region located far from the focal plane in long working distance catheters. Visualization of results was also enhanced by TNode despeckling. This demonstration suggests that computational refocusing could allow improving lateral resolution using inexpensive optical design of catheter probes, instead of using sophisticated designs to account for astigmatism.

Although aberration correction is limited in skin tissue due to the presence of multiple scattering, the *in vivo* experiment in skin imaging is a valuable demonstration. First, because of the presence of involuntary sample motion that is known to be a notable restriction in CAC techniques, which was successfully corrected in SHARP. Second, the irregular topography of the tissue is a clear example of the need of spatial-varying aberration correction.

The demonstration of computational refocusing in PS-OCT is the first experimental demonstration to the best of our knowledge. Results exhibit an improvement of lateral resolution in the estimated polarimetric parameters of tissue in the limbal region of the anterior segment, despite the negative effect of spatial filtering process that is inherent to PS-OCT processing, showing the potential of SHARP to improve resolution in PS-OCT that generally possess a coarse resolution. This improvement is very relevant in the quantitative assessment of polarimetric properties of tissue used for analysis and diagnosis of diseases.

5.2. Perspective of improvements and future works

There are many ideas and experiments that could help to improve the proposed techniques. Aberration correction in the retina with SHARP is a key following validation to determine the possibility to correct beyond x-y-separable aberrations with the proposed extension.

For correction of spatial-varying aberrations, a more localized approach has been devised in which the optimal weights in CAO are determined using small windows with high overlap to produce a dense map of weights, interpolated to obtain the correction of individual pixels that are then applied pixel-wise using an integral transformation in the spatial domain, instead of applying a global correction in Fourier domain for all pixels within the windows.

It is expected that the performance of the optimum filter may vary for different oversampling values, being more effective as oversampling increases. This could be analyzed experimentally by imaging a phantom or a simple sample at different oversampling values and comparing the performance of the optimum filter and the practicality of this approach for noise reduction.

Regarding CTNode, there are yet open issues and questions to solve, for instance, how it impacts phase stability and what is the impact of phase stability on its performance. Also, the effectiveness of the method must be evaluated in a systematic experiment where it could be compared to coherent averaging, additionally expanding operation of CTNode to work with multiple frames repetitions which is straightforwardly obtainable with compounding of probabilities as in TNode. Furthermore, its utility in functional phase-dependent techniques must be evaluated experimentally, possibly in angiography or elastography. Finally, it has been speculated that the operation of TNode could be boosted by operating in the complex signal similarly to CTNode. The idea is to perform the incoherent non-local means of TNode but determining the weights by computing the similarity criterion in the complex signal like in CTNode.

Concerning PSOCT, refinements in the resolution-preserving despeckling technique PS-TNode are yet to be finished, and after that, it could be possible to combine SHARP with PS-TNode to achieve an even greater resolution improvement in images of polarimetric properties than the achieved so far with traditional spatial filtering. Furthermore, numerical phase-stabilization strategies have been devised to obtain phase-stable Jones vectors which can be converted into Mueller matrices to perform a correction of system polarization effects without the axial resolution loss that occurs in spectral binning Stokes processing.

Finally, proper integration of SHARP with angiography processing is also due, to maintain the expansion of CAC into different functional imaging techniques in OCT.

5.3. Collection of publications and presentations

The core of SHARP procedure was already published [72]:

S. Ruiz-Lopera, R. Restrepo, C. Cuartas-Vélez, B. E. Bouma, and N. Uribe-Patarroyo, "Computational adaptive optics in phase-unstable optical coherence tomography," *Optics Letters*, vol. 45, no. 21, pp. 5982-5985 2020.

An additional work has been published in regard to noise and bias analysis in OCT intensity based signal decorrelation employed in functional imaging [57]:

N. Uribe-Patarroyo, A. L. Post, S. Ruiz-Lopera, D. J. Faber, and B. E. Bouma, "Noise and bias in optical coherence tomography intensity signal decorrelation," *OSA Continuum*, vol. 3, p. 709, 2020.

Past works have also included experimental OCT setups [58, 59]:

C. Cuartas-Vélez, S. Ruiz-Lopera, N. Uribe-Patarroyo, and R. Restrepo,"Lab-made accessible full-field optical coherence tomography imaging system," *Optica Pura y Aplicada*, vol. 52, no. 3, pp. 1–11, 2019.

Oral presentations have been given in international conferences:

- S. Ruiz-Lopera, R. Restrepo, C. Cuartas-Vélez, B. E. Bouma, and N. Uribe-Patarroyo, "Digital adaptive optics in optical coherence tomography with phase unstable sources," in *Photonic West*, (San Francisco), [no proceeding], SPIE, 2020.

- S. Ruiz-Lopera, R. Restrepo, C. Cuartas-Vélez, B. E. Bouma, and N. Uribe-Patarroyo, "Digital refocusing and aberration compensation in optical coherence tomography with phase-unstable sources," in *Photonic West*, (Munich), [no proceeding], SPIE, 2019.

- R. Restrepo, S. Ruiz-Lopera, C. Cuartas-Vélez, J. Ren, B. E. Bouma, and N. Uribe-Patarroyo, "Phase-jitter correction for swept-source OCT digital refocusing," in *Photonic West*, (San Francisco), [no proceeding], SPIE, 2019.

- S. Ruiz-Lopera and R. Restrepo, "Design of a Linear in Wavenumber Spectrometer," in *Latin America Optics and Photonics Conference*, (Lima), p. W2B.3, OSA, 2018.

REFERENCES

[1] G. Keiser, *Biophotonics: Concepts to Applications*. Graduate Texts in Physics, Singapore: Springer, 2016.

[2] J. G. Fujimoto and W. Drexler, *Optical Coherence Tomography: Technology and Applications*. Springer, 2015.

[3] D. Huang, E. Swanson, C. Lin, J. Schuman, W. Stinson, W. Chang, M. Hee, T. Flotte, K. Gregory, C. Puliafito, and a. et, "Optical coherence tomography," *Science*, vol. 254, no. 5035, pp. 1178–1181, 1991.

[4] J. G. Fujimoto and W. Drexler, "Introduction to OCT," in *Optical Coherence Tomography* (W. Drexler and J. G. Fujimoto, eds.), pp. 3–64, Cham: Springer International Publishing, 2015.

[5] E. A. Swanson, J. A. Izatt, C. P. Lin, J. G. Fujimoto, J. S. Schuman, M. R. Hee, D. Huang, and C. A. Puliafito, "In vivo retinal imaging by optical coherence tomography," *Optics Letters*, vol. 18, no. 21, p. 1864, 1993.

[6] J. S. Schuman, C. A. Puliafito, and J. G. Fujimoto, eds., *Optical Coherence Tomography of Ocular Diseases*. Thorofare, NJ: SLACK Inc, 2nd ed ed., 2004.

[7] G. J. Tearney, "In Vivo Endoscopic Optical Biopsy with Optical Coherence Tomography," *Science*, vol. 276, no. 5321, pp. 2037–2039, 1997.

[8] G. J. Tearney, M. E. Brezinski, S. A. Boppart, B. E. Bouma, N. Weissman, J. F. Southern, E. A. Swanson, and J. G. Fujimoto, "Catheter-Based Optical Imaging of a Human Coronary Artery," *Circulation*, vol. 94, no. 11, pp. 3013–3013, 1996.

[9] B. E. Bouma, M. Villiger, K. Otsuka, and W.-Y. Oh, "Intravascular optical coherence tomography [Invited]," *Biomedical Optics Express*, vol. 8, no. 5, p. 2660, 2017.

[10] J. Welzel, E. Lankenau, R. Birngruber, and R. Engelhardt, "Optical coherence tomography of the human skin," *Journal of the American Academy of Dermatology*, vol. 37, no. 6, pp. 958–963, 1997.

[11] J. Olsen, J. Holmes, and G. B. E. Jemec, "Advances in optical coherence tomography in dermatology—a review," *Journal of Biomedical Optics*, vol. 23, no. 04, p. 1, 2018.

[12] B. W. Colston, M. J. Everett, L. B. Da Silva, L. L. Otis, P. Stroeve, and H. Nathel, "Imaging of hard- and soft-tissue structure in the oral cavity by optical coherence tomography," *Applied Optics*, vol. 37, no. 16, p. 3582, 1998.

[13] M. J. Suter, S. Lam, and M. Brenner, "Optical techniques in pulmonary medicine," *Expert Review of Respiratory Medicine*, vol. 6, no. 2, pp. 143–145, 2012.

[14] B. J. Vakoc, D. Fukumura, R. K. Jain, and B. E. Bouma, "Cancer imaging by optical coherence tomography: Preclinical progress and clinical potential," *Nature Reviews Cancer*, vol. 12, no. 5, pp. 363–368, 2012.

[15] P. R. Hoskins, K. Martin, and A. Thrush, *Diagnostic Ultrasound: Physics and Equipment*. 2019.

[16] J. G. Fujimoto, M. E. Brezinski, G. J. Tearney, S. A. Boppart, B. Bouma, M. R. Hee, J. F. Southern, and E. A. Swanson, "Optical biopsy and imaging using optical coherence tomography," *Nature Medicine*, vol. 1, no. 9, pp. 970–972, 1995.

[17] J. M. Schmitt, A. Knuttel, M. Yadlowsky, and M. A. Eckhaus, "Optical-coherence tomography of a dense tissue: Statistics of attenuation and backscattering," *Physics in Medicine and Biology*, vol. 39, no. 10, pp. 1705–1720, 1994.

[18] A. F. Fercher, C. K. Hitzenberger, W. Drexler, G. Kamp, and H. Sattmann, "In Vivo Optical Coherence Tomography," *American Journal of Ophthalmology*, vol. 116, no. 1, pp. 113–114, 1993.

[19] E. A. Swanson, J. A. Izatt, C. P. Lin, J. G. Fujimoto, J. S. Schuman, M. R. Hee, D. Huang, and C. A. Puliafito, "In vivo retinal imaging by optical coherence tomography," *Optics Letters*, vol. 18, no. 21, p. 1864, 1993.

[20] C. A. Puliafito, M. R. Hee, C. P. Lin, E. Reichel, J. S. Schuman, J. S. Duker, J. A. Izatt, E. A. Swanson, and J. G. Fujimoto, "Imaging of Macular Diseases with Optical Coherence Tomography," *Ophthalmology*, vol. 102, no. 2, pp. 217–229, 1995.

[21] C. R. Chu, N. J. Izzo, J. J. Irrgang, M. Ferretti, and R. K. Studer, "Clinical diagnosis of potentially treatable early articular cartilage degeneration using

optical coherence tomography," *Journal of Biomedical Optics*, vol. 12, no. 5, p. 051703, 2007.

[22] P. Sathyan and S. Anitha, "Optical Coherence Tomography in Glaucoma," *Journal of Current Glaucoma Practice*, vol. 6, no. 1, pp. 1–5, 2012.

[23] J. S. Schuman, "Quantification of Nerve Fiber Layer Thickness in Normal and Glaucomatous Eyes Using Optical Coherence Tomography: A Pilot Study," *Archives of Ophthalmology*, vol. 113, no. 5, p. 586, 1995.

[24] O. M. Carrasco-Zevallos, C. Viehland, B. Keller, M. Draelos, A. N. Kuo, C. A. Toth, and J. A. Izatt, "Review of intraoperative optical coherence tomography: Technology and applications [Invited]," *Biomedical Optics Express*, vol. 8, no. 3, p. 1607, 2017.

[25] W. Chang, Y. Fan, X. Zhang, and H. Liao, "An Intelligent Theranostics Method Using Optical Coherence Tomography Guided Automatic Laser Ablation for Neurosurgery," in *2018 40th Annual International Conference of the IEEE Engineering in Medicine and Biology Society (EMBC)*, (Honolulu, HI), pp. 3224–3227, IEEE, 2018.

[26] R. Maltais-Tariant, C. Boudoux, and N. Uribe-Patarroyo, "Real-time co-localized OCT surveillance of laser therapy using motion corrected speckle decorrelation," *Biomedical Optics Express*, vol. 11, no. 6, p. 2925, 2020.

[27] J. Welzel, "Optical coherence tomography in dermatology: A review," *Skin Research and Technology*, vol. 7, no. 1, pp. 1–9, 2001.

[28] L. Carrion, M. Lestrade, Z. Xu, G. Touma, R. Maciejko, and M. Bertrand, "Comparative study of optical sources in the near infrared for optical coherence tomography applications," *Journal of Biomedical Optics*, vol. 12, no. 1, p. 014017, 2007.

[29] L. Ferrante di Ruffano, J. Dinnes, J. J. Deeks, N. Chuchu, S. E. Bayliss, C. Davenport, Y. Takwoingi, K. Godfrey, C. O'Sullivan, R. N. Matin, H. Tehrani, H. C. Williams, and Cochrane Skin Cancer Diagnostic Test Accuracy Group, "Optical coherence tomography for diagnosing skin cancer in adults," *Cochrane Database of Systematic Reviews*, 2018.

[30] S. Jäckle, N. Gladkova, F. Feldchtein, A. Terentieva, B. Brand, G. Gelikonov, V. Gelikonov, A. Sergeev, A. Fritscher-Ravens, J. Freund, U. Seitz, S. Schröder, and N. Soehendra, "In Vivo Endoscopic Optical Coherence Tomography of the Human Gastrointestinal Tract - Toward Optical Biopsy," *Endoscopy*, vol. 32, no. 10, pp. 743–749, 2000.

[31] J. J. Armstrong, M. S. Leigh, I. D. Walton, A. V. Zvyagin, S. A. Alexandrov, S. Schwer, D. D. Sampson, D. R. Hillman, and P. R. Eastwood, "In vivo size and shape measurement of the human upper airway using endoscopic long-range optical coherence tomography," *Optics Express*, vol. 11, no. 15, p. 1817, 2003.

[32] R. A. McLaughlin, B. C. Quirk, A. Curatolo, R. W. Kirk, L. Scolaro, D. Lorenser, P. D. Robbins, B. A. Wood, C. M. Saunders, and D. D. Sampson, "Imaging of Breast Cancer With Optical Coherence Tomography Needle Probes: Feasibility and Initial Results," *IEEE Journal of Selected Topics in Quantum Electronics*, vol. 18, no. 3, pp. 1184–1191, 2012.

[33] T. Ralston, D. Marks, P. Carney, and S. Boppart, "Interferometric synthetic aperture microscopy: Inverse scattering for optical coherence tomography," *Optics and Photonics News*, vol. 17, no. 12, p. 25, 2006.

[34] Y. Yasuno, J.-i. Sugisaka, Y. Sando, Y. Nakamura, S. Makita, M. Itoh, and T. Yatagai, "Non-iterative numerical method for laterally superresolving Fourier domain optical coherence tomography," *Optics Express*, vol. 14, no. 3, pp. 1006–1020, 2006.

[35] S. Adie, B. Graf, A. Ahmad, P. Carney, and S. Boppart, "Computational adaptive optics for broadband optical interferometric tomography of biological tissue," *Proceedings of the National Academy of Sciences of the United States of America*, vol. 109, no. 19, pp. 7175–7180, 2012.

[36] R. J. Zawadzki, S. M. Jones, S. S. Olivier, M. Zhao, B. A. Bower, J. A. Izatt, S. Choi, S. Laut, and J. S. Werner, "Adaptive-optics optical coherence tomography for high-resolution and high-speed 3D retinal in vivo imaging," *Optics Express*, vol. 13, no. 21, p. 8532, 2005.

[37] Z. Hu and A. M. Rollins, "Optical Design for OCT," in *Optical Coherence Tomography* (W. Drexler and J. G. Fujimoto, eds.), pp. 357–384, Cham: Springer International Publishing, 2015.

[38] G. Walsh, H. C. Howland, and W. N. Charman, "Objective technique for the determination of monochromatic aberrations of the human eye," *Journal of the Optical Society of America A*, vol. 1, no. 9, p. 987, 1984.

[39] J. Liang and D. R. Williams, "Aberrations and retinal image quality of the normal human eye," *Journal of the Optical Society of America A*, vol. 14, no. 11, p. 2873, 1997.

[40] B. Cense, W. Gao, J. M. Brown, S. M. Jones, R. S. Jonnal, M. Mujat, B. H. Park, J. F. de Boer, and D. T. Miller, "Retinal imaging with polarization-sensitive optical coherence tomography and adaptive optics," *Optics Express*, vol. 17, no. 24, p. 21634, 2009.

[41] K. S. Park, J. W. Kim, B. H. Lee, and T. J. Eom, "Angiographic Imaging of an In Vivo Mouse Brain as a Guiding Star for Automatic Digital Refocusing in OCT," *Applied Sciences*, vol. 10, no. 4, p. 1210, 2020.

[42] J. F. de Boer, T. E. Milner, M. J. C. van Gemert, and J. S. Nelson, "Two-dimensional birefringence imaging in biological tissue by polarization-sensitive optical coherence tomography," *Optics Letters*, vol. 22, no. 12, p. 934, 1997.

[43] R. K. Wang, S. L. Jacques, Z. Ma, S. Hurst, S. R. Hanson, and A. Gruber, "Three dimensional optical angiography," *Optics Express*, vol. 15, no. 7, p. 4083, 2007.

[44] Y. Zhang, B. Cense, J. Rha, R. S. Jonnal, W. Gao, R. J. Zawadzki, J. S. Werner, S. Jones, S. Olivier, and D. T. Miller, "High-speed volumetric imaging of cone photoreceptors with adaptive optics spectral-domain optical coherence tomography," *Optics Express*, vol. 14, no. 10, p. 4380, 2006.

[45] M. Pircher and R. Zawadzki, "Review of adaptive optics OCT (AO-OCT): Principles and applications for retinal imaging [invited]," *Biomedical Optics Express*, vol. 8, no. 5, pp. 2536–2562, 2017.

[46] M. Wu, D. Small, N. Nishimura, and S. Adie, "Computed optical coherence microscopy of mouse brain ex vivo," *Journal of Biomedical Optics*, vol. 24, no. 11, 2019.

[47] N. D. Shemonski, S. G. Adie, Y.-Z. Liu, F. A. South, P. S. Carney, and S. A. Boppart, "Stability in computed optical interferometric tomography (Part I): Stability requirements," *Optics Express*, vol. 22, no. 16, p. 19183, 2014.

[48] J. A. Izatt, M. A. Choma, and A.-H. Dhalla, "Theory of Optical Coherence Tomography," in *Optical Coherence Tomography* (W. Drexler and J. G. Fujimoto, eds.), pp. 65–94, Cham: Springer International Publishing, 2015.

[49] J. W. Goodman, *Speckle Phenomena in Optics: Theory and Applications*. Englewood, Colo: Roberts & Co, 2007.

[50] J. Lee, W. Wu, J. Y. Jiang, B. Zhu, and D. A. Boas, "Dynamic light scattering optical coherence tomography," *Optics Express*, vol. 20, no. 20, p. 22262, 2012.

[51] X. Liu, Y. Huang, J. C. Ramella-Roman, S. A. Mathews, and J. U. Kang, "Quantitative transverse flow measurement using optical coherence tomography speckle decorrelation analysis," *Optics Letters*, vol. 38, no. 5, p. 805, 2013.

[52] J. M. Schmitt, S. H. Xiang, and K. M. Yung, "Speckle in Optical Coherence Tomography," *Journal of Biomedical Optics*, vol. 4, no. 1, p. 95, 1999.

[53] C. Cuartas-Vélez, R. Restrepo, B. E. Bouma, and N. Uribe-Patarroyo, "Volumetric non-local-means based speckle reduction for optical coherence tomography," *Biomedical Optics Express*, vol. 9, no. 7, p. 3354, 2018.

[54] F. Argenti, A. Lapini, T. Bianchi, and L. Alparone, "A Tutorial on Speckle Reduction in Synthetic Aperture Radar Images," *IEEE Geoscience and Remote Sensing Magazine*, vol. 1, no. 3, pp. 6–35, 2013.

[55] J. F. de Boer, B. Cense, B. H. Park, M. C. Pierce, G. J. Tearney, and B. E. Bouma, "Improved signal-to-noise ratio in spectral-domain compared with time-domain optical coherence tomography," *Optics Letters*, vol. 28, no. 21, p. 2067, 2003.

[56] B. Baumann, C. W. Merkle, R. A. Leitgeb, M. Augustin, A. Wartak, M. Pircher, and C. K. Hitzenberger, "Signal averaging improves signal-to-noise in OCT images: But which approach works best, and when?," *Biomedical Optics Express*, vol. 10, no. 11, p. 5755, 2019.

[57] N. Uribe-Patarroyo, A. L. Post, S. Ruiz-Lopera, D. J. Faber, and B. E. Bouma, "Noise and bias in optical coherence tomography intensity signal decorrelation," *OSA Continuum*, vol. 3, no. 4, p. 709, 2020.

[58] C. Cuartas-Vélez, S. Ruiz-Lopera, N. Uribe-Patarroyo, and R. Restrepo, "Lab-made accessible full-field optical coherence tomography imaging system," *Optica Pura y Aplicada*, vol. 52, no. 3, pp. 1–11, 2019.

[59] S. Ruiz-Lopera and R. Restrepo, "Design of a Linear in Wavenumber Spectrometer," in *Latin America Optics and Photonics Conference*, (Lima), p. W2B.3, OSA, 2018.

[60] C. Cuartas-Vélez, *Formación y restauración de imagen en tomografía óptica de coherencia mediante posprocesamiento*. Masther thesis, Universidad EAFIT, Medellín, 2017.

[61] D. Hillmann, H. Spahr, C. Hain, H. Sudkamp, G. Franke, C. Pfäffle, C. Winter, and G. Hüttmann, "Aberration-free volumetric high-speed imaging of in vivo retina," *Scientific Reports*, vol. 6, no. 1, p. 35209, 2016.

[62] A. Kumar, L. Wurster, M. Salas, L. Ginner, W. Drexler, and R. Leitgeb, "In-vivo digital wavefront sensing using swept source OCT," *Biomedical Optics Express*, vol. 8, no. 7, pp. 3369–3382, 2017.

[63] B. J. Vakoc, S. H. Yun, J. F. de Boer, G. J. Tearney, and B. E. Bouma, "Phase-resolved optical frequency domain imaging," *Optics Express*, vol. 13, no. 14, p. 5483, 2005.

[64] N. Shemonski, A. Ahmad, S. Adie, Y.-Z. Liu, F. South, P. Carney, and S. Boppart, "Stability in computed optical interferometric tomography (Part II): In vivo stability assessment," *Optics Express*, vol. 22, no. 16, pp. 19314–19326, 2014.

[65] N. D. Shemonski, S. S. Ahn, Y.-Z. Liu, F. A. South, P. S. Carney, and S. A. Boppart, "Three-dimensional motion correction using speckle and phase for in vivo computed optical interferometric tomography," *Biomedical Optics Express*, vol. 5, no. 12, p. 4131, 2014.

[66] Z. Chen, T. E. Milner, D. Dave, and J. S. Nelson, "Optical Doppler tomographic imaging of fluid flow velocity in highly scattering media," *Optics Letters*, vol. 22, no. 1, p. 64, 1997.

[67] B. R. White, M. C. Pierce, N. Nassif, B. Cense, B. H. Park, G. J. Tearney, B. E. Bouma, T. C. Chen, and J. F. de Boer, "In vivo dynamic human retinal blood flow imaging using ultra-high-speed spectral domain optical Doppler tomography," *Optics Express*, vol. 11, no. 25, p. 3490, 2003.

[68] L. Ginner, T. Schmoll, A. Kumar, M. Salas, N. Pricoupenko, L. M. Wurster, and R. A. Leitgeb, "Holographic line field en-face OCT with digital adaptive optics in the retina in vivo," *Biomedical Optics Express*, vol. 9, no. 2, pp. 472–485, 2018.

[69] A. Kumar, W. Drexler, and R. Leitgeb, "Subaperture correlation based digital adaptive optics for full field optical coherence tomography," *Optics Express*, vol. 21, no. 9, pp. 10850–10866, 2013.

[70] H. Sudkamp, D. Hillmann, P. Koch, M. vom Endt, H. Spahr, M. Münst, C. Pfäffle, R. Birngruber, and G. Hüttmann, "Simple approach for aberration-corrected OCT imaging of the human retina," *Optics Letters*, vol. 43, no. 17, p. 4224, 2018.

[71] T. Ralston, D. Marks, P. Carney, and S. Boppart, "Phase Stability Technique for Inverse Scattering in Optical Coherence Tomography," in *3rd IEEE International Symposium on Biomedical Imaging: Macro to Nano, 2006.*, (Arlington, Virginia, USA), pp. 578–581, IEEE, 2006.

[72] S. Ruiz-Lopera, R. Restrepo, C. Cuartas-Vélez, B. E. Bouma, and N. Uribe-Patarroyo, "Computational adaptive optics in phase-unstable optical coherence tomography," *Optics Letters*, vol. 45, no. 21 [in press], 2020.

[73] A. Fercher, C. Hitzenberger, G. Kamp, and S. El-Zaiat, "Measurement of intraocular distances by backscattering spectral interferometry," *Optics Communications*, vol. 117, no. 1-2, pp. 43–48, 1995.

[74] S. R. Chinn, E. A. Swanson, and J. G. Fujimoto, "Optical coherence tomography using a frequency-tunable optical source," *Optics Letters*, vol. 22, no. 5, p. 340, 1997.

[75] S. Yun, G. Tearney, J. de Boer, N. Iftimia, and B. Bouma, "High-speed optical frequency-domain imaging," *Optics Express*, vol. 11, no. 22, p. 2953, 2003.

[76] C. Guy and D. ffytche, *An Introduction to the Principles of Medical Imaging*. PUBLISHED BY IMPERIAL COLLEGE PRESS AND DISTRIBUTED BY WORLD SCIENTIFIC PUBLISHING CO., revised ed., 2005.

[77] T. L. Szabo, *Diagnostic Ultrasound Imaging: Inside Out*. MATLAB Examples, Amsterdam ; Boston: Elsevier/AP, Academic Press is an imprint of Elsevier, second edition ed., 2014.

[78] M. A. Duguay and A. T. Mattick, "Ultrahigh Speed Photography of Picosecond Light Pulses and Echoes," *Applied Optics*, vol. 10, no. 9, p. 2162, 1971.

[79] M. A. Duguay, "Light Photographed in Flight," *American Scientist*, vol. 59, no. 5, pp. 550–556, 1971.

[80] J. G. Fujimoto, C. A. Puliafito, R. Margolis, A. Oseroff, S. De Silvestri, and E. P. Ippen, "Femtosecond optical ranging in biological systems," *Optics Letters*, vol. 11, no. 3, p. 150, 1986.

[81] K. Takada, I. Yokohama, K. Chida, and J. Noda, "New measurement system for fault location in optical waveguide devices based on an interferometric technique," *Applied Optics*, vol. 26, no. 9, p. 1603, 1987.

[82] R. C. Youngquist, S. Carr, and D. E. N. Davies, "Optical coherence-domain reflectometry: A new optical evaluation technique," *Optics Letters*, vol. 12, no. 3, p. 158, 1987.

[83] A. F. Fercher, K. Mengedoht, and W. Werner, "Eye-length measurement by interferometry with partially coherent light," *Optics Letters*, vol. 13, no. 3, p. 186, 1988.

[84] D. Malacara, ed., *Optical Shop Testing*. Wiley Series in Pure and Applied Optics, Hoboken, N.J: Wiley-Interscience, 3rd ed., 2007.

[85] E. Hecht, *Optics*. Pearson Global Edition, Boston Columbus Indianapolis: Pearson, fifth ed., 2017.

[86] A. G. Podoleanu, "Unbalanced versus balanced operation in an optical coherence tomography system," *Applied Optics*, vol. 39, no. 1, p. 173, 2000.

[87] R. Leitgeb, C. Hitzenberger, and A. Fercher, "Performance of fourier domain vs time domain optical coherence tomography," *Optics Express*, vol. 11, no. 8, p. 889, 2003.

[88] M. Choma, M. Sarunic, C. Yang, and J. Izatt, "Sensitivity advantage of swept source and Fourier domain optical coherence tomography," *Optics Express*, vol. 11, no. 18, p. 2183, 2003.

[89] B. E. Bouma, G. J. Tearney, B. Vakoc, and S. H. Yun, "Optical Frequency Domain Imaging," in *Optical Coherence Tomography* (W. Drexler and J. G. Fujimoto, eds.), pp. 225–254, Cham: Springer International Publishing, 2015.

[90] Y. Okabe, Y. Sasaki, M. Ueno, T. Sakamoto, S. Toyoda, S. Yagi, K. Naganuma, K. Fujiura, Y. Sakai, J. Kobayashi, K. Omiya, M. Ohmi, and M. Haruna, "200 kHz swept light source equipped with KTN deflector for optical coherence tomography," *Electronics Letters*, vol. 48, no. 4, p. 201, 2012.

[91] W.-Y. Oh, B. J. Vakoc, M. Shishkov, G. J. Tearney, and B. E. Bouma, ">400 kHz repetition rate wavelength-swept laser and application to high-speed optical frequency domain imaging," *Optics Letters*, vol. 35, no. 17, p. 2919, 2010.

[92] S. H. Yun and B. E. Bouma, "Wavelength Swept Lasers," in *Optical Coherence Tomography* (W. Drexler and J. G. Fujimoto, eds.), pp. 619–637, Cham: Springer International Publishing, 2015.

[93] C. Dorrer, N. Belabas, J.-P. Likforman, and M. Joffre, "Spectral resolution and sampling issues in Fourier-transform spectral interferometry," *Journal of the Optical Society of America B*, vol. 17, no. 10, p. 1795, 2000.

[94] A. Yariv, P. Yeh, and A. Yariv, *Photonics: Optical Electronics in Modern Communications*. The Oxford Series in Electrical and Computer Engineering, New York: Oxford University Press, 6th ed ed., 2007.

[95] A. Yasin Alibhai, C. Or, and A. J. Witkin, "Swept Source Optical Coherence Tomography: A Review," *Current Ophthalmology Reports*, vol. 6, no. 1, pp. 7–16, 2018.

[96] B. E. A. Saleh and M. C. Teich, *Fundamentals of Photonics*. Wiley Series in Pure and Applied Optics, New York: Wiley, 1991.

[97] E. C. Vail, M. S. Wu, G. S. Li, W. Yuen, and C. J. Chang-Hasnain, "Tunable Micromachined Vertical Cavity Surface Emitting Lasers," in *Quantum Electronics and Laser Science Conference*, vol. 16, (Baltimore), p. paper QPD12, OSA Technical Digest (Optical Society of America, 1995), 1995.

[98] V. Jayaraman, J. Jiang, H. Li, P. Heim, G. Cole, B. Potsaid, J. G. Fujimoto, and A. Cable, "OCT Imaging up to 760Khz Axial Scan Rate Using Single-Mode 1310nm MEMs-Tunable VCSELs with >100nm Tuning Range," in *CLEO:2011 - Laser Applications to Photonic Applications*, (Baltimore, Maryland), p. PDPB2, OSA, 2011.

[99] H. D. Lee, G. H. Kim, J. G. Shin, B. Lee, C.-S. Kim, and T. J. Eom, "Akinetic swept-source optical coherence tomography based on a pulse-modulated active mode locking fiber laser for human retinal imaging," *Scientific Reports*, vol. 8, no. 1, p. 17660, 2018.

[100] B. Vakoc, G. Tearney, and B. Bouma, "Statistical Properties of Phase-Decorrelation in Phase-Resolved Doppler Optical Coherence Tomography," *IEEE Transactions on Medical Imaging*, vol. 28, no. 6, pp. 814–821, 2009.

[101] Y.-J. Hong, S. Makita, F. Jaillon, M. J. Ju, E. J. Min, B. H. Lee, M. Itoh, M. Miura, and Y. Yasuno, "High-penetration swept source Doppler optical coherence angiography by fully numerical phase stabilization," *Optics Express*, vol. 20, no. 3, p. 2740, 2012.

[102] S. H. Yun, G. J. Tearney, J. F. de Boer, and B. E. Bouma, "Removing the depth-degeneracy in optical frequency domain imaging with frequency shifting," *Optics Express*, vol. 12, no. 20, p. 4822, 2004.

[103] B. C. Johnson, B. Goldberg, and D. C. Flanders, "Multi-speed oct swept source with optimized k-clock," *U.S. Patent No. 9,243,885*, 2016.

[104] Y. Nakamura, S. Makita, M. Yamanari, M. Itoh, T. Yatagai, and Y. Yasuno, "High-speed three-dimensional human retinal imaging by line-field spectral domain optical coherence tomography," *Optics Express*, vol. 15, no. 12, p. 7103, 2007.

[105] L. Ginner, A. Kumar, D. Fechtig, L. M. Wurster, M. Salas, M. Pircher, and R. A. Leitgeb, "Noniterative digital aberration correction for cellular resolution retinal optical coherence tomography in vivo," *Optica*, vol. 4, no. 8, pp. 924–931, 2017.

[106] A. Dubois, L. Vabre, A.-C. Boccara, and E. Beaurepaire, "High-resolution full-field optical coherence tomography with a Linnik microscope," *Applied Optics*, vol. 41, no. 4, p. 805, 2002.

[107] B. Karamata, P. Lambelet, M. Leutenegger, M. Laubscher, S. Bourquin, and T. Lasser, "Multiple scattering in optical coherence tomography II Experimental and theoretical investigation of cross talk in wide-field optical coherence tomography," *Journal of the Optical Society of America A*, vol. 22, no. 7, p. 1380, 2005.

[108] B. Karamata, P. Lambelet, M. Laubscher, M. Leutenegger, S. Bourquin, and T. Lasser, "Multiple scattering in optical coherence tomography I Investigation and modeling," *Journal of the Optical Society of America A*, vol. 22, no. 7, p. 1369, 2005.

[109] M. Minneman, J. Ensher, M. Crawford, M. Bonesi, B. Zabihian, P. Boschert, E. Hoover, D. Derickson, B. E. Applegate, T. Milner, and W. Drexler, "Akinetik Swept Sources," in *Optical Coherence Tomography* (W. Drexler and J. G. Fujimoto, eds.), pp. 687–739, Cham: Springer International Publishing, 2015.

[110] C. Joo, T. Akkin, B. Cense, B. H. Park, and J. F. de Boer, "Spectral-domain optical coherence phase microscopy for quantitative phase-contrast imaging," *Optics Letters*, vol. 30, no. 16, p. 2131, 2005.

[111] R. K. Manapuram, V. G. R. Manne, and K. V. Larin, "Phase-sensitive swept source optical coherence tomography for imaging and quantifying of microbubbles in clear and scattering media," *Journal of Applied Physics*, vol. 105, no. 10, p. 102040, 2009.

[112] W. Choi, B. Potsaid, V. Jayaraman, B. Baumann, I. Grulkowski, J. J. Liu, C. D. Lu, A. E. Cable, D. Huang, J. S. Duker, and J. G. Fujimoto, "Phase-sensitive swept-source optical coherence tomography imaging of the human retina with a vertical cavity surface-emitting laser light source," *Optics Letters*, vol. 38, no. 3, p. 338, 2013.

[113] T. S. Ralston, D. L. Marks, P. S. Carney, and S. A. Boppart, "Inverse scattering for optical coherence tomography," *JOSA A*, vol. 23, no. 5, pp. 1027–1037, 2006.

[114] T. S. Ralston, D. L. Marks, S. A. Boppart, and P. S. Carney, "Non-Paraxial Solution to Inverse Scattering in Optical Coherence Tomography," in *Frontiers in Optics*, p. FMI3, Optical Society of America, 2006.

[115] T. Ralston, D. Marks, F. Kamalabadi, and S. Boppart, "Deconvolution methods for mitigation of transverse blurring in optical coherence tomography," *IEEE Transactions on Image Processing*, vol. 14, no. 9, pp. 1254–1264, 2005.

[116] B. Davis, S. Schlachter, D. Marks, T. Ralston, S. Boppart, and P. Carney, "Nonparaxial vector-field modeling of optical coherence tomography and interferometric synthetic aperture microscopy," *Journal of the Optical Society of America A: Optics and Image Science, and Vision*, vol. 24, no. 9, pp. 2527–2542, 2007.

[117] S. G. Adie, N. D. Shemonski, T. S. Ralston, P. S. Carney, and S. A. Boppart, "Interferometric Synthetic Aperture Microscopy (ISAM)," in *Optical Coherence Tomography* (W. Drexler and J. G. Fujimoto, eds.), pp. 965–1004, Cham: Springer International Publishing, 2015.

[118] D. L. Marks, T. S. Ralston, P. S. Carney, and S. A. Boppart, "Inverse scattering for rotationally scanned optical coherence tomography," *Journal of the Optical Society of America A*, vol. 23, no. 10, p. 2433, 2006.

[119] A. F. Fercher, W. Drexler, C. K. Hitzenberger, and T. Lasser, "Optical coherence tomography - principles and applications," *Reports on Progress in Physics*, vol. 66, no. 2, pp. 239–303, 2003.

[120] Y.-Z. Liu, F. South, Y. Xu, P. Scott Carney, and S. Boppart, "Computational optical coherence tomography [invited]," *Biomedical Optics Express*, vol. 8, no. 3, pp. 1549–1574, 2017.

[121] T. S. Ralston, D. L. Marks, P. S. Carney, and S. A. Boppart, "Interferometric synthetic aperture microscopy," *Nature Physics*, vol. 3, no. 2, pp. 129–134, 2007.

[122] C. Cafforio, C. Prati, and F. Rocca, "SAR data focusing using seismic migration techniques," *IEEE Transactions on Aerospace and Electronic Systems*, vol. 27, no. 2, pp. 194–207, 1991.

[123] R. H. Stolt, "Mitigation by Fourier transform," *GEOPHYSICS*, vol. 43, no. 1, pp. 23–48, 1978.

[124] Y.-Z. Liu, N. Shemonski, S. Adie, A. Ahmad, A. Bower, P. Scott Carney, and S. Boppart, "Computed optical interferometric tomography for high-speed volumetric cellular imaging," *Biomedical Optics Express*, vol. 5, no. 9, pp. 2988–3000, 2014.

[125] S. Boppart, "Computational adaptive optics for broadband optical interferometric tomography of biological tissue," vol. 9335 of *Progress in Biomedical Optics and Imaging - Proceedings of SPIE*, SPIE, 2015.

[126] L. Yi and L. Sun, "Structure and Function Sensing of Bio-tissues Based on Dual Channel Spectral Domain OCT," in *2019 IEEE SENSORS*, (Montreal, QC, Canada), pp. 1–4, IEEE, 2019.

[127] A. Zysk, K. Chen, E. Gabrielson, L. Tafra, E. May Gonzalez, J. Canner, E. Schneider, A. Cittadine, P. Scott Carney, S. Boppart, K. Tsuchiya, K. Sawyer, and L. Jacobs, "Intraoperative assessment of final margins with a handheld optical imaging probe during breast-conserving surgery may reduce the reoperation rate: Results of a multicenter study," *Annals of Surgical Oncology*, vol. 22, no. 10, pp. 3356–3362, 2015.

[128] D. L. Marks, T. S. Ralston, P. S. Carney, and S. A. Boppart, "An Inverse scattering method for catheter-based optical coherence tomography," in *Biomedical Optics*, (Fort Lauderdale, Florida), p. WE9, OSA, 2006.

[129] B. Davis, T. Ralston, D. Marks, S. Boppart, and P. Scott Carney, "Polarimetric interferometric synthetic aperture microscopy: Vectorial computed imaging from optical coherence tomography data," Optics InfoBase Conference Papers, Optical Society of America, 2007.

[130] T. S. Ralston, D. L. Marks, P. S. Carney, and S. A. Boppart, "Real-time interferometric synthetic aperture microscopy," *Optics Express*, vol. 16, no. 4, pp. 2555–2569, 2008.

[131] A. Ralston, M. Ali, F. South, G. Monroy, S. Adie, N. Shemonski, P. Carney, and S. Boppart, "Interferometric synthetic aperture microscopy implementation on a floating point multi-core digital signal processer," vol. 8571 of *Progress in Biomedical Optics and Imaging - Proceedings of SPIE*, 2013.

[132] L. St. Marie, F. An, A. Corso, J. Grasel, and R. Haskell, "Robust, real-time, digital focusing for FD-OCM using ISAM on a GPU," vol. 8934 of *Progress in Biomedical Optics and Imaging - Proceedings of SPIE*, SPIE, 2013.

[133] F. South, Y.-Z. Liu, P. Carney, and S. Boppart, "Computed optical interferometric imaging: Methods, achievements, and challenges," *IEEE Journal on Selected Topics in Quantum Electronics*, vol. 22, no. 3, 2016.

[134] L. Yu, B. Rao, J. Zhang, J. Su, Q. Wang, S. Guo, and Z. Chen, "Improved lateral resolution in optical coherence tomography by digital focusing using two-dimensional numerical diffraction method," *Optics Express*, vol. 15, no. 12, pp. 7634–7641, 2007.

[135] Y. Liu, Y. Liang, G. Mu, and X. Zhu, "Deconvolution methods for image deblurring in optical coherence tomography," *Journal of the Optical Society of America A: Optics and Image Science, and Vision*, vol. 26, no. 1, pp. 72–77, 2009.

[136] P. Meemon, K.-S. Lee, S. Murali, and J. Rolland, "Optical design of a dynamic focus catheter for high-resolution endoscopic optical coherence tomography," *Applied Optics*, vol. 47, no. 13, pp. 2452–2457, 2008.

[137] J. Xi, L. Huo, Y. Wu, M. J. Cobb, J. H. Hwang, and X. Li, "High-resolution OCT balloon imaging catheter with astigmatism correction," *Optics Letters*, vol. 34, no. 13, p. 1943, 2009.

[138] J. Mo, M. De Groot, and J. De Boer, "Focus-extension by depth-encoded synthetic aperture in Optical Coherence Tomography," *Optics Express*, vol. 21, no. 8, pp. 10048–10061, 2013.

[139] E. Bo, Y. Luo, S. Chen, X. Liu, N. Wang, X. Ge, X. Wang, S. Chen, S. Chen, J. Li, and L. Liu, "Depth-of-focus extension in optical coherence tomography via multiple aperture synthesis," *Optica*, vol. 4, no. 7, pp. 701–706, 2017.

[140] D. Fechtig, A. Kumar, B. Grajciar, A. Singh, W. Drexler, and R. Leitgeb, "Line field off axis swept source OCT utilizing digital refocusing," vol. 9129 of *Proceedings of SPIE - The International Society for Optical Engineering*, SPIE, 2014.

[141] S. Adie, N. Shemonski, B. Graf, A. Ahmad, P. Carney, and S. Boppart, "Broadband optical interferometric tomography with computational adaptive optics using 'guide stars'," Frontiers in Optics, FIO 2012, 2012.

[142] V. Lakshminarayanan and A. Fleck, "Zernike polynomials: A guide," *Journal of Modern Optics*, vol. 58, no. 7, pp. 545–561, 2011.

[143] B. C. Flores, "Robust method for the motion compensation of ISAR imagery," in *Intelligent Robots and Computer Vision X: Algorithms and Techniques*, vol. 1607, pp. 512–518, International Society for Optics and Photonics, 1992.

[144] C. Trujillo and J. Garcia-Sucerquia, "Comparative analysis of the modified enclosed energy metric for self-focusing holograms from digital lensless holographic microscopy," *Applied Optics*, vol. 54, no. 16, p. 5102, 2015.

[145] P. Memmolo, C. Distante, M. Paturzo, A. Finizio, P. Ferraro, and B. Javidi, "Automatic focusing in digital holography and its application to stretched holograms," *Optics Letters*, vol. 36, no. 10, p. 1945, 2011.

[146] D. Debarre, M. J. Booth, and T. Wilson, "Image based adaptive optics through optimisation of low spatial frequencies," *Optics Express*, vol. 15, no. 13, p. 8176, 2007.

[147] F. South, K. Kurokawa, Z. Liu, Y.-Z. Liu, D. Miller, and S. Boppart, "Combined hardware and computational optical wavefront correction," *Biomedical Optics Express*, vol. 9, no. 6, pp. 2562–2574, 2018.

[148] W. Wallace, L. H. Schaefer, and J. R. Swedlow, "A Workingperson's Guide to Deconvolution in Light Microscopy," *BioTechniques*, vol. 31, no. 5, pp. 1076–1097, 2001.

[149] J. Pawley, *Handbook of Biological Confocal Microscopy*. 2006.

[150] D. S. Biggs, "3D Deconvolution Microscopy," *Current Protocols in Cytometry*, vol. 52, no. 1, pp. 12.19.1–12.19.20, 2010.

[151] P. D. Woolliams, R. A. Ferguson, C. Hart, A. Grimwood, and P. H. Tomlins, "Spatially deconvolved optical coherence tomography," *Applied Optics*, vol. 49, no. 11, p. 2014, 2010.

[152] B. Braaf, M. G. O. Gräfe, N. Uribe-Patarroyo, B. E. Bouma, B. J. Vakoc, J. F. de Boer, S. Donner, and J. Weichsel, "OCT-Based Velocimetry for Blood Flow Quantification," in *High Resolution Imaging in Microscopy and Ophthalmology* (J. F. Bille, ed.), pp. 161–179, Cham: Springer International Publishing, 2019.

[153] C. Yang, A. Wax, M. S. Hahn, K. Badizadegan, R. R. Dasari, and M. S. Feld, "Phase-referenced interferometer with subwavelength and subhertz sensitivity applied to the study of cell membrane dynamics," *Optics Letters*, vol. 26, no. 16, p. 1271, 2001.

[154] D. Fechtig, A. Kumar, L. Ginner, W. Drexler, and R. Leitgeb, "High-speed, digitally refocused retinal imaging with Line-field parallel swept source OCT," vol. 9312 of *Progress in Biomedical Optics and Imaging - Proceedings of SPIE*, SPIE, 2015.

[155] R. Leitgeb, L. Ginner, A. Kumar, and D. Fechtig, "Digital aberration correction for in-vivo retinal OCT imaging," 2016 15th Workshop on Information Optics, WIO 2016, Institute of Electrical and Electronics Engineers Inc., 2016.

[156] F. South, Y.-Z. Liu, P.-C. Huang, T. Kohlfarber, and S. Boppart, "Local wavefront mapping in tissue using computational adaptive optics OCT," *Optics Letters*, vol. 44, no. 5, pp. 1186–1189, 2019.

[157] P. Pande, Y.-Z. Liu, F. A. South, and S. A. Boppart, "Automated computational aberration correction method for broadband interferometric imaging techniques," *Optics Letters*, vol. 41, no. 14, p. 3324, 2016.

[158] A. Kumar, T. Kamali, R. Platzer, A. Unterhuber, W. Drexler, and R. Leitgeb, "Anisotropic aberration correction using region of interest based digital adaptive optics in fourier domain oct," *Biomedical Optics Express*, vol. 6, no. 4, pp. 1124–1134, 2015.

[159] G. B. Arfken, H. J. Weber, and F. E. Harris, "Legendre Functions," in *Mathematical Methods for Physicists*, pp. 715–772, Elsevier, 2013.

[160] G. Liu, S. Yousefi, Z. Zhi, and R. K. Wang, "Automatic estimation of point-spread-function for deconvoluting out-of-focus optical coherence tomographic images using information entropy-based approach," *Optics Express*, vol. 19, no. 19, p. 18135, 2011.

[161] G. Liu, Z. Zhi, and R. K. Wang, "Digital focusing of OCT images based on scalar diffraction theory and information entropy," *Biomedical Optics Express*, vol. 3, no. 11, p. 2774, 2012.

[162] J. C. Lagarias, J. A. Reeds, M. H. Wright, and P. E. Wright, "Convergence Properties of the Nelder–Mead Simplex Method in Low Dimensions," *SIAM Journal on Optimization*, vol. 9, no. 1, pp. 112–147, 1998.

[163] J. W. Brault and O. R. White, "The Analysis and Restoration of Astronomical Data via the Fast Fourier Transform," *Astronomy and Astrophysics*, vol. 13, p. 169, 1971.

[164] J. A. Bonet, "High Spatial Resolution Imaging in Solar Physics," in *Motions in the Solar Atmosphere* (A. Hanslmeier and M. Messerotti, eds.), vol. 239, pp. 1–34, Dordrecht: Springer Netherlands, 1999.

[165] M. F. Kraus and J. Hornegger, "OCT Motion Correction," in *Optical Coherence Tomography* (W. Drexler and J. G. Fujimoto, eds.), pp. 459–476, Cham: Springer International Publishing, 2015.

[166] S. Ricco, M. Chen, H. Ishikawa, G. Wollstein, and J. Schuman, "Correcting Motion Artifacts in Retinal Spectral Domain Optical Coherence Tomography via Image Registration," in *Medical Image Computing and Computer-Assisted Intervention – MICCAI 2009* (G.-Z. Yang, D. Hawkes, D. Rueckert, A. Noble, and C. Taylor, eds.), vol. 5761, pp. 100–107, Berlin, Heidelberg: Springer Berlin Heidelberg, 2009.

[167] G. Maguluri, M. Mujat, B. Park, K. Kim, W. Sun, N. Iftimia, R. D. Ferguson, D. X. Hammer, T. C. Chen, and J. F. de Boer, "Three dimensional tracking for volumetric spectral-domain optical coherence tomography," *Optics Express*, vol. 15, no. 25, p. 16808, 2007.

[168] E. Auksorius, D. Borycki, P. Stremplewski, K. Liżewski, S. Tomczewski, P. Niedźwiedziuk, B. L. Sikorski, and M. Wojtkowski, "In vivo imaging of the human cornea with high-speed and high-resolution Fourier-domain full-field optical coherence tomography," *Biomedical Optics Express*, vol. 11, no. 5, p. 2849, 2020.

[169] R. J. Zawadzki, A. R. Fuller, S. S. Choi, D. F. Wiley, B. Hamann, and J. S. Werner, "Correction of motion artifacts and scanning beam distortions in 3D ophthalmic optical coherence tomography imaging," in *Biomedical Optics (BiOS) 2007* (F. Manns, P. G. Soederberg, A. Ho, B. E. Stuck, and M. Belkin, eds.), (San Jose, CA), p. 642607, 2007.

[170] M. Guizar-Sicairos, S. T. Thurman, and J. R. Fienup, "Efficient subpixel image registration algorithms," *Optics Letters*, vol. 33, no. 2, p. 156, 2008.

[171] M. F. Kraus, B. Potsaid, M. A. Mayer, R. Bock, B. Baumann, J. J. Liu, J. Hornegger, and J. G. Fujimoto, "Motion correction in optical coherence tomography volumes on a per A-scan basis using orthogonal scan patterns," *Biomedical Optics Express*, vol. 3, no. 6, p. 1182, 2012.

[172] M. Guizar, "Efficient subpixel image registration by cross-correlation." https://www.mathworks.com/matlabcentral/fileexchange/18401-efficient-subpixel-image-registration-by-cross-correlation, 2020.

[173] J. M. Beckers, "Adaptive Optics for Astronomy: Principles, Performance, and Applications," *Annual Review of Astronomy and Astrophysics*, vol. 31, no. 1, pp. 13–62, 1993.

[174] J. F. de Boer, C. K. Hitzenberger, and Y. Yasuno, "Polarization sensitive optical coherence tomography – a review [Invited]," *Biomedical Optics Express*, vol. 8, no. 3, p. 1838, 2017.

[175] M. Villiger, K. Otsuka, A. Karanasos, P. Doradla, J. Ren, N. Lippok, M. Shishkov, J. Daemen, R. Diletti, R.-J. van Geuns, F. Zijlstra, G. van Soest, P. Libby, E. Regar, S. K. Nadkarni, and B. E. Bouma, "Coronary Plaque Microstructure and Composition Modify Optical Polarization," *JACC: Cardiovascular Imaging*, vol. 11, no. 11, pp. 1666–1676, 2018.

[176] B. Elmaanaoui, B. Wang, J. C. Dwelle, A. B. McElroy, S. S. Liu, H. G. Rylander, and T. E. Milner, "Birefringence measurement of the retinal nerve fiber layer by swept source polarization sensitive optical coherence tomography," *Optics Express*, vol. 19, no. 11, p. 10252, 2011.

[177] Q. Li, K. Karnowski, G. Untracht, P. B. Noble, B. Cense, M. Villiger, and D. D. Sampson, "Vectorial birefringence imaging by optical coherence microscopy for assessing fibrillar microstructures in the cornea and limbus," *Biomedical Optics Express*, vol. 11, no. 2, p. 1122, 2020.

[178] M. Villiger, E. Z. Zhang, S. K. Nadkarni, W.-Y. Oh, B. J. Vakoc, and B. E. Bouma, "Spectral binning for mitigation of polarization mode dispersion artifacts in catheter-based optical frequency domain imaging," *Optics Express*, vol. 21, no. 14, p. 16353, 2013.

[179] R. A. Chipman, "Polarization Analysis Of Optical Systems," *Optical Engineering*, vol. 28, no. 2, 1989.

[180] M. Szkulmowski and M. Wojtkowski, "Averaging techniques for OCT imaging," *Optics Express*, vol. 21, no. 8, p. 9757, 2013.

[181] A. Sakamoto, M. Hangai, and N. Yoshimura, "Spectral-Domain Optical Coherence Tomography with Multiple B-Scan Averaging for Enhanced Imaging of Retinal Diseases," *Ophthalmology*, vol. 115, no. 6, pp. 1071–1078.e7, 2008.

[182] C.-A. Deledalle, L. Denis, F. Tupin, A. Reigber, and M. Jager, "NL-SAR: A Unified Nonlocal Framework for Resolution-Preserving (Pol)(In)SAR Denoising," *IEEE Transactions on Geoscience and Remote Sensing*, vol. 53, no. 4, pp. 2021–2038, 2015.

[183] K. Lu, N. He, and L. Li, "Nonlocal Means-Based Denoising for Medical Images," *Computational and Mathematical Methods in Medicine*, vol. 2012, pp. 1–7, 2012.

[184] H. Yu, J. Gao, and A. Li, "Probability-based non-local means filter for speckle noise suppression in optical coherence tomography images," *Optics Letters*, vol. 41, no. 5, p. 994, 2016.

[185] P. Coupe, P. Yger, S. Prima, P. Hellier, C. Kervrann, and C. Barillot, "An Optimized Blockwise Nonlocal Means Denoising Filter for 3-D Magnetic Resonance Images," *IEEE Transactions on Medical Imaging*, vol. 27, no. 4, pp. 425–441, 2008.

[186] S. Makita, K. Kurokawa, Y.-J. Hong, M. Miura, and Y. Yasuno, "Noise-immune complex correlation for optical coherence angiography based on standard and

Jones matrix optical coherence tomography," *Biomedical Optics Express*, vol. 7, no. 4, p. 1525, 2016.

[187] C.-A. Deledalle, L. Denis, and F. Tupin, "How to Compare Noisy Patches? Patch Similarity Beyond Gaussian Noise," *International Journal of Computer Vision*, vol. 99, no. 1, pp. 86–102, 2012.

[188] N. Uribe-Patarroyo, M. Villiger, and B. E. Bouma, "Quantitative technique for robust and noise-tolerant speed measurements based on speckle decorrelation in optical coherence tomography," *Optics Express*, vol. 22, no. 20, p. 24411, 2014.

[189] R. K. Wang, S. Kirkpatrick, and M. Hinds, "Phase-sensitive optical coherence elastography for mapping tissue microstrains in real time," *Applied Physics Letters*, vol. 90, no. 16, p. 164105, 2007.

[190] B. Braaf, S. Donner, A. S. Nam, B. E. Bouma, and B. J. Vakoc, "Complex differential variance angiography with noise-bias correction for optical coherence tomography of the retina," *Biomedical Optics Express*, vol. 9, no. 2, p. 486, 2018.

[191] D. Huang, Y. Li, and M. Tang, "Anterior Eye Imaging with Optical Coherence Tomography," in *Optical Coherence Tomography* (W. Drexler and J. G. Fujimoto, eds.), pp. 1649–1683, Cham: Springer International Publishing, 2015.

[192] L. Wang, Q. Xiong, X. Ge, E. Bo, J. Xie, X. Liu, X. Yu, X. Wang, N. Wang, S. Chen, X. Wu, and L. Liu, "Cellular resolution corneal imaging with extended imaging range," *Optics Express*, vol. 27, no. 2, pp. 1298–1309, 2019.

[193] W. Drexler and J. G. Fujimoto, "Retinal Optical Coherence Tomography Imaging," in *Optical Coherence Tomography* (W. Drexler and J. G. Fujimoto, eds.), pp. 1685–1735, Cham: Springer International Publishing, 2015.

[194] G. Yiu, P. Pecen, N. Sarin, S. J. Chiu, S. Farsiu, P. Mruthyunjaya, and C. A. Toth, "Characterization of the Choroid-Scleral Junction and Suprachoroidal Layer in Healthy Individuals on Enhanced-Depth Imaging Optical Coherence Tomography," *JAMA Ophthalmology*, vol. 132, no. 2, p. 174, 2014.

[195] M. E. Brezinski, G. J. Tearney, B. E. Bouma, S. A. Boppart, M. R. Hee, E. A. Swanson, J. F. Southern, and J. G. Fujimoto, "Imaging of coronary artery microstructure (in vitro) with optical coherence tomography," *The American Journal of Cardiology*, vol. 77, no. 1, pp. 92–93, 1996.

[196] G. Isenberg and M. V. Sivak, "Gastrointestinal optical coherence tomography," *Techniques in Gastrointestinal Endoscopy*, vol. 5, no. 2, pp. 94–101, 2003.

[197] T. Wang, A. F. W. van der Steen, and G. van Soest, "Numerical analysis of astigmatism correction in gradient refractive index lens based optical coherence tomography catheters," *Applied Optics*, vol. 51, no. 21, p. 5244, 2012.

[198] W. Kang, H. Wang, Y. Pan, M. W. Jenkins, G. A. Isenberg, A. Chak, M. Atkinson, D. Agrawal, Z. Hu, and A. M. Rollins, "Endoscopically guided spectral-domain OCT with double-balloon catheters," *Optics Express*, vol. 18, no. 16, p. 17364, 2010.

[199] J. Holmes and J. Welzel, "OCT in Dermatology," in *Optical Coherence Tomography* (W. Drexler and J. G. Fujimoto, eds.), pp. 2189–2207, Cham: Springer International Publishing, 2015.

[200] K. Bizheva, B. Tan, B. MacLellan, Z. Hosseinaee, E. Mason, D. Hileeto, and L. Sorbara, "In-vivo imaging of the palisades of Vogt and the limbal crypts with sub-micrometer axial resolution optical coherence tomography," *Biomedical Optics Express*, vol. 8, no. 9, p. 4141, 2017.

[201] Q. Li, K. Karnowski, P. B. Noble, A. Cairncross, A. James, M. Villiger, and D. D. Sampson, "Robust reconstruction of local optic axis orientation with fiber-based polarization-sensitive optical coherence tomography," *Biomedical Optics Express*, vol. 9, no. 11, p. 5437, 2018.